UNIVERSITY OF OKLAHOMA
GRADUATE COLLEGE

CONVECTION-DRIVEN STRATOSPHERE-TROPOSPHERE EXCHANGE: OBSERVATIONS AND SIMULATIONS OF MIDLATITUDE THUNDERSTORMS AND TROPICAL CYCLONES

A DISSERTATION
SUBMITTED TO THE GRADUATE FACULTY
in partial fulfillment of the requirements for the
Degree of
DOCTORATE OF PHILOSOPHY

by ANDREA E GORDON
Norman, Oklahoma
2026

Downloaded from SHAREOK. Persistent Handle URL: https://hdl.handle.net/11244/342888

CONVECTION-DRIVEN STRATOSPHERE-TROPOSPHERE EXCHANGE: OBSERVATIONS AND SIMULATIONS OF MIDLATITUDE THUNDERSTORMS AND TROPICAL CYCLONES

A DISSERTATION APPROVED FOR THE
SCHOOL OF METEOROLOGY

BY THE COMMITTEE CONSISTING OF

Dr. Cameron Homeyer (Chair)

Dr. Steven Cavallo

Dr. Elinor Martin

Dr. Valerie Watts

©Copyright by ANDREA E GORDON 2026

All Rights Reserved.

Acknowledgments

The past five years completing my PhD, eight as a part of the Chemistry, Convection, and Climate (CCC) Research Group, and nine at the University of Oklahoma have been a whirlwind filled with joy, challenges, and growth that has been so meaningful and rewarding to me. As I write these acknowledgments, it is hard to believe this time is truly here. Reflecting on my time working towards my PhD, it is surreal to think that this experience is wrapping up and this journey will be complete. I cannot express my gratitude to all those who have helped support and encourage me throughout my PhD, but I will try. Please note that these acknowledgments are in no particular order and are by no means an exhaustive list.

I would like to acknowledge my advisor and "science dad" Dr. Cameron Homeyer. It is wild to think all the way back to when I first started working with you as an undergraduate the summer after my freshman year. You have been a mentor through the highs and lows during covid, the DCOTSS field campaign, many conferences (including adventures to Austria and Slovakia), and so many memories in Norman. I am so thankful to have been able to be your student the past eight years. I struggle to find words to express how grateful I am for your mentorship, unconditional support, and encouragement. Thank you for always believing in me, even when I didn't believe in myself. Thank you for showing me what it means to be a great scientist, and encouraging my perseverance, scientific curiosities, and goofiness. Thank you for always accepting me as I am, which has allowed me to grow as a scientist and person. I am inspired by your dedication to your family, your students, your ideals, and your community. You the best advisor I could have asked for, and I would not be the scientist or person I am today without your influence.

I would like to thank my committee members Drs. Steven Cavallo, Elinor Martin, and Valerie Watts for their encouragement, support, and advice throughout the years. Elinor, I have learned so much in your classes and broadened my perspective about the field. Steven, thank you for being my capstone mentor in my undergraduate degree and your support since. Dr. Watts, thank you for encouraging my meteorology passions and supporting me as my as my flute professor in my undergraduate degree from the beginning, I am glad you were able to be a committee member. I would also like to thank Dr. Amanda Kis for her mentorship towards teaching in the classroom.

There are many scientists outside of the University of Oklahoma who have supported and encouraged me, and who I have learned greatly from. Thank you to Dr. Bill Randel for believing in me as a scientist and your mentorship. Thank you for encouraging me to think critically as a scientist and when to trust what I am seeing. I am thankful for your wisdom and support along this journey of discovery with tropical cyclones and radio occultation, and I am excited for what is to come. Thank you, Dr. Rosimar Rios Berrios, for the wisdom and encouragement you have showed me as I took a leap into the tropical cyclone community. You have been so welcoming and have helped me grow as a scientist, and I am excited for future collaborations. To other scientists and mentors at NCAR including Drs. Gretchen Mullendore, Ren Smith, and Quinton Lawton, thank you for your encouragement, advice, and giving me a sense of community during my visits at NCAR and beyond. I would like to thank the team members of the Dynamics and Chemistry of the Summer Stratosphere (DCOTSS) field campaign. Working with this campaign was such a formative scientific experience for me, and I would be remiss if I did not thank the forecasting and flight planning team for creating such a positive environment. Thank you to Dr. Rei Ueyama and Kris Bedka for your support and encouraging me to voice my opinions. You all made me feel seen, heard and valued as an early career scientist throughout this campaign, which helped

with my self-confidence.

My graduate school experience would not be the same without those who have experienced it with me. I am grateful to so many of my past and present fellow CCC research group members, including Amanda, Elisa, Emily, Hannah, Ry, Jaime, and Francesco. Thank you for the collaboration, community, adventures, laughs, rants, and so much more. Elisa, thank you for all the emotional validation over the years and for showing me it is always worth advocating for myself. Emily, I am beyond grateful for all of our Beanstalk coffee days, taco trips, hiking adventures, and for all the emotional support and wisdom you have shared over the years. I must express my gratitude to my fellow office mates of 5700 both past and present including Melanie, Alethia, Bryony, and Margaret. Thank you for making this such a fun space to work throughout the past eight years. Mel, thank you for all the advice and support throughout the years. Thank you to my undergraduate research assistant, Eli Harrison, for making my first advising experience such a positive one. Witnessing your confidence, curiosity, and scientific skills grow has brought me so much joy.

I am so grateful for the support I have received from my friends, including those from my time at OU and before. You all have been there throughout the highs and lows of graduate school, and I am thankful for all the support, laughter, and understanding. To my friends I have during my PhD, I am so grateful to have shared this experience with you, and would not have been able to do it without your support. I am so grateful for the adventures we have shared over the years. Erica and Rachel, even though we are now spread out across the country I am thankful for your support, encouragement, and always boosting my spirits. I would like to thank my partner Evan for all his support throughout this journey. I appreciate your understanding, patience, and the sense of calm you bring.

I owe my deepest gratitude to my family and their unwavering support. To my

mom Nancy, my dad Jeff, and my brother Luke, thank you for all the reassurance, encouragement, and for always listening to me. Thank you for accommodating my hectic and changing schedule, always being a shoulder to cry on, and being excited to celebrate my wins. Thank you for always believing in me and for being my rock. Your support means so much, and I truly could not have done this without you. Although he is no longer with us, I would like to thank my dog Taz for all of the unconditional love, laughter, and entertainment through my time in graduate school and all the years before.

Lastly, this work would not have been possible without funding by the National Aeronautics and Space Administration (NASA) under Awards 80NSSC19K0347 and 80NSSC23K1003.

Table of Contents

Acknowledgments iv

List of Figures x

Abstract xviii

1 Introduction 1
1.1 Midlatitude Overshooting Convection 3
1.2 Tropical Cyclones 9

2 Sensitivities of Cross-Tropopause Transport in Midlatitude Overshooting Convection to the Lower Stratosphere Environment 16
2.1 Model Design 17
2.2 Results 19
2.2.1 UTLS Hydration and Cross-Tropopause Transport 20
2.2.2 Potential Mechanisms Impacting Transport 29
2.3 Summary 36

3 Airborne observations of upper troposphere and lower stratosphere composition change in active convection producing above-anvil cirrus plumes 39
3.1 Data and Methods 40
3.1.1 DCOTSS Overview 40
3.1.2 DCOTSS Observations 41
3.1.3 ERA5 Reanalysis 43
3.1.4 Radar Observations 44
3.1.5 Satellite Observations 44
3.2 Results 45
3.2.1 Storm Characteristics and Flight Overview 45
3.2.2 UTLS Composition Changes 48
3.3 Summary 65

4 Examining Stratosphere-Troposphere Exchange in Idealized Simulations of Tropical Cyclones 68

4.1 Model Setup and Design . . . 69
4.1.1 Model Configuration . . . 69
4.1.2 Passive Tracer Design . . . 70
4.2 Results . . . 71
4.2.1 Processes Contributing to Exchange in Tropical Cyclones . . . 76
4.2.2 Transport Sensitivity to Intensity . . . 90
4.2.3 Transport Sensitivity to Deep-Layer Shear . . . 91
4.3 Summary . . . 98

5 Discovery of Tropical Cyclone-Driven Stratospheric Temperature Anomalies using Radio Occultation Observations . . . 104
5.1 Data and Methods . . . 105
5.1.1 ROMEX Temperature . . . 105
5.1.2 ERA5 Reanalysis Temperature and Wind . . . 106
5.2 Results . . . 108
5.3 Summary . . . 116

6 Summary and Conclusions . . . 118
6.1 Lessons Learned . . . 118
6.2 Midlatitude Overshooting Convection . . . 120
6.3 Tropical Cyclones . . . 123
6.4 Recommended Directions of Future Research . . . 125

Reference List . . . 128

List of Figures

1.1 Illustration of (left) top-down view of a tropical cyclone and (right) vertical cross section of a tropical cyclone with known stratosphere troposphere exchange processes. These processes include: isentropic mixing, subsidence, two exchange facilitated by overshooting tops, and apparent stratospheric air wrapping at outflow edge. The tropopause is annotated in blue and near-tropopause isentrope is annotated in red. 12

2.1 Initial conditions (profiles) of idealized simulations including (left) temperature for (blue) single tropopause and (red) double tropopause environments, and (middle) wind speed and (right) wind direction for (solid line) AACP-producing storms and (dashed line) non-AACP storms. . . 18

2.2 Evolution of cloud top altitudes (the maximum altitude that the sum of ice and cloud mixing ratios exceeds 1×10^{-6} kg kg^{-1}) at 60, 90, and 120 minutes for (top to bottom): AACP-producing storm simulations with a single tropopause, AACP-producing with a double tropopause, non-AACP with a single tropopause, and non-AACP with a double tropopause. The domain size for each panel is 185 km by 150 km. . . . 21

2.3 As in Fig. 2.2, but for near-surface simulated radar reflectivity. 22

2.4 Time-height curtains of the domain-integrated mass change in H_2O relative to the initial H_2O mass at each altitude for (left) AACP-producing storms, (right) non-AACP storms, (top) single tropopause environments, and (bottom) double tropopause environments. Vertical lines at a simulation time of 50 minutes indicate the first time of overshooting (that when the cloud top height first exceeds the primary tropopause altitude of 12 km). Thick solid and long-dashed horizontal lines represent the initial primary and secondary tropopause altitudes, respectively, while additional dotted lines at 10 km and 14.2 km (380 K) are for visual reference only. 24

2.5 As in Fig. 4, but for passive tracer 1 (PT1; boundary layer air) mass change relative to the initial domain-integrated dry air mass. 26

2.6 As in Fig. 2.5, but for passive tracer 2 (PT2; stratospheric air). 27

2.7 As in Fig 2.5, but for passive tracer 3 (PT3; stratospheric overworld air). 28

2.8 Domain-integrated mass profiles at the final simulation time of 120 minutes of a) water vapor (H_2O), b) passive tracer 1 (PT1; boundary layer air), c) passive tracer 2 (PT2; stratospheric air), and d) passive tracer 3 (PT3; stratospheric overworld air). Initial domain-integrated mass profiles of H_2O and dry air are given in panels a and b-d, respectively, for reference. 29

2.9 Time-height curtains of (left) domain-minimum potential temperature gradient and (right) areal extent of instability (potential temperature gradient less than 0 K km^{-1}) for (top) AACP-producing and (bottom) non-AACP storms. 31

2.10 As in Fig. 2.9, but for the (left) maximum and (right) minimum vertical velocity. Dashed orange lines coincide with subjectively identified ascending (descending) maxima (minima) in vertical velocity with time. 33

2.11 Vertical cross-sections at a simulation time of 90 minutes for (left) single tropopause AACP-producing and (right) single tropopause non-AACP storms. From top to bottom: water vapor (H_2O; in ppmv), passive tracer 1 (PT1; boundary layer air), passive tracer 2 (PT2; stratospheric air), and passive tracer 3 (PT3; stratospheric overworld air). Vertical velocity contours are shown in gray in each panel, with intervals of 5 m/s (upward motion is solid and downward is dashed). Black contours in each panel represent potential temperature at 10-K intervals (with solid contours for 380 K and above, and dashed below). The potential temperature of the environmental tropopause (345 K) is shown in magenta in each panel. The blue arrows and blue ellipse atop the PT1 sections identify the mechanical oscillation and hydraulic jump features, respectively. . . 34

2.12 Vertical velocity at 12 km for (left) AACP-producing and (right) non-AACP storms at 90 minutes. The black contour outlines the cloud boundary (where the sum of ice and cloud mixing ratios is greater than 1.0E-6 kg/kg). 36

3.1 From top to bottom, GridRad radar reflectivity (Z_H; panels a–c), GridRad Z_H = 15.0 dBZ tropopause-relative echo top heights (km; panels d–f), GOES-16 infrared imagery (panels g–i), and GOES-16 visible imagery (panels j–l) at: (left) 23:00 UTC on 31 May 2022 (takeoff), (middle) 00:20 UTC on 01 June 2022 (convective sampling begins), and (right) 02:10 UTC on 01 June 2022 (start of the AACP bisects). The latitude and longitude domain span 33.3-37.5°N, 94.0-103.5°W. The targeted overshoot is annotated with a yellow circle, while the targeted AACP is annotated with a cyan oval. 46

3.2 ER-2 aircraft flight track for the 31 May 2022 flight shaded by (a) altitude in km, and (b) HHH H_2O in ppmv, spanning a domain of 33.0-39.5°N, 96.0-100.5°W. The star symbol indicates the location of Salina, KS, the base of the DCOTSS field campaign. The plane symbols labeled A, B, C, and D coincide with ER-2 camera imagery shown in Fig. 3.3. Point 1 (P1) is the starting point of the racetrack sampling, point 2 (P2) is the endpoint of the racetrack sampling, and point 3 (P3) was the endpoint of the AACP bisect sampling. 47

3.3 Visible imagery from the rotatable camera aboard the NASA ER-2 aircraft taken at (a) 00:09 UTC where the camera is facing forward toward the northwest, (b) 00:34 UTC where the camera is facing right of the aircraft towards the west, (c) 02:19 UTC where the camera is facing right of the aircraft towards the northwest, and (d) 02:24 UTC on 01 June 2022 where the camera is facing to the right of the aircraft toward the northwest. These images correspond to the plane symbols labeled A, B, C, and D in Fig. 3.2. 49

3.4 The convective sampling period (in UTC) of the DCOTSS 31 May 2022 flight shown as timeseries. All timeseries include the MMS GPS aircraft altitude (thick black line) and illustrations of the convective sampling segments (light blue shading, labeled 1–6 in timeseries (a)). The top timeseries (a) includes WI-ICOS total water (gray), ERA5 LRT altitude (dashed black line), and H_2O mixing ratio (blue). Points P1, P2, and P3 from Fig. 3.2 are labeled (gray) atop timeseries (a). The middle timeseries (b) includes HUPCRS CO (red), MMS potential temperature (purple), ROZE O_3 mixing ratio (yellow), and HUPCRS CH_4 (green). The lower timeseries (c) includes AWAS ethyne (magenta), ethane (blue), propane (orange), and canister fill time (vertical gray bars of varying width). 50

3.5 An illustration of AACP sampling during the 31 May 2022 flight. Dynamic processes which would be expected to encounter (based on prior modeling work) and their feature-relative locations are indicated, including the decayed overshoot (gray), the AACP (blue), mixing associated with the coupling of the hydraulic jump and mechanical oscillation (purple), and the expected location of maximum turbulence (red). The ER-2 is shown in black, and an outline of the flight track along the AACP bisects is denoted in gray in the top-down view panel. 54

3.6 AACP sampling during the 31 May 2022 flight (in UTC) shown as timeseries. Both timeseries include the MMS GPS aircraft altitude (thick black line) and potential temperature (purple line). The top timeseries (a) uniquely includes HUPCRS CO (red), ROZE O_3 mixing ratio (yellow), and HHH H_2O mixing ratio (blue). The lower timeseries (b) uniquely includes MMS measurements of the vertical wind speed (m s^{-1}; yellow), the $\log_{10}$ of the Turbulent Eddy Dissipation Rate (TEDR; red), and the vertical-to-horizontal TKE ratio (green). The dark blue box in each timeseries denotes the time period of the 'stratospheric signal' near the end of the first AACP bisect, and gray horizontal lines with arrows at each end denote times when the ER-2 is within the AACP and in the turbulence-avoidance vertical profile. 55

3.7 As in Fig. 3.6, but with top timeseries (a) of MMS GPS altitude (black), MMS potential temperature (purple), ROZE O_3 mixing ratio (yellow), HHH H_2O mixing ratio (blue), positive O_3-H_2O correlations (blue shading), and negative O_3-H_2O correlations (pink shading). The lower timeseries (b) includes MMS GPS altitude (black), MMS saturation mixing ratio (dark blue), MMS temperature (brown), H_2O mixing ratio (light blue), and WI-ICOS total water (gray). 59

3.8 Illustration of the process that is generally expected for an overshoot which results in a negative O_3-H_2O correlation (top panels), and a saturation-limited overshoot and hypothesized process resulting in a positive O_3-H_2O correlation (bottom panels). 61

3.9 Density of CO (left) and H_2O (right) in LRT-relative altitude of convective segments (blue; a and b) and background segments (gray; c and d) from all DCOTSS 2021 and 2022 flights except for the 31 May 2022 flight. Convective sampling from 31 May 2022 flight (red) and AACP sampling from 31 May 2022 flight (yellow) are shown atop the respective convective sampling densities. Density is determined using a 10.0 ppbv x 0.5 km bin resolution for CO and a 1.0 ppmv x 0.5 km bin resolution for H_2O. For the 31 May 2022 convective samples, every 5th H_2O measurement is shown to be more consistent with the frequency of CO, which results in no loss of qualitative detail. Measurements obtained when skimming the anvil near the tropopause and during the vertical profile are annotated. 64

4.1 Maximum azimuth-averaged 10-m horizontal wind speed within 500 km of TC center throughout the model run time of 192 hours for all simulations, with hurricane categories 1-5 shaded and annotated based on the Saffir-Simpson Hurricane Wind Scale. 71

4.2 Average profiles of (top-to-bottom) H_2O, boundary layer passive tracer: PT_{bl}, and stratospheric passive tracer: PT_{strat} from (left-to-right) 0-300 km, 300-1000 km, and 0-1000 km. In each panel, the approximate tropopause altitude is shown by the dashed black line, initial model profiles are shown by the thick gray line, and remaining colored lines represent end-of-simulation averages for $TC_{noshear}$ (yellow), TC_{shear} (orange), and TC_{lowSST} (blue). 73

4.3 Overshoot count (cloud tops reaching or exceeding 17.56 km) (left) spatial distribution, and (right) timeseries for the total TC domain (solid line) and inner 150 km from TC center (dashed line) for $TC_{noshear}$ (a,b), TC_{shear} (c,d), and TC_{lowSST} (e,f). The inner 150 km of the TC is indicated by the cyan circle (a,c,e). 75

4.4 Constant-altitude TC-centered plots of $TC_{noshear}$ of (left-to-right) H_2O at 17.56 km, boundary layer passive tracer (PT_{bl}) at 17.56 km, stratospheric passive tracer (PT_{strat}) at 15.56 km, and convective passive tracer (PT_{conv}) at 17.56 km for (top-to-bottom) hours 83, 126, and 152 of simulation time. The black contour outlines the cloud boundary (sum of cloud and ice mixing ratios is greater than 1.0×10^{-6} kg kg^{-1}). 77

4.5 For H_2O in $TC_{noshear}$, (a) space-time diagram at an altitude of 17.50 km, in coordinates of distance from TC center and simulation time, and (b-d) storm-average curtains of H_2O in distance from TC center and altitude at hours 106, 144, and 192, respectively. Storm averaging occurs in 4-km radial bins over all 360 degrees of the TC. 79

4.6 Vertical cross-sections of water vapor (H_2O; ppmv) in $TC_{noshear}$ at hour 106 (a), 115 (b), 144 (c) and 167 (d). Potential temperature contours are shown in black in each panel in 10 K intervals (with solid contours for 380 K and above, and dashed below). The orange contour shown in each panel is the potential temperature of the environmental tropopause (383 K).The cross-section is taken through the meridional center of the TC, going from west to east. 80

4.7 As in Figure 4.5, but for temperature anomalies in $TC_{noshear}$. 82

4.8 Vertical temperature profiles in $TC_{noshear}$ at distances from TC center of 50 km (red), 100 km (blue) and 200 km (black) for hour 48 (a), 96 (b), 144 (c), and 192 (d). The initial TC temperature profile is shown in gray in all panels. 83

4.9 As in Fig. 4.6, but for the percentage of convective passive tracer (PT_{conv}) in $TC_{noshear}$. 84

4.10 As in Figure 4.5, but for the percentage of boundary layer passive tracer (PT_{bl}) in $TC_{noshear}$. 85

4.11 As in Figure 4.6, but for the percentage of boundary layer passive tracer (PT_{bl}) in $TC_{noshear}$. 86

4.12 As in Figure 4.5, but for the percentage of stratosphere passive tracer (PT_{strat}; stratospheric air) in $TC_{noshear}$. 87

4.13 As in Figure 4.6, but for the percentage of stratosphere passive tracer (PT_{strat}) in $TC_{noshear}$. Blue arrows indicate the local maxima of stratospheric air advected radially outward from the TC. 88

4.14 Illustration of the evolution of TC convective outflow in $TC_{noshear}$ from (a) an intensifying hurricane and to (b) a mature major hurricane, and its impact on downward transport of stratospheric air. Notable aspects of the outflow evolution include the secondary circulation deepening and strengthening as the storm intensifies, resulting in the eyewall convection and outflow impinging upon the tropopause. 89

4.15 Vertical cross-sections of TC_{lowSST} taken from west to east through the meridional center of the TC. These include (H_2O; ppmv, (a,b)), percentage of boundary layer passive tracer (PT_{bl} (c,d)), percentage of stratospheric passive tracer (PT_{strat} (e,f)), and percentage of convective passive tracer (PT_{conv} (g,h)) at Category 2 (left) and 4 (right) hurricane intensity, respectively. Potential temperature contours are shown in black in each panel in 10-K intervals (with solid contours for 380 K and above, and dashed below). The orange, yellow, or pink contour shown in each panel is the potential temperature of the environmental tropopause (383 K). 92

4.16 Vertical cross-sections of water vapor (H_2O; ppmv) category 4 hurricane intensity for $TC_{noshear}$ (a; hour 115) and TC_{shear} (b; hour 155). Potential temperature contours are shown in black in each panel in 10-K intervals (with solid contours for 380 K and above, and dashed below). The orange contour shown in each panel is the potential temperature of the environmental tropopause (383 K).The cross-section is taken from west to east through the meridional center of the TC. 94

4.17 Storm-average curtains of temperature anomalies in distance from TC center and altitude at Category 4 hurricane intensity for $TC_{noshear}$ (a) and TC_{shear} (b). Storm averaging occurs in 4-km radial bins over all 360 degrees of the TC. 95

4.18 For H_2O, space-time diagram at an altitude of 17.50 km for the upshear left (a), downshear left (b), upshear right (c), and downshear right (d) quadrants. The arrow indicates the direction of the VWS vector. Storm averaging occurs in 4-km radial bins over the TC. 96

4.19 As in Figure 4.19, but for the percentage of boundary layer passive tracer (PT_{bl}; boundary layer air) at 17.0 km. 97

4.20 Constant-altitude TC-centered plots of stratospheric passive tracer (PT_{strat}) at 15.56 km for $TC_{noshear}$ at category 3 (a) and category 5 (b) intensity and TC_{shear} at category 2 (c) and category 4 (d) intensity. The black contour outlines the cloud boundary (sum of cloud and ice mixing ratios is greater than 1.0×10^{-6} kg kg^{-1}). 99

4.21 As in Figure 4.19, but for the percentage of stratosphere passive tracer (PT_{strat}; stratospheric air) at 15.5 km. 100

5.1 Number of ROMEX profiles included in each 100 km bin from TC center for all extracted TC profiles (black), hurricane (red), and tropical storm (blue) profiles. 107

5.2 Extracted ROMEX profiles for three example storms included in ROMEX data: Tropical Storm Madeline (orange), Hurricane Fiona (cyan) and Very Strong Typhoon Noru (red). TC track points are indicated by black X's. Selected profiles are only equatorward of 30 deg. N, as indicated by the gray box. 107

5.3 ROMEX RO temperature anomalies for (a) all extracted TC profiles, (b) hurricane profiles, and (c) tropical storm profiles. Anomalies are calculated in 100 km bins, relative to far-field temperatures. The black dashed line is the lapse-rate tropopause. 110

5.4 Mean temperature anomaly profiles (a) from 0-900 km for non-TC profiles (black), tropical storms (blue) and hurricanes (red). Dashed lines indicate plus or minus the standard error. Temperature variance (b) from 0-900 km for non-TC profiles (black), tropical storms (blue), and hurricanes (red). 111

5.5 **Anomaly structure present for individual storms.** As in Figure 5.3, but for individual storms with ROMEX(left) and ERA5 (right) for Hurricane Fiona (a,b), Tropical Storm Madeline (c,d) and Very Strong Typhoon Noru (e,f). 112

5.6 ERA5 TC temperature anomalies and gradient wind balance contoured in gray for all extracted TC profiles. Solid gray lines indicating positive gradient wind values and dashed contours indicating negative. The tropopause is indicated by the solid black line. 113

5.7 ROMEX temperature variance for: (b) all identified TC profiles, (b) non-TC profiles. High temperature variance indicates gravity wave activity. The yellow line is the tropopause. 115

Abstract

The troposphere and stratosphere are two layers of the atmosphere with distinct composition and dynamics, separated by the tropopause region. Exchange between these layers, known as stratosphere-troposphere exchange (STE) occurs often, when dynamical processes impact the tropopause region. STE alters the composition and thermodynamics of the upper troposphere and lower stratosphere (UTLS), which irreversibly modifies the distribution of greenhouse gases, such as water vapor (H_2O) and ozone (O_3). This change in greenhouse gas distribution affects the radiation budget and is therefore important for Earth's climate. UTLS composition change occurs through multiple STE processes at various temporal and spatial scales. Tropopause-overshooting convection is the most rapid of such processes, as it enables irreversible mixing between the troposphere and stratosphere through the transport of air in minutes to hours. Previous efforts examining the contribution of overshooting convection to the lower stratospheric H_2O budget have primarily considered the tropics, but more frequent and deeper midlatitude overshooting convection has gained increasing attention. Midlatitude overshooting convection can result in the formation of above-anvil cirrus plumes (AACPs) that result in extreme hydration of the stratosphere. While tropical convection has received most prior attention with respect to stratospheric H_2O, tropical cyclones (TCs) remain understudied for their contribution to convection-driven UTLS composition change and compared to other recognized STE processes. Given that TCs often have long transit paths have a relatively longer lifetimes (days to weeks), TC-driven UTLS composition change could have unique impacts on the climate system compared to storms that are short-lived. Nonetheless, all convective phenomena pose unique challenges towards understanding their contributions to STE given tropopause

altitude, wind shear, tropospheric instability, and stratospheric stability in convective environments are known to vary considerably and impact transport occurrence and/or efficiency. This dissertation seeks to improve understanding of convection-driven STE and concomitant UTLS composition change through isolating several of these interdependencies.

The first component of this dissertation utilizes idealized simulations to improve understanding of how the lower stratospheric environment can impact cross-tropopause transport from midlatitude overshooting convection. Previous work has primarily focused on troposphere-to-stratosphere transport (TST) rather than stratosphere-to-troposphere transport (STT), including for AACP-producing storms which are recognized to have unique dynamics. Understanding of how transport driven by overshooting convection and AACP properties are modified by variations in UTLS environments is limited, especially that for the extent of STT (i.e., downward) transport. Therefore, AACP development and UTLS transport sensitivities to lower stratosphere stability and the UTLS wind environment are evaluated using four idealized simulations. Varying these attributes results in overshooting storms with and without AACPs, each including a single and double tropopause. It is found that greater TST and stratospheric hydration occurs in storms with AACPs, while STT is greater in storms without AACPs. This STT is facilitated by a mechanical oscillation induced by the overshoot. AACP-producing storms have increased downward transport of stratospheric overworld air to the lowermost stratosphere, which is enhanced within a double tropopause environment. More expansive AACPs, deeper overshoots, and greater TST also occurs in double tropopause environments.

The second component of this dissertation uses recent observations to examine STE and UTLS composition change within an active AACP-producing storm. In particular, novel in situ observations from the NASA Dynamics and Chemistry of the

Summer Stratosphere (DCOTSS) field campaign are used to examine UTLS impacts from AACP-generating overshooting convection. The DCOTSS research flight on 31 May 2022 sampled active convection over the state of Oklahoma for more than three hours with the NASA ER-2 high-altitude research aircraft. An AACP was bisected during this flight, providing the first such extensive in situ sampling of this phenomenon. The convective observations reveal pronounced changes in air mass composition and stratospheric hydration up to altitudes 2.3 km above the tropopause and concentrations more than double background levels. Unique dynamic and trace gas signatures were found within the AACP, including enhanced vertical mixing near the AACP edge and a positive correlation between H_2O and O_3. Moreover, the H_2O enhancement within the AACP was found to be limited to the saturation mixing ratio of the low temperature overshoot and AACP air. Comparison with all remaining DCOTSS flights demonstrates that the 31 May 2022 flight had some of the largest tropospheric tracer and H_2O perturbations in the stratosphere and within the AACP.

The third component of this dissertation examines the contributions of identified STE processes within TCs to STE and how STE varies with important TC environmental factors using simulations. Prior work examining TCs and the stratosphere has been limited to coarse spatial resolution, specific ocean basins, or short time periods, resulting in limited understanding of fine-scale processes impacting UTLS composition change. Previous case studies have identified multiple STE processes within TCs, but it remains unclear how these individual processes contribute to the total STE in TCs and vary with common TC environmental factors. To improve upon these limitations, three idealized simulations are executed and analyzed to provide a more thorough understanding of the importance of STE in TCs, the role of various STE processes, and their sensitivity to different TC environmental factors, including sea surface temperature (SST) and deep-layer vertical wind shear (VWS). The simulations suggest

substantial hydration of the lower stratosphere occurs within the TC inner core. H_2O enhancements reach greater altitudes and magnitudes with no VWS, but a greater spatial extent beyond the inner core when VWS is included. Overshooting eyewall convection is the dominant stratospheric hydration process, and near-tropopause cooling is an important constraint for hydration. The shallower TC that develops with a lower SST facilitates less TST than the other simulations, but similar STT. Downward transport of stratospheric air occurs i) within the upper portion of the near-tropopause outflow and ii) via subsidence within the eye.

The final component of this dissertation evaluates observations of TC impacts on temperature in the UTLS and middle stratosphere. There are limited observations within TCs and their environments over the open ocean to confirm model outcomes, such as TC impacts on temperature structure and concomitant H_2O transport in the UTLS. Satellite-based radio occultation (RO) data offer a modern global observational pathway for fine-scale evaluation UTLS temperatures, of which a special collection of RO data during a Northern Hemisphere TC season, the Radio Occultation Modeling Experiment (ROMEX), is used to investigate UTLS temperature impacts of TCs. ROMEX is particularly transformative as RO data from all operational public and private satellites was made publicly available resulting in nearly 5X as much data and far more profiles per individual TC than that otherwise available in the recent RO record (since late 2019). Here, ROMEX profiles are extracted along TC tracks in the North Atlantic, East Pacific, and West Pacific basins to extensively evaluate observed TC-induced UTLS temperature change. Robust temperature anomalies are seen, including the expected tropospheric warm core and tropopause cooling, along with at least two higher-altitude stratospheric features revealed for the first time: cooling near 20 km and warming near 30 km. This analysis suggests that TCs perturb the middle atmosphere far deeper than previously recognized. The ubiquitous cold and warm layers in

the low-to-middle stratosphere are found to be insensitive to most considered TC and environmental factors, however, impacts are larger in weaker TCs. These anomalies are similarly captured in ERA5 reanalysis data. The inferred deep stratospheric circulations may have impacts on TC evolution and forecasting that are not captured in current simulations.

This dissertation seeks to provide insight towards the importance of environmental factors on convection-driven STE in the midlatitudes and tropics. In particular, this dissertation examines the dynamical and physical processes leading to STE in midlatitude AACP-producing storms and their sensitivity to the lower stratospheric environment, how individual processes contribute to STE in TCs and how they vary by TC intensity and shear, and how TCs impact temperature in the UTLS and middle stratosphere. Overall, this dissertation has shown that environmental factors, such as thermodynamic and dynamic characteristics, have considerable influence on STE driven by high-impact convective phenomena. One such characteristic is wind shear, as it impacts STE for both AACP-producing storms and TCs. This dissertation has also emphasized that UTLS temperature is an important constraint for transporting H_2O in convective phenomena in the midlatitudes and tropics.

Chapter 1

Introduction

The tropopause is often viewed as a sharp boundary separating the troposphere and stratosphere. However, the tropopause region is routinely impacted by dynamical processes that lead to exchange between the troposphere and stratosphere, known as stratosphere-troposphere exchange (STE). This exchange can modify the thermodynamics and composition of a variably deep layer that is commonly referred to as the upper troposphere and lower stratosphere (UTLS). STE-induced composition change in the UTLS irreversibly modifies the distribution and concentration of greenhouse gases such as water vapor (H_2O) and ozone (O_3), which impact radiative forcing and climate (Holton et al., 1995; Stohl et al., 2003). For instance, the radiative forcing by H_2O in the UTLS is most sensitive to changes in the extratropical lowermost stratosphere (Solomon et al., 2010; Banerjee et al., 2019), while that for O_3 is most sensitive to changes in the upper troposphere (Lacis et al., 1990).

STE occurs through multiple transport processes at various spatial and temporal scales including: the Brewer-Dobson Circulation (Brewer, 1949; Dobson and Massey, 1956; Salby and Callaghan, 2006), Rossby wave breaking and isentropic transport (Postel and Hitchman, 1999; Hitchman and Huesmann, 2007; Homeyer and Bowman, 2013), tropical cyclones (Ray and Rosenlof, 2007; Danielsen, 1993; Baray et al., 1999), extratropical cyclones and warm conveyor belts (Wernli and Bourqui, 2002; Eckhardt et al., 2004), tropopause folds and stratospheric intrusions (Appenzeller and Davies, 1992; Cooper et al., 2004; Browell et al., 1987), and overshooting convection (Poulida et al.,

1996; Hanisco et al., 2007; Dessler and Sherwood, 2004). The most rapid of these processes, tropopause-overshooting convection (hereafter "overshooting convection"), facilitates transport of air from the lower troposphere to the UTLS in minutes to hours and can enable irreversible mixing between these layers. The contribution to the global lower stratosphere H_2O budget from overshooting convection is currently estimated to range from 10–15%, based on several studies using output from convection-resolving model simulations and observations of storms with a trajectory model driven by large-scale winds (Dauhut and Hohenegger, 2022; Dessler and Sherwood, 2004; Tinney and Homeyer, 2021; Ueyama et al., 2023). This is likely an underestimation, as most existing efforts to quantify the lower stratosphere H_2O budget only consider effects from tropical convection. However, there has been increasing attention towards midlatitude convection contributions to the lower stratosphere H_2O budget, due to its observed frequency and depth (Khaykin et al., 2009; Liu and Liu, 2016; Liu et al., 2020; Werner et al., 2020).

Tropical cyclones (TCs) are another identified, but less explored, convective phenomena that facilitates STE. TCs have different organization and structure than midlatitude overshooting convection, given that they contain a multitude of convective elements as opposed to a singular dominant storm. UTLS composition changes resulting from TCs could have a unique impact on the climate system due to their relatively long lifetime compared to shorter-lived storms (days to weeks compared to hours) and often long transit paths.

Convective phenomena pose unique challenges towards understanding their contributions to STE given their variability in intensity, organization, and other interactions with the variety of environments they occur in. Specifically, tropospheric instability, tropopause altitude, wind shear, and stratospheric stability are known to vary considerably for both midlatitude overshooting convection and TCs which could influence the

amount of STE associated with these storms. Therefore, improved understanding of convection-driven STE and accompanying UTLS composition impacts requires an analysis approach that isolates some of these inter-dependencies. As such, this dissertation addresses the impact of several key environmental factors on STE in midlatitude overshooting convection and TCs using simulations and observations. Detailed background and motivation for each thematic focus is provided in the remaining sub-chapters of this Introduction.

1.1 Midlatitude Overshooting Convection

In addition to being recognized as the most rapid STE pathway, overshooting convection is also commonly associated with severe weather in the midlatitudes, as these storms often produce hazards including hail, tornadoes, and strong winds (Fujita, 1974; Brunner et al., 2007; Bedka, 2011; Dworak et al., 2012; Bedka et al., 2015, 2018; Marion et al., 2019; Sandmæl et al., 2019). Tropopause-overshooting convection occurs worldwide and is most frequent over land in the midlatitudes, especially in North and South America (Liu and Liu, 2016; Liu et al., 2020; Clapp et al., 2023; Nugent and Bretherton, 2023). The United States, specifically the Great Plains region, has been recognized as a unique hotspot of deep and frequent overshooting based on satellite and radar observations (Solomon et al., 2016; Cooney et al., 2018; Homeyer and Bowman, 2021). Overshooting convection in the United States is most frequent in the warm season (March-August), with an annual cycle that sharply peaks in late spring and early summer along with a diurnal cycle that peaks near sunset. Approximately half of overshooting convection in the United States reaches the stratospheric overworld (potential temperature (θ) $>$ 380 K; Cooney et al., 2018), where the impacts from these events on the stratosphere can last weeks to months as this air will take longer to

descend back to the troposphere in the midlatitudes (Holton et al., 1995). Additionally, air that reaches the stratospheric overworld can be isentropically transported toward the tropics where it may enter the the upward branch of the Brewer-Dobson circulation, further extending its stratospheric lifetime (Chang et al., 2023). In a warming climate, the frequency of severe thunderstorm environments favorable for overshooting convection is projected to increase (Del Genio et al., 2007; Trapp et al., 2007). Furthermore, overshooting convection increased by over 250% across the domain of a pseudo-global warming model simulation, with an increase in frequency of extreme tropopause-relative heights exceeding 4 km above the tropopause (Tinney et al., 2024).

Known impacts of tropopause-overshooting convection on the UTLS are detailed in some cases and more general in others. For example, a key storm feature commonly associated with midlatitude tropopause-overshooting convection is the above-anvil cirrus plume (AACP). AACPs are cirrus clouds that reside above the anvil and are commonly identified in visible and infrared (IR) satellite imagery (Wang, 2003; Luderer et al., 2007; Wang et al., 2016; Homeyer et al., 2017). When AACPs appear warm relative to the underlying anvil cloud in IR imagery, this indicates stratospheric injection of cloud ice and subsequent hydration via sublimation (Murillo and Homeyer, 2022). These plumes are known to be driven by gravity wave breaking near and within the overshooting top in environments with strong storm-relative winds (the difference between the environmental wind and storm motion) in the UTLS, which is associated with the establishment of a hydraulic jump (Wang, 2003; Luderer et al., 2007; Wang et al., 2016; Homeyer et al., 2017; O'Neill et al., 2021). This hydraulic jump occurs near the tropopause and downstream of the overshooting top, where the overshooting top acts as a topographic obstacle. These AACPs have been studied for their influence on UTLS composition and relationship to severe weather, which have been demonstrated to be the most extreme among all overshooting storms (Bedka et al., 2018). While our

appreciation is increasing for the role of various storm and environmental characteristics in overshooting and cross-tropopause transport (including whether an AACP is produced), most prior observational work does not consider such characteristics when evaluating the UTLS impacts associated with these storms.

UTLS composition impacts from overshooting convection have been explored broadly via satellite observations (Randel et al., 2012; Schwartz et al., 2013; Smith et al., 2017; Werner et al., 2020; Tinney and Homeyer, 2021) and specifically using aircraft observations of individual cases (Poulida et al., 1996; Fischer et al., 2003; Fromm and Servranckx, 2003; Hegglin et al., 2004; Frey et al., 2015; Hanisco et al., 2007; Homeyer et al., 2011; Anderson et al., 2012; Homeyer et al., 2014b; Pan et al., 2014; Herman et al., 2017; Smith et al., 2017; Khaykin et al., 2022). These studies have shown that H_2O in the UTLS is enhanced through both sublimation of ice and air mass transport, and that H_2O and additional tropospheric and stratospheric trace gases are modified up to 4 km above the tropopause. Meanwhile, STE of more passive tropospheric and stratospheric compounds (e.g., O_3 and carbon monoxide (CO)) is largely confined to within 1–3 km above/below the tropopause altitude.

Stratospheric hydration from convection has been encountered in a few prior field campaigns including: the SCOUT-AMMA aircraft campaign over Africa (Khaykin et al., 2009), the Aura Validation Experiment (AVE) aircraft campaign over the United States (Hanisco et al., 2007; Anderson et al., 2012; Smith et al., 2017), the Studies of Emissions, Atmospheric Composition, Clouds and Climate Coupling by Regional Surveys (SEAC4RS) aircraft campaign over the United States (Smith et al., 2017), and the Deep Convective Clouds and Chemistry (DC3) field campaign over the United States (Homeyer et al., 2014b; Pan et al., 2014). The majority of convective encounters within these field campaigns were serendipitous rather than targeted. The SEAC4RS campaign targeted convective outflow from an AACP-producing storm that occurred ∼20

hours prior to flight, detailed in Smith et al. (2017). In situ data were used to estimate that between 6.6 and 13.5 kilotonnes of H_2O was irreversibly delivered to the lower stratosphere from this convective system. Most airborne observations of overshooting convection and UTLS impacts are associated with recent (less than 36 hours between overshooting and sampling) or aged convection (longer than 36 hours between overshooting and convection) rather than active convection (measurements in or near an active convective complex with co-located cloud observations, which can range from minutes to a few hours old), especially within the lower stratosphere. The DC3 field campaign had active convection targeting, which occurred primarily in the upper troposphere. The GV and DC-8 aircraft used during DC3, however, did encounter convectively injected H_2O at altitudes up to 1–2 km above the tropopause near active overshooting convection during a flight on 20 May 2012, detailed in Homeyer et al. (2014b). H_2O enhancements exceeded 200 ppmv above background concentrations in the lower stratosphere, with evidence of extensive mixing between troposphere and stratosphere air within this broad H_2O enhancement. Additionally, an AACP was briefly encountered within this flight, measured at a distant range from the parent overshoot for approximately 30 seconds.

As past observations of overshoot-influenced air are limited, much of the current understanding of the impact of overshooting convection on the UTLS and physical and dynamical processes driving STE has been gleaned from numerical model simulations. These simulations have shown that mass exchange across the tropopause from overshooting convection has a significant role in changes of the composition and chemistry of the UTLS (Homeyer et al., 2014a). Irreversible exchange can occur through gravity wave breaking in and near the overshooting top (as previously mentioned to be critical for AACP formation), Kelvin-Helmholtz instabilities near cloud top, and tropopause-level shallow continuity circulations coupled with differential advection (Pan et al.,

2014; Homeyer et al., 2017; Phoenix et al., 2020; O'Neill et al., 2021). Additionally, the amount of overshooting convection and cross-tropopause transport in simulations exhibits several sensitivities to storm characteristics (e.g., mode - discrete supercell versus mesoscale convective system or MCS) and to the characteristics of the lower stratospheric environment, such as stability and the strength of storm-relative winds (Mullendore et al., 2005; Bigelbach et al., 2014; Homeyer et al., 2014a; Starzec et al., 2020). An isolated supercell tends to have a larger updraft and deeper overshooting compared to alternative storms, while an MCS has a large number of weaker overshoots that can achieve greater overall transport and STE (Mullendore et al., 2005). The lower stratosphere environment can help to constrain the depth and area of overshooting through differences in stability, such that environments with lower stability (weaker temperature lapse rates) enable deeper overshooting (Homeyer et al., 2014a). In the midlatitudes, the largest reductions in lower stratosphere stability (relative to normal) and thus impacts on overshoot depth typically occur within double tropopause environments, where the temperature above the primary tropopause decreases substantially over a layer several kilometers deep up to the altitude of a secondary tropopause typical of that found in the tropics (Homeyer et al., 2014a; Solomon et al., 2016).

The amount of STE from overshooting convection also appears to depend on the height of the tropopause and, more generally, UTLS temperature (Phoenix and Homeyer, 2021). A lower UTLS temperature is an important constraint for stratospheric hydration, while a higher tropopause also impacts air mass transport as it is harder to reach and allows for greater cumulative diluting effects on air within the convective updraft that result from entrainment of environmental (free troposphere) air. Within these known sensitivities, multiple simulations have shown that H_2O enhancements have appeared to reach higher altitudes than passive tropospheric tracers (Homeyer, 2015; Phoenix and Homeyer, 2021). Furthermore, recent numerical modeling studies

have identified the unique influence of AACP-producing storms on UTLS composition (O'Neill et al., 2021). Many of these modeling results have yet to be verified by observations, including H_2O enhancements routinely reaching greater altitudes.

Of all impacts to UTLS composition from tropopause-overshooting convection, troposphere-to-stratosphere transport (TST) has received the most attention in previous work (including both the upward transport of boundary layer air and stratospheric hydration via ice). There is comparatively limited understanding of the extent of stratosphere-to-troposphere transport (STT) occurring within these storms and its sensitivity to storm and environment characteristics. One known mechanism for STT is anvil-wrapping in MCSs, where stratospheric air (high in O_3) is transported downward to the upper troposphere around the anvil edge (Poulida et al., 1996; Pan et al., 2014; Phoenix et al., 2020). Apart from this mechanism, however, the extent of STT in tropopause-overshooting convection is not well understood. AACPs are known to develop due to unique dynamics (a hydraulic jump and strong storm relative winds in the UTLS conducive to gravity wave breaking; O'Neill et al., 2021; Homeyer et al., 2017), but it is unknown if AACP-producing storms facilitate STT differently than a non-AACP overshooting storm. Environmental attributes in the UTLS, such as tropopause height and temperature, have been recognized to impact transport, but their influence on AACP-producing storms and accompanying transport is not well understood. Although AACP-producing storms have been suggested to facilitate unique impacts on the UTLS, this has not been robustly verified with observations as past observations of overshooting convection have been sparse.

Motivated by this limited understanding and perceived outsized importance of AACP-producing storms, idealized simulations and novel in situ airborne observations are utilized to explore the unique impact of AACPs on two-way transport and resulting UTLS composition change. The simulations also explore how AACP-producing

storm impacts are sensitive to characteristics of the lower stratospheric environment. Specifically, this dissertation aims to address the following questions:

1. How is the UTLS composition altered near/during active overshooting convection and AACPs?

2. What dynamical/physical processes could contribute to these changes in UTLS composition, including whether a storm produces an AACP?

3. How is two-way STE sensitive to the dynamic and thermodynamic characteristics of the lower stratosphere environment?

All questions are addressed at varying depth using idealized simulations in Chapter 2 and novel in situ airborne observations in Chapter 3. Work included in Chapter 2 is published in Gordon and Homeyer (2022) and work included in Chapter 3 is published in Gordon et al. (2024).

1.2 Tropical Cyclones

TCs are commonly recognized for their damaging hazards when they make landfall, including severe winds, excessive rainfall, and storm surge flooding, and have an expansive range of impacts on the climate system. TCs and their potential climate feedbacks have received increasing attention over the past several decades (Walsh et al., 2019; Knutson et al., 2019; Evans et al., 2017). One probable, but under-investigated, climate impact of TCs is UTLS composition change facilitated by STE. A warming climate is expected to result in an increase in TC intensity, due primarily to increasing atmospheric and sea surface temperatures (SSTs; Walsh et al., 2019). As TC intensity increases, the primary and secondary circulations of the TC accelerate and may subsequently impact the distribution and significance of STE processes. The intensity of

convective elements embedded within TC as revealed by observed radar echo strength and echo top height are also known to increase as TC intensity increases (Hence and Houze, 2011). More broadly, specific structural characteristics that are likely to change include the strength of the warm core and subsidence within the eye, and the extent of eyewall convection (Holland and Merrill, 1984; Houze, 2010).

Environmental deep-layer vertical wind shear (VWS), the vector difference between horizontal winds at 200 and 850 hPa, has been studied for its influence on TCs using idealized simulations and observations, such as airborne Doppler radar and dropsondes (Reasor et al., 2013; Hence and Houze, 2011; Nguyen et al., 2019; Frank and Ritchie, 2001; Rios-Berrios et al., 2024). VWS has been recognized to weaken TC intensity and alter TC structure by creating azimuthal asymmetries in convection (Corbosiero and Molinari, 2002; Rios-Berrios and Torn, 2017). Namely, VWS is recognized to tilt the vortex from its upright position (Jones, 1995) and facilitate stronger convection in the downshear half of the TC (Corbosiero and Molinari, 2002; Reasor et al., 2013). Specifically, the downshear left quadrant has been shown to have a maximum in vertical velocity within buoyant updrafts, resulting in the most intense convection and a precipitation maximum (Corbosiero and Molinari, 2002; Nugent and Rios-Berrios, 2018). Meanwhile, deep convection and precipitation are greatly reduced in the upshear quadrants (Corbosiero and Molinari, 2002; Hence and Houze, 2011). VWS is recognized as one of the most influential external factors on TC structure (Rios-Berrios et al., 2024), however its impacts on STE processes in TCs is unknown.

Previous studies have explored UTLS composition impacts within TCs using aircraft (Danielsen, 1993; Baray et al., 1999; Roux et al., 2020), satellite observations (Ray and Rosenlof, 2007; Jiang et al., 2020; Fagan and Homeyer, 2025), and model simulations (Allison et al., 2018; Preston et al., 2019; De Bellevue et al., 2006). UTLS composition change is sensitive to TC intensity, with stronger storms facilitating greater

change (Fagan and Homeyer, 2025), but it is unknown how STE processes facilitating this transport may change with varying intensities. O_3 can be transported down to the upper troposphere in the eye and near TC outflow (De Bellevue et al., 2006; Baray et al., 1999). TCs have been shown to hydrate the upper troposphere by up to 50% above mean H_2O mixing ratios using satellite measurements from the Atlantic and Pacific Ocean basins (Ray and Rosenlof, 2007). Enhanced H_2O has also been observed to reach the lower stratosphere (82 hPa) near TCs in the Indian Ocean using satellite observations (Ratnam et al., 2016). UTLS change in H_2O has been shown to be sensitive to deep layer VSW, as Fagan and Homeyer (2025) saw greater hydration downshear (upshear) when shear was strong (weak) in global satellite observations. TCs can also result in dehydration near the tropopause, as seen in satellite observations and convection-resolving simulations (Jiang et al., 2020; Allison et al., 2018; Fagan and Homeyer, 2025). This is likely due to TC-driven tropopause temperature decreases and the layer being supersaturated with respect to ice. A portion of these ice particles will be injected into the lower stratosphere and sublimate, which hydrates the layer (Jiang et al., 2020). However, the typical extent of near-tropopause and stratospheric hydration and dehydration processes in TCs is not well understood. Previous studies have been limited to specific ocean basins or short time periods, few observations at altitudes of interest, and coarse spatial resolution which makes it difficult to capture fine-scale processes impacting hydration and dehydration.

Multiple STE processes within TCs identified in past case studies are shown in Fig. 1.1, and include: i) isentropic transport and mixing of cloud and tropospheric air from the inner TC core into the surrounding lower stratosphere (Danielsen, 1993), ii) downward transport of stratospheric air near and below the edge of tropopause-level TC outflow (Baray et al., 1999; De Bellevue et al., 2006), iii) two-way exchange in and near overshooting tops (cloud tops exceeding the tropopause; Allison et al., 2018;

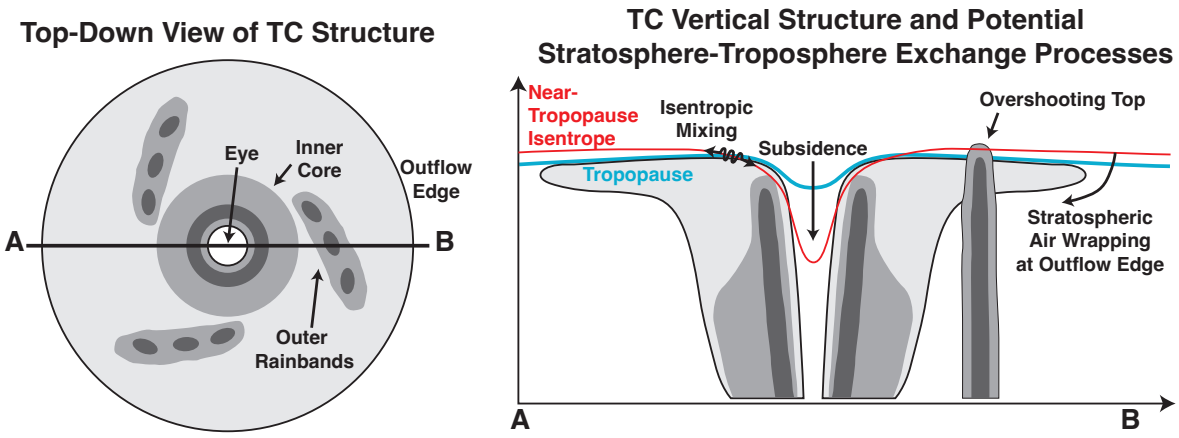


Figure 1.1: Illustration of (left) top-down view of a tropical cyclone and (right) vertical cross section of a tropical cyclone with known stratosphere troposphere exchange processes. These processes include: isentropic mixing, subsidence, two exchange facilitated by overshooting tops, and apparent stratospheric air wrapping at outflow edge. The tropopause is annotated in blue and near-tropopause isentrope is annotated in red.

Preston et al., 2019), and iv) subsidence of stratospheric air within the eye of the TC (Newell et al., 1996; Zou and Wu, 2005; Ratnam et al., 2016). Isentropic transport of troposphere air to the stratosphere is suggested to occur due to a combination of TC-driven UTLS temperature change (cross-tropopause "bending" of isentropes) and the prevailing TC secondary circulation, based on in situ airborne observations from the Stratosphere-Troposphere Exchange Project (STEP) field campaign (Danielsen, 1993). For the downward transport of stratospheric air near tropopause-level TC outflow process, Baray et al. (1999) suggested measurements of O_3 by Airbus In-Service Aircraft (MOZAIC) data near TC Marlene showed O_3 rich stratospheric air is transported downward around and below the tropopause-level TC outflow and into the troposphere (Baray et al., 1999; De Bellevue et al., 2006). Specifically, measurements showed a peak O_3 concentration of 300 ppbv at 300 hPa, which exceeds typical observations in the upper troposphere by $\sim$200% and suggests the presence of stratospheric air, especially given its coincidence with low relative humidity (Baray et al., 1999).

Transport from overshooting convection leads to enhanced H_2O and CO in the stratosphere, based on simulated TC eyewall convection and outer rainbands (Allison et al., 2018; Preston et al., 2019), with the greatest contributions to STE near the eyewall (Preston et al., 2019). Preston et al. (2019) also found that overshooting convection contributes more to H_2O transport than CO (per area) using a simulation and airborne observations of Typhoon Mireille. It has also been found that ∼15% of overshooting convection in the tropics occurs in TCs (Jiang and Tao, 2014; Romps and Kuang, 2009). Subsidence within the TC eye has been explored with satellite observations in the north Indian Ocean, as enhanced O_3 (+∼200 ppbv) in the upper troposphere reached as low as 146 hPa (13–14 km; Ratnam et al., 2016).

Despite its recognized importance for STE of H_2O, historically few observations exist at fine resolution and in close proximity to a TC throughout its lifecycle over the open ocean to enable detailed evaluation of UTLS temperature structure. Global navigation satellite system radio occultation (RO) data offer a modern observational approach for examining TC impacts on UTLS temperature at high vertical resolution (<500 m). TC temperature structure is well recognized to be distinguished by a warm core in the mid-to-upper troposphere and a narrow cold layer near the tropopause. This cooling results in a temperature structure that resembles a double tropopause (Biondi et al., 2015). Near-tropopause cooling in TCs has been explored using RO measurements and shown to increase in magnitude with TC intensity and vary by ocean basin (Rivoire et al., 2016; Biondi et al., 2013, 2015). The near-tropopause cold layer is linked to dynamically-balanced circulations and convective ascent (Rivoire et al., 2020); cloud radiative effects reinforce the cooling but are not the primary mechanism. An important limitation of prior work examining UTLS temperature change in TCs is that analyses have focused on altitudes below 20 km. However, modern RO observations allow for robust examination of impacts to altitudes as high as 40 km.

TCs have received comparatively less attention for their impacts on the UTLS than other STE pathways, such as overshooting convection. Given that TCs have longer lifetimes and are a larger system with multiple convective elements, it is important to increase understanding of STE processes within TCs and their sensitivity to varying environmental factors. Previous work has examined UTLS composition change from TCs (Ray and Rosenlof, 2007; Fagan and Homeyer, 2025), but there has been limited focus on STE mechanisms leading to this composition change. Multiple distinct STE processes that can occur have been identified in prior case studies, but the importance of each to STE in TCs and relationship to important TC environmental factors, such as sea surface temperature (SST) and VWS, is unknown. Although it is common to use convection-resolving simulations to study TCs, these are rarely used to explore STE and transport in TCs. Prior simulations have explored TCs and transport in the UTLS, but most are too coarse to resolve convection (10 km, e. g. Das et al. (2016)) apart from a couple based on real events (Allison et al., 2018; Preston et al., 2019). Idealized simulations are a preferred method to increase process-level understanding of STE in TCs and explore how STE is sensitive to varying environmental factors with fixed complexity.

To improve upon the limitations of prior work and deepen understanding of TC impacts on the UTLS, this dissertation utilizes idealized simulations and a special collection of RO observations to increase process-level understanding of STE in TCs, TC impacts on the UTLS, and accompanying sensitivities to TC environmental characteristics. Specifically, this dissertation aims to address the following questions:

1. How do individual processes in TCs contribute to STE?,

2. How do intensity and deep-layer wind shear impact STE in TCs?

3. What do high-resolution observations reveal about TC impacts on UTLS tem-

perature?

Questions 1 and 2 are addressed using idealized simulations in Chapter 4, while question 3 is addressed using a special collection of RO observations in Chapter 5. A majority of the work included in Chapter 4 is published in Gordon and Homeyer (2025). Chapter 5 initially sought to validate TC UTLS temperature changes produced in the simulations, but these high-resolution observations revealed deeper stratospheric impacts than previous literature has reported, and thus altered its direction. The discovery outcome of this work has led to the ongoing pursuit of its publication in *Science*.

Chapter 2

Sensitivities of Cross-Tropopause Transport in Midlatitude Overshooting Convection to the Lower Stratosphere Environment

Motivated by the limited understanding of two-way STE in midlatitude overshooting convection, this chapter analyzes both TST and STT in such storms using a suite of idealized modeling experiments. Specifically, four idealized simulations of tropopause-overshooting supercells are completed using the Bryan Cloud Model 1 (CM1) and vary the thermodynamic and dynamic characteristics of the lower stratosphere environment to represent common regimes found in the midlatitudes. These characteristics include evaluating two lower stratosphere stability environments (single versus double tropopause) and two storm-relative stratospheric wind environments (resulting in storms with and without AACPs). For each simulation, a set of passive tracers is used to quantify transport within the stratosphere and troposphere, as well as the exchange of air between these layers. Spatially integrated time-height analyses of H_2O, the passive tracers, indicators of gravity wave breaking, and vertical motion are used to examine the bulk changes in the UTLS in each simulation, and to guide exploration

of potential mechanisms driving these changes.

2.1 Model Design

For idealized simulations of tropopause-overshooting supercell thunderstorms, release 20.2 of the Cloud Model 1 (CM1) is used (Bryan and Fritsch, 2000). CM1 is a non-linear, non-hydrostatic, three dimensional, time-dependent numerical model that is commonly used for mesoscale storm studies. Here, four unique idealized supercell simulations are designed and carried out by varying the thermodynamic and dynamic environment of the lower stratosphere. The domain for each simulation is a 400 x 333 x 25 km grid box, with 500-m horizontal and 100-m vertical grid spacing. Parameterization choices in the model follow those employed in O'Neill et al. (2021). Convection is initialized with a warm bubble, including a maximum potential temperature perturbation of 1 K. The Morrison double-moment microphysics scheme is employed with hail as the dense rimed ice class (Morrison et al., 2009). The Smagorinsky scheme is used for subgrid-scale turbulence (Stevens et al., 1998). Free-slip winds are applied at the top of the model and a free-slip ocean is applied at the surface. An upper level sponge layer is included within the top 5 km of the grid (20-25 km). No surface model or radiative effects are included.

Each simulation is initialized with a modified version of the conventional Weisman and Klemp (1982) supercell environment. Profiles of initial conditions for these simulations include an equivalent tropospheric environment from the ground to $\sim$9 km (3 km below the tropopause). Thermodynamic environments were varied above the primary tropopause inversion layer (above $\sim$12 km) to include a typical midlatitude single tropopause environment for two simulations, and a double tropopause environment for the other two simulations. The secondary tropopause altitude is 17 km. Stratospheric

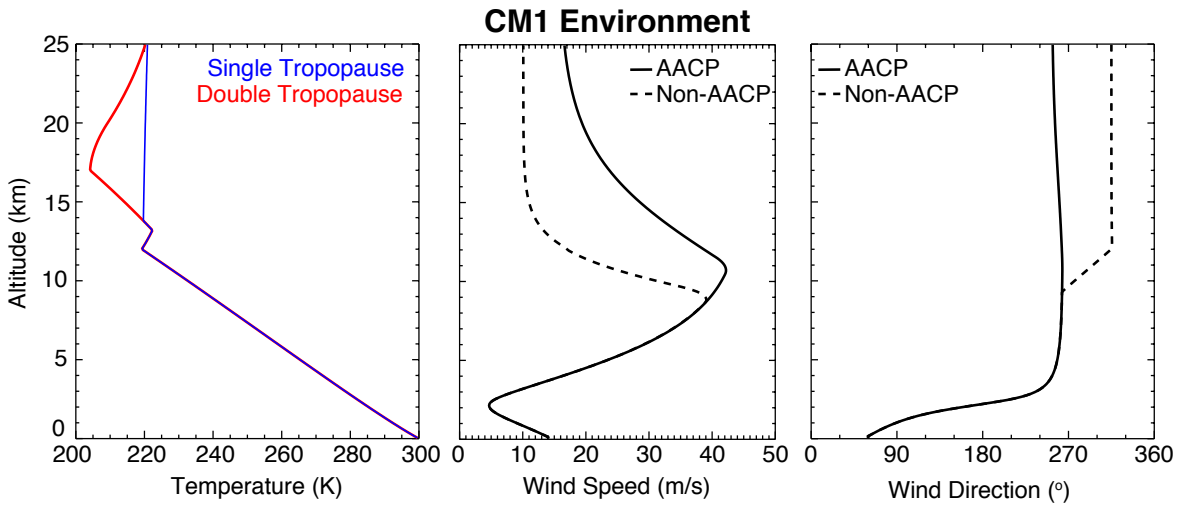


Figure 2.1: Initial conditions (profiles) of idealized simulations including (left) temperature for (blue) single tropopause and (red) double tropopause environments, and (middle) wind speed and (right) wind direction for (solid line) AACP-producing storms and (dashed line) non-AACP storms.

winds were varied to be strong relative to storm motion in two simulations in order to support frequent gravity wave breaking and AACP development, and weak in the remaining two simulations to suppress frequent gravity wave breaking and discourage AACP development (as originally found in observations and tested in Homeyer et al. (2017)). The resulting combination of these thermodynamic and dynamic variations within the lower stratosphere (shown in Fig. 2.1) give four idealized simulations - two single tropopause and two double tropopause simulations, with one AACP and one non-AACP simulation within each tropopause environment.

A set of four custom tropospheric and stratospheric passive tracers are implemented in the CM1 simulations for cross-tropopause transport analysis. The first passive tracer (PT1) is initialized in boundary layer air, set to 100% of the air mass at altitudes less than 1200 m (the boundary layer top in the idealized environment). The second passive tracer (PT2) is initialized as 100% of the air mass at all altitudes at and above the primary tropopause (i.e., 12-25 km). The third passive tracer (PT3) is initialized as

100% of the air mass at all altitudes above a potential temperature of 380 K (the conventional boundary separating the lowermost and overworld stratosphere in the midlatitudes), which occurs at an altitude of 14.2 km. The fourth tracer (PT4) is initialized as 100% of the air mass at altitudes at and above the secondary tropopause altitude (i.e., above 17 km). Following Homeyer et al. (2017), all simulations restrict the initial stratospheric H_2O mass mixing ratio to 5 ppm at all altitudes above the first altitude the mixing ratio is reached near the primary tropopause. Note that this aims to approximate the typical "background" midlatitude stratospheric H_2O concentration of 5 ppmv (e.g., Tilmes et al., 2010), but given the mass-to-volume mixing ratio conversion it is $\sim$8 ppmv in reality. This constant mass mixing ratio approach differs from keeping relative humidity constant, which is common in idealized supercell simulations but leads to spurious formation of cirrus clouds in the stratosphere.

2.2 Results

The evolution of the storm structure based on cloud top altitudes is comparable in all of the simulations (Fig. 2.2), which is expected since the simulations have equivalent tropospheric environments (the primary supporting conditions for supercell development and evolution). The most notable differences are found from contrasting maximum overshooting and AACP depth and anvil shape. The ACCP-producing storms have an elongated anvil due to stronger upper level winds, while the non-AACP storms feature a more circular anvil as a result of weaker UTLS winds (as similarly diagnosed and discussed in Wang et al. (2016)). Evaluating differences in overshoot (cloud tops that extend above the tropopause altitude and are associated with the strong convective updraft) and AACP depth reveals more expansive and deeper overshooting in the double tropopause simulations compared to single tropopuase simulations. Overshooting ma-

terial peaks in altitude near 80 minutes and thereafter plateaus in the AACP-producing storm simulations. This occurs near 60 minutes in the non-AACP storm simulations. For both AACP-producing and non-AACP storms, overshoots reach ∼0.5 km higher in altitude in the double tropopause environment. AACPs reach up to ∼1 km higher in altitude and cover a broader area in the double tropopause environment. AACPs reach heights of 17-18 km with overshoots reaching 15-16 km, indicating that the height of an AACP is not limited by its parent overshoot.

The near-surface simulated radar reflectivity of both AACP-producing and non-AACP storm simulations demonstrates a clear supercellular evolution (Fig. 2.3). Storm structure and evolution are similar for single and double tropopause simulations within AACP-producing and non-AACP storms. There are some slight differences in AACP-producing vs non-AACP storm structure primarily attributed to differences in the UTLS wind profile, and there is a slightly more pronounced hook echo in non-AACP storms. The more pronounced hook echo is expected to be the result of differing UTLS winds, but it is ultimately unknown if the subtle differences are meaningful to or indicative of the differing hazard potential of AACP producing and non-AACP storms. At 60 minutes the storm splits, which eventually leads to a secondary tropopause-overshooting storm by the end of the simulation (i.e., the non-super cellular storm north of the primary storm), consistent with the occurrence of secondary convection in cloud top altitude.

2.2.1 UTLS Hydration and Cross-Tropopause Transport

To evaluate the degree to which UTLS hydration in tropopause-overshooting convection is sensitive to the environment, the change in domain-integrated H_2O mass relative to the total initial domain-integrated H_2O mass at each altitude as a function of time is shown (Fig. 2.4). This and subsequent time-height analysis aggregates mass within

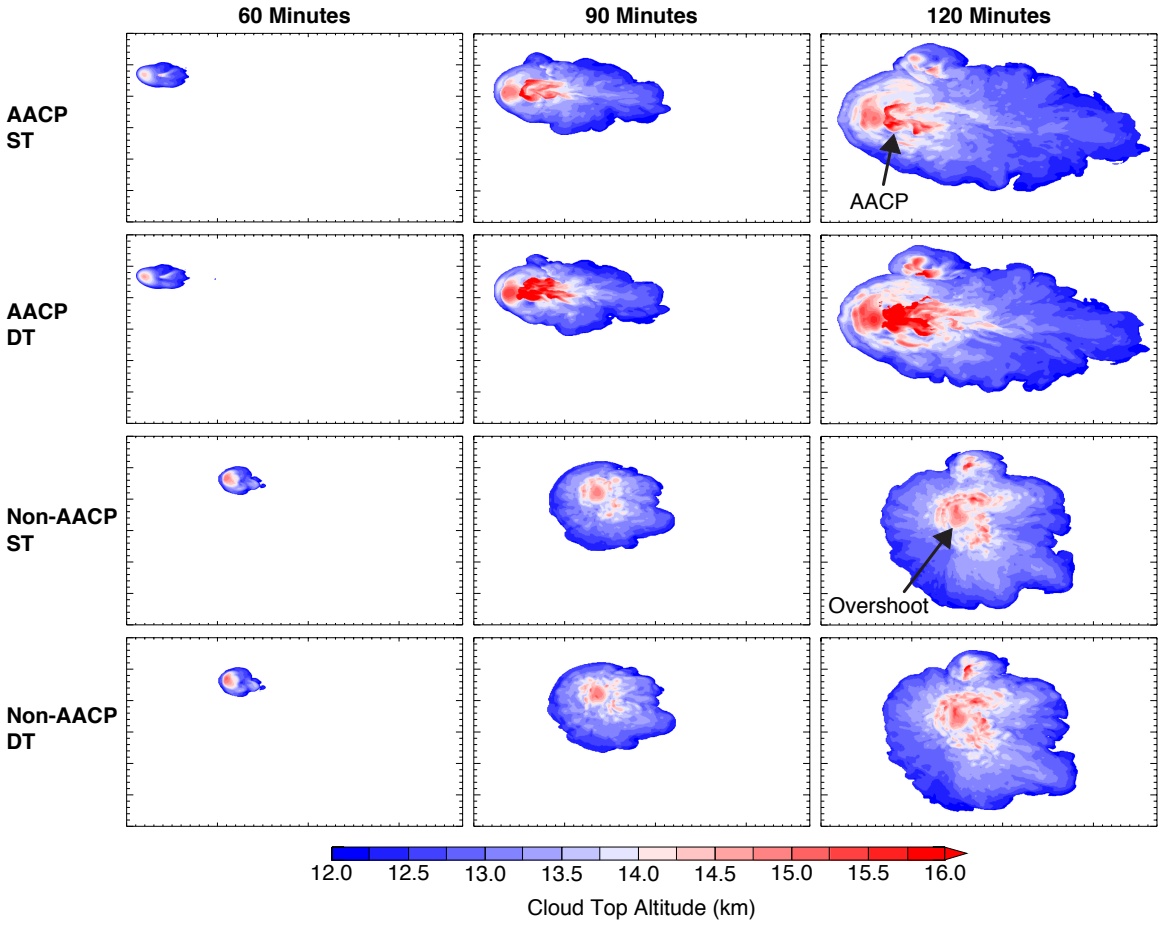


Figure 2.2: Evolution of cloud top altitudes (the maximum altitude that the sum of ice and cloud mixing ratios exceeds 1×10^{-6} kg kg^{-1}) at 60, 90, and 120 minutes for (top to bottom): AACP-producing storm simulations with a single tropopause, AACP-producing with a double tropopause, non-AACP with a single tropopause, and non-AACP with a double tropopause. The domain size for each panel is 185 km by 150 km.

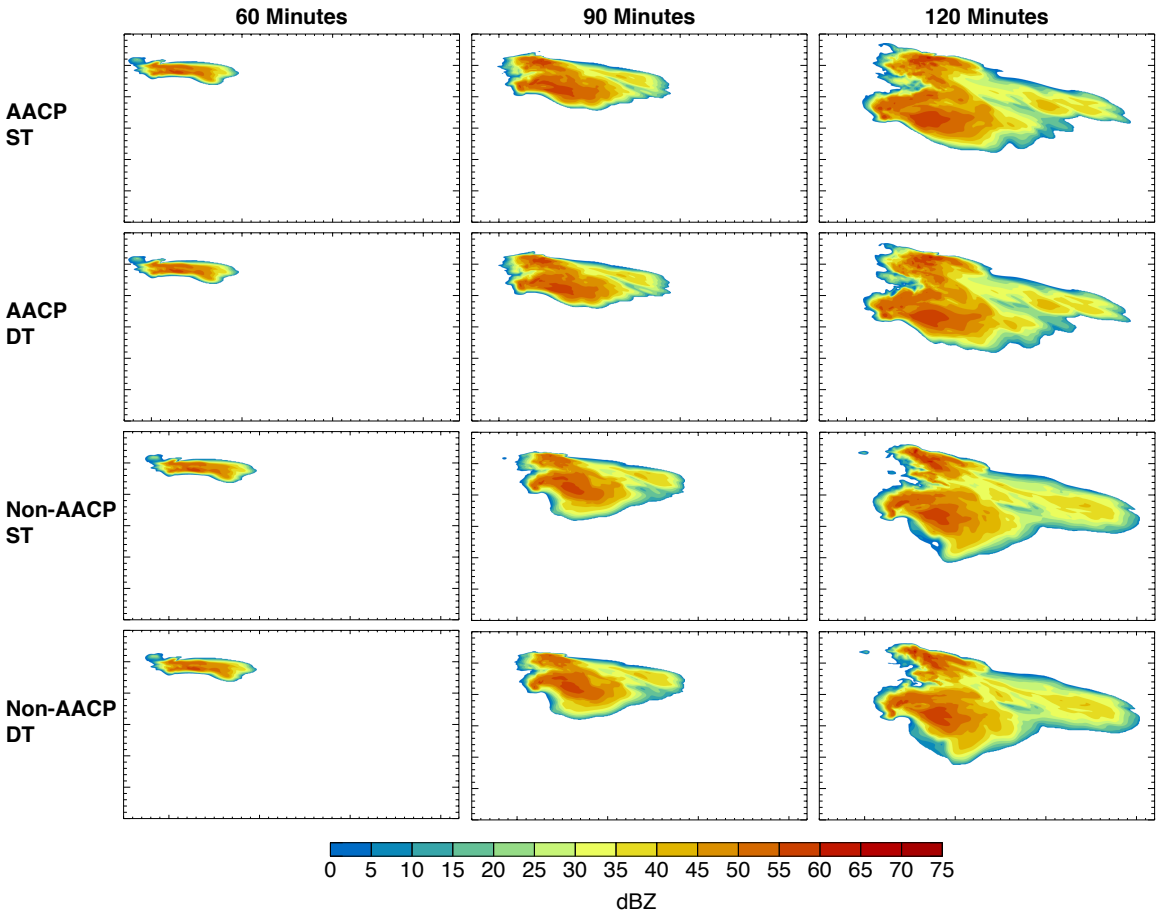


Figure 2.3: As in Fig. 2.2, but for near-surface simulated radar reflectivity.

a specified storm-centered subdomain with an area of 28,000 km^2, which fully encompasses each simulated storm at all times. The analysis focuses on the first 120 minutes of each simulation as secondary convection becomes more prominent beyond that time, making it challenging to distinguish transport from the primary overshoots and AACPs versus the secondary convection. All four idealized simulations result in enhanced H_2O in the UTLS from both air mass transport and ice injection and sublimation. Stratospheric hydration is greatest and extends to higher altitudes in the AACP-producing storms, with enhancements up to 16 km (∼1.5 km higher than that in non-AACP storms). H_2O enhancements also extend 0.25-0.5 km higher within double tropopause environments. H_2O enhancement in the UTLS begins shortly after the time of initial overshooting, is centered near an altitude of 12.5 km for all simulations, and gradually encompasses a deeper tropopause-relative layer over time. By 120 minutes (after more than an hour of continuous overshooting), the H_2O mass increases by about 50% of the original domain air mass over altitudes from 11-14 km for both AACP-producing and non-AACP storm simulations, and by more than 100% in the 1-2 km layer immediately above the tropopause (i.e., more than a doubling of lower stratospheric H_2O over the domain of the storm). The mass increase and depth of elevated H_2O above the tropopause is more substantial in AACP-producing storms, while the below-tropopause H_2O mass increases slightly more in non-AACP storms. To provide clear quantitative assessment of H_2O mass change in these simulations, domain-integrated mass profiles taken at 120 minutes (Fig. 2.8a) are included, which further reveal the aforementioned H_2O mass increases.

Boundary layer air often contains the greatest concentrations of pollutants in the troposphere as it is adjacent to ground sources and convection is uniquely capable of transporting boundary layer air to the UTLS in a short time period. Therefore, assessing the vertical transport of boundary layer air in each simulation is of high

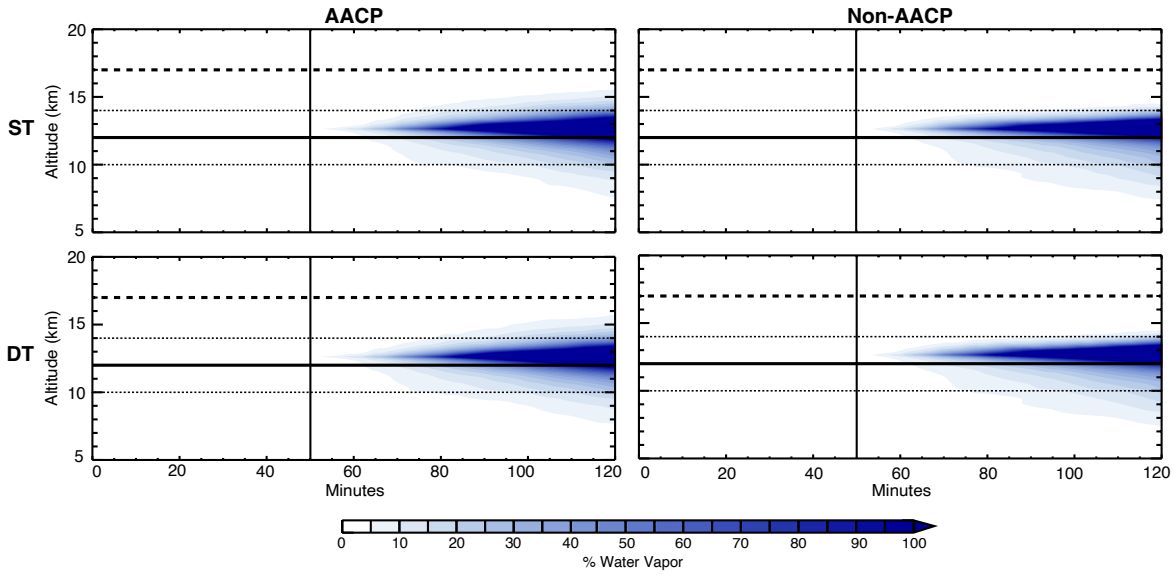


Figure 2.4: Time-height curtains of the domain-integrated mass change in H_2O relative to the initial H_2O mass at each altitude for (left) AACP-producing storms, (right) non-AACP storms, (top) single tropopause environments, and (bottom) double tropopause environments. Vertical lines at a simulation time of 50 minutes indicate the first time of overshooting (that when the cloud top height first exceeds the primary tropopause altitude of 12 km). Thick solid and long-dashed horizontal lines represent the initial primary and secondary tropopause altitudes, respectively, while additional dotted lines at 10 km and 14.2 km (380 K) are for visual reference only.

importance. Thus, similar to the time-height diagnosis of H_2O mass change in the previous paragraph, the same for the passive boundary layer tracer is examined here (Fig. 2.5; relative to the initial domain-integrated dry air mass as a function of altitude within the analysis subdomain). Boundary layer air reaches altitudes above 14 km in all simulations, lower than that found for H_2O, which reaches ∼1-2 km higher in altitude than the transported boundary layer air. Boundary layer transport to the UTLS in all simulations increases shortly after the time of initial overshooting. There are two distinct layers of enhanced delivery of boundary layer air centered at ∼10 and ∼12.5 km that emerge after 60 minutes. The increase near 10 km is more pronounced in the non-AACP storms, while the increase found near 12.5 km is more pronounced for the AACP-producing storms. At 120 minutes, both AACP-producing and non-AACP storms result in a >5% increase of PT1 mass (again, relative to the total initial dry air mass) near 14 km. Single and double tropopause environments within AACP-producing or non-AACP storms show slight differences, with boundary layer air reaching ∼0.25 km higher in a double tropopause environment (especially for the AACP-producing storms). Profiles of boundary layer air mass at 120 minutes (Fig. 2.8b) again provide more quantitative understanding of the aforementioned differences and demonstrate that very little boundary layer air reaches altitudes above 15 km (i.e., well into the overworld).

To estimate the total transport of stratospheric air to altitudes below the initial tropopause level, time-height diagnosis of PT2 are included here (Fig. 2.6). Evaluating the change of PT2 mass throughout time reveals there is more downward transport of stratospheric air in the non-AACP storms. Substantial downward transport of stratospheric air begins near the time of initial overshooting for both AACP-producing and non-AACP storms, but the amount of air mass change is far lower than that for upward transport of boundary layer air largely because of the exponential decrease in

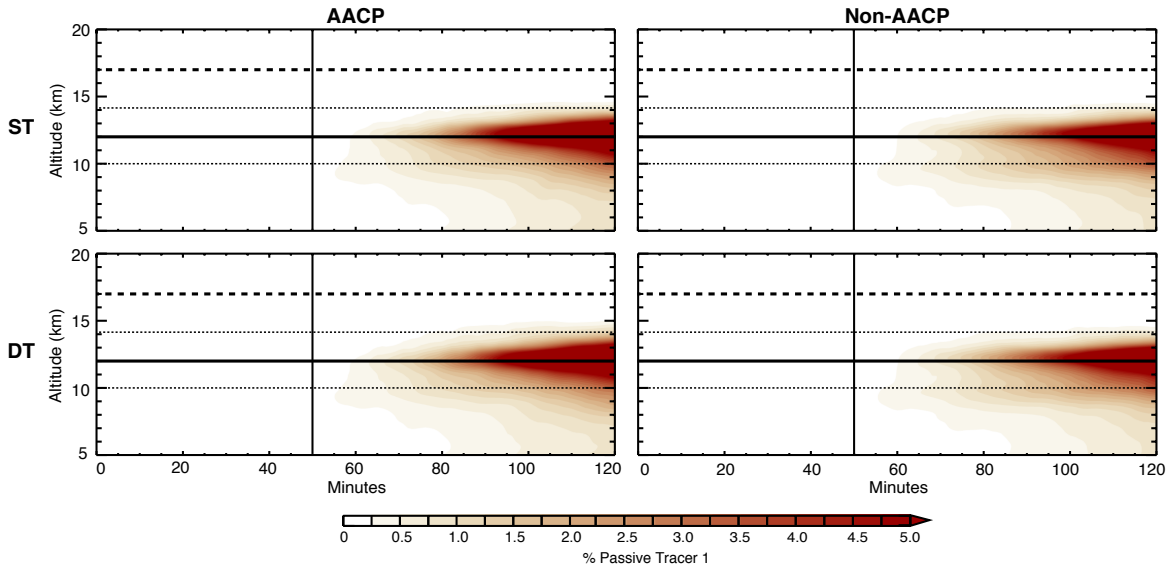


Figure 2.5: As in Fig. 4, but for passive tracer 1 (PT1; boundary layer air) mass change relative to the initial domain-integrated dry air mass.

dry air mass with height (and thus, more difficult task of substantial mass change from downward transport). However, there is a sharper increase in downward transport that extends over a deeper layer in non-AACP storms with PT2 mass increasing to $\geq$1% of the initial dry air mass at altitudes as low as 11 km by 120 minutes. AACP-producing storms feature a more gradual increase of downward transport confined mostly to altitudes above 11 km. At 120 minutes, PT2 is substantially transported down to 11.5 km (500 m below the initial tropopause altitude) with a $\geq$5% increase in mass for both AACP-producing and non-AACP storms. Mass profiles of PT2, taken at 120 minutes (Fig. 2.8c), further demonstrate that non-AACP storms have more downward transport of stratospheric air mass below 11 km. There are no discernible differences in simulated PT2 mass transport between double and single tropopause environments; this is likely attributed to the fact that the tropospheric thermodynamic environments are equivalent.

Since overworld air contains higher concentrations of inorganic chlorine which can become activated in sufficiently cold environments by enhanced H_2O delivered by con-

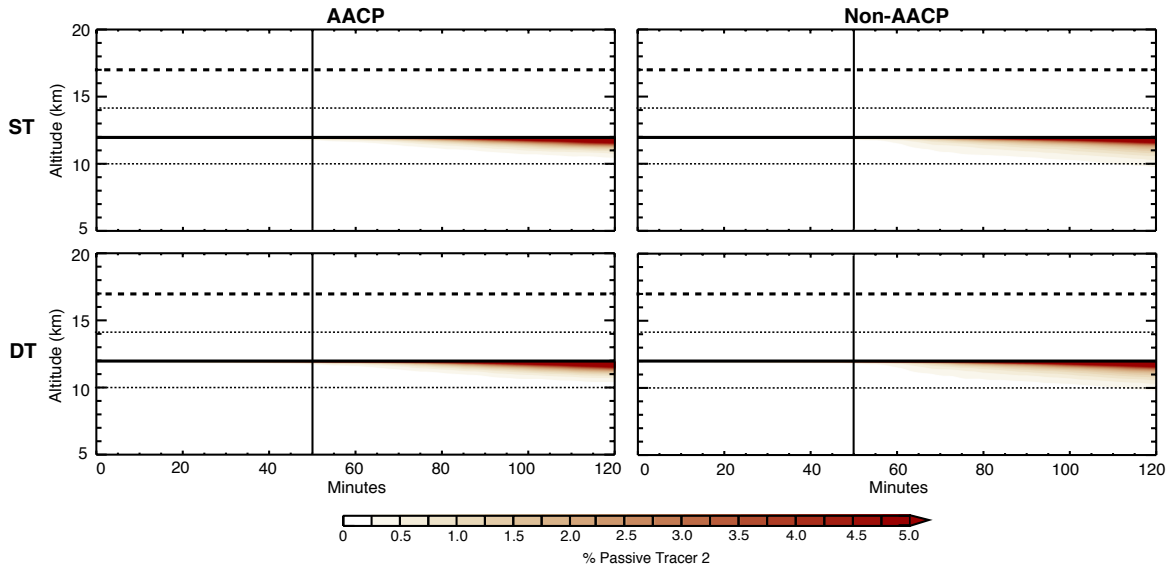


Figure 2.6: As in Fig. 2.5, but for passive tracer 2 (PT2; stratospheric air).

vection to destroy O_3 (Anderson et al., 2012, 2017), it is important to assess the vertical transport of overworld air in the UTLS in these simulations. PT3 is used to represent the downward transport of overworld stratospheric air (that at an initial potential temperature $\geq$ 380 K), which is examined using the same time-height diagnosis here (Fig. 2.7). Greater downward transport of overworld air to the lowermost stratosphere is found in AACP-producing storms, but greater cross-tropopause transport (below 12 km) of overworld air is found in non-AACP storms. Increases of PT3 below the altitude where potential temperature initially exceeds 380 K ($\sim$14 km) begin shortly after the time of initial overshooting for AACP-producing storms, and approximately 15 minutes later for non-AACP storms. AACP-producing storms result in a gradual increase in the depth of downward transport of overworld air, which is mostly confined to altitudes above 12 km and reaches no lower than 11 km by 120 minutes. AACP-producing storms also contain a $\geq$2% increase of PT3 mass at altitudes down to $\sim$13 km, and a $\geq$1% increase down to $\sim$12 km. Non-AACP storms result in a substantially different character of downward transport of overworld air, with a local maximum of $\sim$1% increase

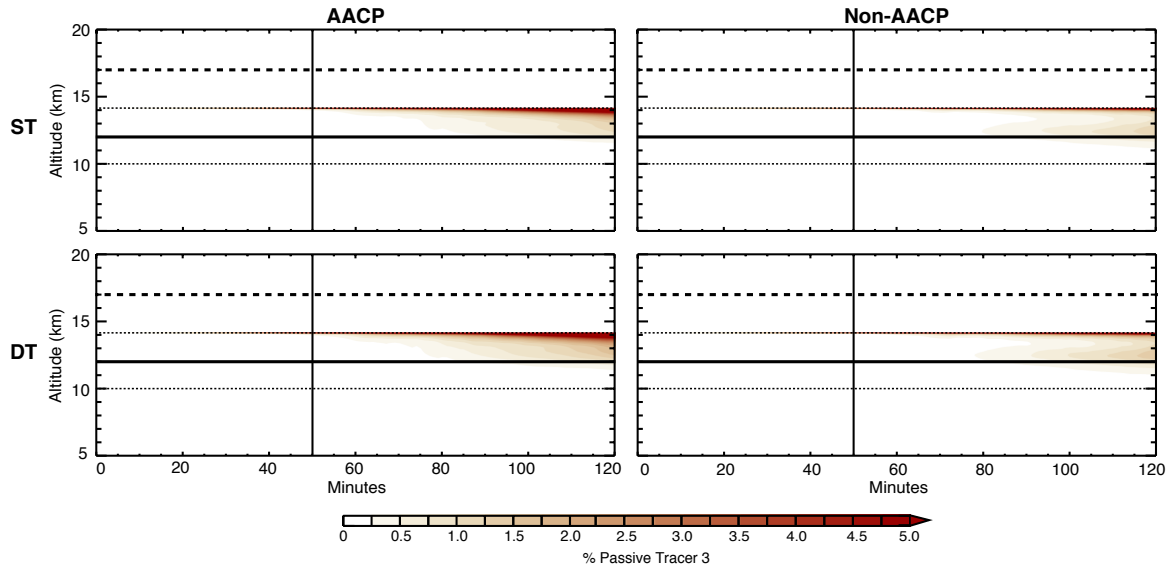


Figure 2.7: As in Fig 2.5, but for passive tracer 3 (PT3; stratospheric overworld air).

between 12 and 13 km. This may indicate a narrow transport pathway for overworld air with little mixing between 13 and 14 km in non-AACP storms. Lastly, double tropopause environments in both AACP-producing and non-AACP storm simulations result in more downward transport of overworld air to the lowermost stratosphere than their respective single tropopause environments, and these differences are more prominent in AACP-producing storms. Specifically, in AACP-producing storms, a double tropopause results in ∼0.5% more downward transport of overworld air between 12 and 13 km, and in non-AACP storms results in an increase of ∼0.25% more downward transport than that in single tropopause environments. Profiles of PT3 mass at 120 minutes (Fig. 2.8d) further emphasize these differences in downward transport of overworld air between simulations, which are more prominent than most of the other transport differences.

PT4 was used to evaluate any downward transport of air from 17 km or higher (above the second tropopause level in the double tropopause environment). Changes in PT4 mass transport over time were minimal at all altitudes and, as such, are not

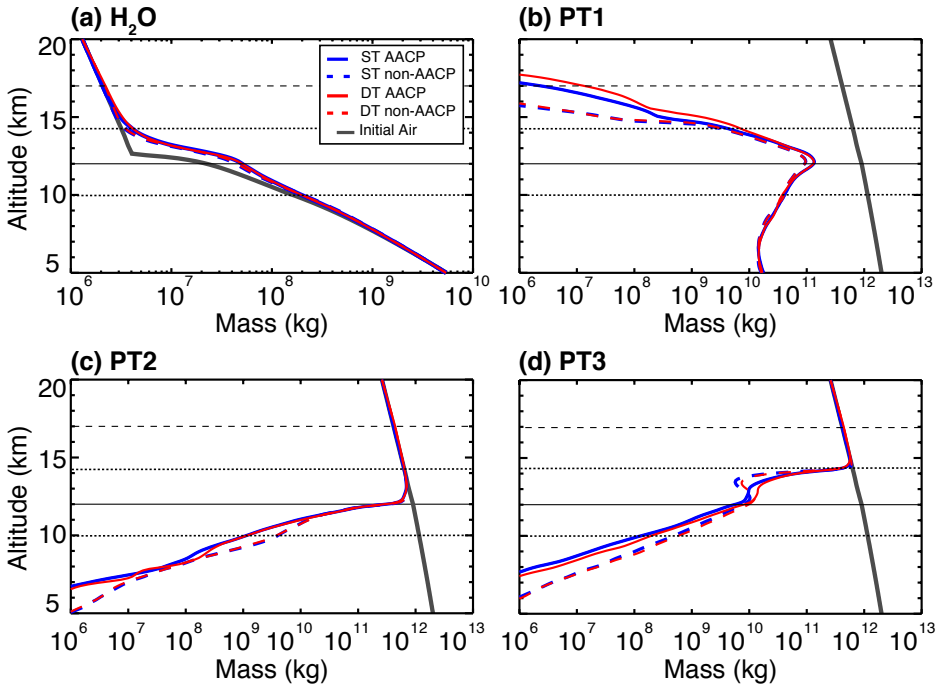


Figure 2.8: Domain-integrated mass profiles at the final simulation time of 120 minutes of a) water vapor (H_2O), b) passive tracer 1 (PT1; boundary layer air), c) passive tracer 2 (PT2; stratospheric air), and d) passive tracer 3 (PT3; stratospheric overworld air). Initial domain-integrated mass profiles of H_2O and dry air are given in panels a and b-d, respectively, for reference.

shown.

2.2.2 Potential Mechanisms Impacting Transport

Examining UTLS hydration and cross-tropopause transport for AACP-producing and non-AACP storms within single and double tropopause environments revealed several important differences in stratospheric hydration, cross-tropopause transport, and downward transport of overworld air to the lowermost stratosphere. To identify potential mechanisms responsible for these bulk differences, vertical cross-sections through each storm were taken at several times throughout each simulated storm's evolution. Here, the analysis of potential mechanisms is restricted to show to single tropopause simulations only, since differences in transport behavior were found to be dominated

by AACP versus non-AACP simulations and no additional insights were gained for the varying tropopause environments.

Since AACP development is associated with strong storm-relative stratospheric winds that support frequent gravity wave breaking, this chapter examines wave breaking behavior via the vertical gradient of potential temperature (Fig. 2.9). It is expected that the AACP-producing storm would have a deep layer of gravity wave breaking above the tropopause (evidenced by frequently negative – i.e., unstable – potential temperature gradients), and the non-AACP storm would have little stratospheric wave breaking. There are indeed differences in the minimum potential temperature gradient found in AACP-producing and non-AACP storm simulations, with a greater reduction in stability present in AACP-producing storms at altitudes above 14 km. In particular, after the time of initial overshooting, unstable layers are pervasive in the 14-17 km altitude layer in AACP-producing storms, signifying frequent gravity wave breaking (and irreversible mixing), which is not found in this layer in non-AACP storms (see r.h.s. of Fig. 2.9). Thus, it is no surprise that maps and vertical cross-sections reveal the AACP is present from 14-17 km (c.f. Figs. 2.2 & 2.11) in the simulations, coinciding with the layer of unstable air.

While the AACPs are well-demonstrated to be driven by sustained gravity wave breaking near the overshooting top in such storms (for which the behavior is consistent with a hydraulic jump), examining time-height curtains of the minimum and maximum vertical velocity (Fig. 2.10) suggests that overshooting in the non-AACP storms behaves more strongly as a mechanical oscillator. An overshooting cloud and air mass is near its maximum vertical velocity when it reaches its level of neutral buoyancy near the tropopause, so it overshoots the tropopause and decelerates as it becomes colder than the environment and negatively buoyant. When vertical velocity reaches zero, the overshooting cloud and air mass is much colder than its environment and begins

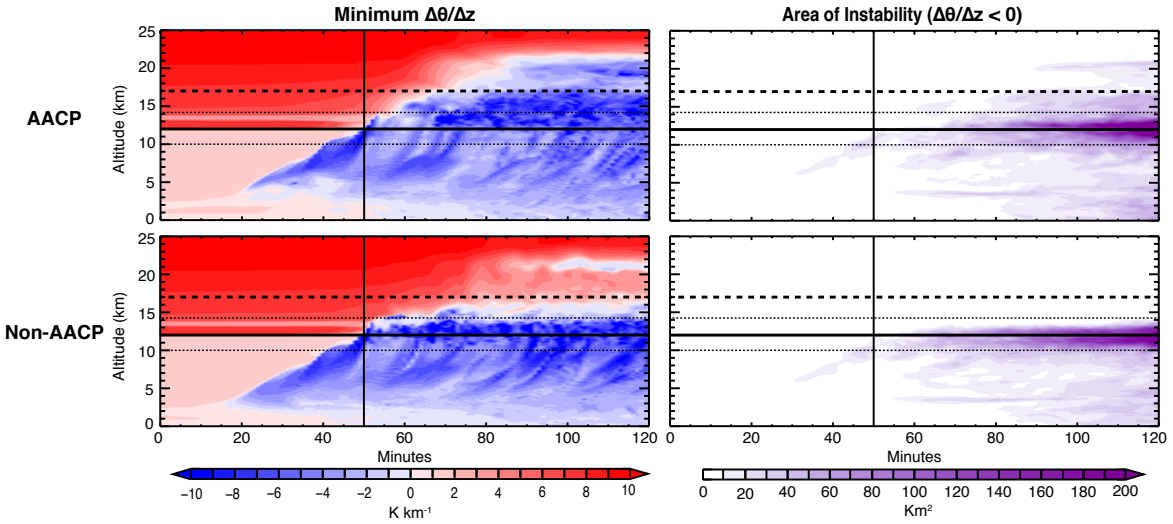


Figure 2.9: Time-height curtains of (left) domain-minimum potential temperature gradient and (right) areal extent of instability (potential temperature gradient less than 0 K km^{-1}) for (top) AACP-producing and (bottom) non-AACP storms.

to accelerate downward until it once again crosses its level of neutral buoyancy and undershoots the tropopause, once again becoming warmer than the environment and positively buoyant. This process repeats itself until vertical momentum is destroyed by mixing and additional processes, demonstrating an oscillatory behavior. The overshooting cloud and air mass thus have sinusoidal oscillations about the tropopause, with amplitudes decreasing as distance from the overshoot increases. This overshoot-driven mechanical oscillation has been a focus of prior work and is a well-recognized source of convective gravity waves (Fovell et al., 1992; Lane et al., 2001).

The present analysis (Fig. 2.10) demonstrates that non-AACP storms have a stronger and longer-lived mechanical oscillation than AACP-producing storms, in part due to differences in gravity wave breaking. Namely, AACP-producing storms have more gravity wave breaking, which destroys vertical momentum as it mixes overshoot material into the stratosphere, thereby preventing subsequent oscillatory behavior of the overshoot. In particular, while there is comparably strong upward motion present in both AACP-producing and non-AACP simulations, there is substantially stronger

downward motion in non-AACP cases spanning altitudes ±2–3 km from the initial tropopause. The time-height curtains also reveal a periodic occurrence of vertical velocity extrema in the lower stratosphere (12-14 km altitude) that represent successive overshooting thermals (based on the 1-min output available for analysis). In AACP-producing storms, these extrema occur every 5 minutes and begin at the time of initial overshooting, becoming less apparent at ∼80 minutes (perhaps due to interaction with the hydraulic jump that becomes established near this time, as evidenced by the layer of enhanced upward motion from 14 to 17 km that is not found in the non-plume simulations). Upward vertical velocity maxima are apparently more frequent in non-AACP storms, occurring every ∼3.5 minutes. As in the AACP-producing storms, these extrema begin at the time of initial overshooting and continue for the remainder of the simulation. Downward vertical velocity extrema for non-AACP storms are stronger, more frequent, and deeper than those in AACP-producing storms. Consistent with a mechanical oscillation of overshoot air, downward vertical velocity extrema begin shortly after upward vertical velocity extrema and remain out of phase throughout the simulation. The depth of downward vertical velocity extrema is typically ∼2 km deeper in non-AACP storms.

Vertical cross-sections of H_2O and PT1-PT3 are also analyzed to help identify mechanisms responsible for bulk transport differences found in Section 3.1. While cross-sections were taken at 1-min intervals for simulation times spanning 60 to 120 minutes, a single time is shown in Figure 2.11 to illustrate key sustained features identified from this analysis. Namely, vertical motion patterns near and surrounding the storm updraft support the inference that overshooting in each storm behaves as a mechanical oscillator, as seen by the couplet of upward and downward motion occurring downstream of the overshoot in each case. This oscillation is found to be coincident with pronounced cross-tropopause transport of air in the passive tracer fields

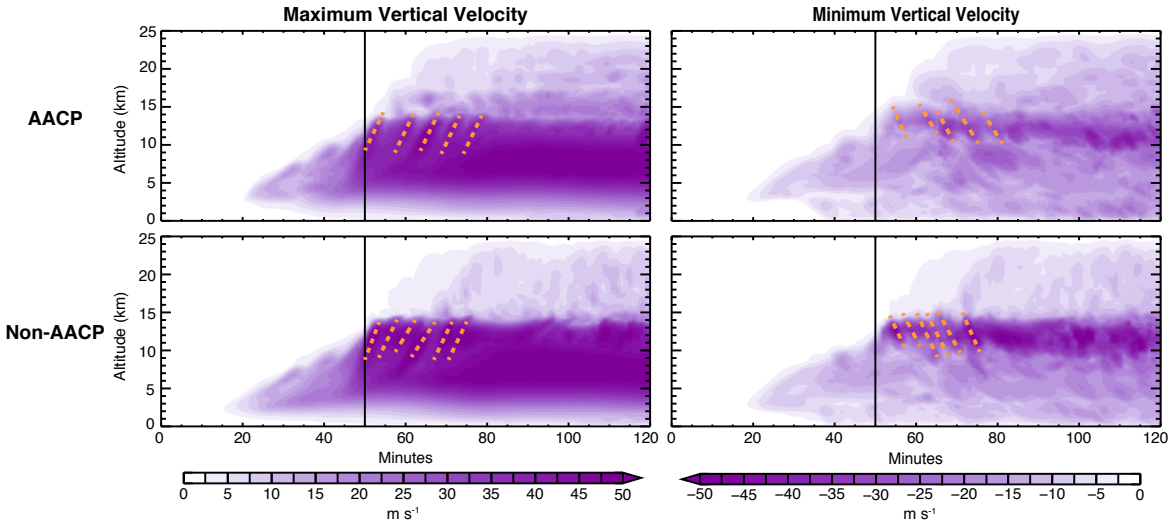


Figure 2.10: As in Fig. 2.9, but for the (left) maximum and (right) minimum vertical velocity. Dashed orange lines coincide with subjectively identified ascending (descending) maxima (minima) in vertical velocity with time.

throughout the simulation time. The oscillation is slightly stronger and ∼1 km deeper in the non-AACP producing storms, which is likely why there is more downward cross-tropopause transport in these storms. Additionally, the oscillation is more symmetric in the non-AACP storms, which leads to both upstream and downstream impacts, but the downstream oscillation remains stronger and deeper nonetheless (Fig. 2.12). The AACP-producing storm has a comparably strong oscillation initially, which becomes less deep after 80 minutes due to its coupling with the apparent hydraulic jump near 15 km altitude that persists throughout the remainder of each AACP storm simulation (as diagnosed in Fig. 2.10). Likening this feature to a hydraulic jump, as argued recently in much higher-resolution idealized simulations by O'Neill et al. (2021), is motivated by its stability and persistence in our simulations after 80 minutes, rather than a simpler alternative such as periodic gravity wave breaking.

Cross-sections (Fig. 2.11) of H_2O demonstrate that H_2O enhancements at altitudes above 15 km in the AACP-producing storm are associated with the AACP. Little to

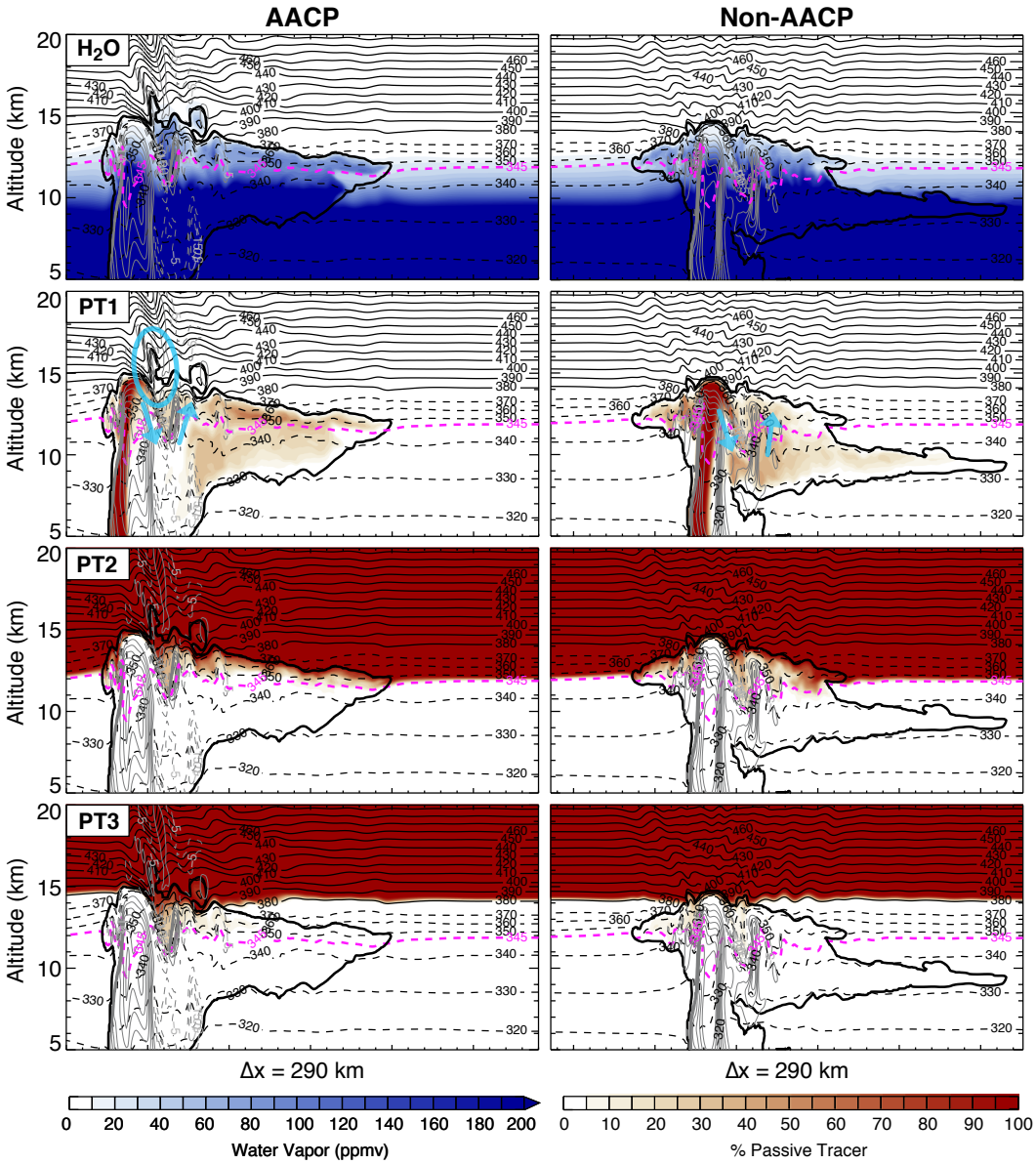


Figure 2.11: Vertical cross-sections at a simulation time of 90 minutes for (left) single tropopause AACP-producing and (right) single tropopause non-AACP storms. From top to bottom: water vapor (H_2O; in ppmv), passive tracer 1 (PT1; boundary layer air), passive tracer 2 (PT2; stratospheric air), and passive tracer 3 (PT3; stratospheric overworld air). Vertical velocity contours are shown in gray in each panel, with intervals of 5 m/s (upward motion is solid and downward is dashed). Black contours in each panel represent potential temperature at 10-K intervals (with solid contours for 380 K and above, and dashed below). The potential temperature of the environmental tropopause (345 K) is shown in magenta in each panel. The blue arrows and blue ellipse atop the PT1 sections identify the mechanical oscillation and hydraulic jump features, respectively.

no boundary layer air (PT1) reaches such high altitudes within the AACP, but the cross sections reveal that more of this air reaches altitudes above 12 km in the AACP storm (as found in the time-height analysis). While these cross sections show the boundary layer air concentrations are highest in the updraft, such is true throughout time in the simulations, implying that the increases of PT1 identified in the time-height analysis are primarily driven by differences outside of the updraft, where air has been irreversibly mixed into the UTLS. Additionally, the enhanced layers of boundary layer air at ∼10 and ∼12 km are consistent with those identified in Figure 2.5. Based on its evolution over time (not shown), the 10 km layer is likely a preferred anvil level detrainment layer early in the storm's evolution, which deepens faster in the AACP simulation and is driven (in part) by the frequent gravity wave breaking that occurs. Cross-sections of PT2 support the finding that there is more STT in non-AACP storms. This is apparently facilitated by the stronger and deeper downward motion within the mechanical oscillation, and the increased area of the oscillation (i.e., occurring both upstream and downstream of the overshoot) in the non-AACP storm (Fig. 2.12). Finally, cross-sections of PT3 reveal that greater downward transport of overworld air to the lowermost stratosphere in AACP-producing storms occurs within the region of the coupled hydraulic jump and mechanical oscillation, but more cross-tropopause transport (to altitudes below 12 km) in non-AACP producing storms appears to be the result of the deeper and stronger mechanical oscillation. Moreover, while cross-sections reveal that the mechanical oscillation feature is an important mechanism for facilitating STT, there is no evidence of anvil wrapping in these simulations.

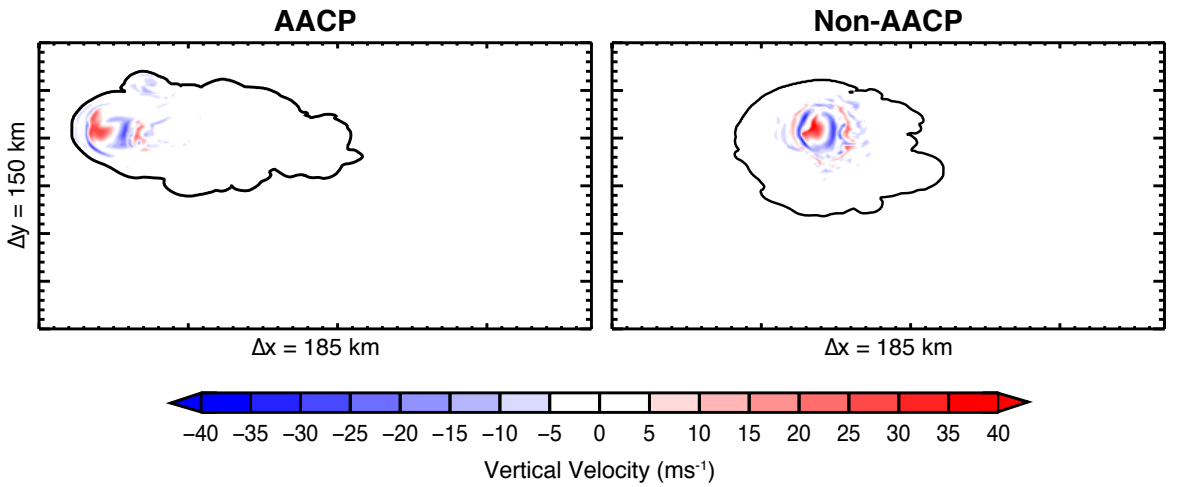


Figure 2.12: Vertical velocity at 12 km for (left) AACP-producing and (right) non-AACP storms at 90 minutes. The black contour outlines the cloud boundary (where the sum of ice and cloud mixing ratios is greater than 1.0E-6 kg/kg).

2.3 Summary

This chapter used four idealized simulations of tropopause-overshooting supercells to examine how varying thermodynamic and dynamic characteristics of the lower stratosphere environment impacts overshooting, the development of AACPs, and cross-tropopause transport. These varying characteristics included two common lower stratosphere stability environments (single versus double tropopause) and two storm-relative stratospheric wind environments (resulting in storms with and without AACPs). In each simulation, spatially integrated time-height analyses of H_2O, passive tracers, indicators of gravity wave breaking, and vertical velocity were used to examine changes within the UTLS and the factors responsible. In agreement with previous studies, AACP-producing storms were found to have a greater impact on the stratospheric overworld than non-AACP storms (O'Neill et al., 2021; Homeyer et al., 2017). The lowermost stratosphere was more hydrated by impacts from AACP-producing storms than non-AACP storms, which differs from that found in O'Neill et al. (2021) and

Homeyer et al. (2017). The difference in hydration of the lowermost stratosphere could be driven by the differences in environmental wind profile used here, for which the wind change with altitude is smoother than that used in previous studies. It was found that using a wind profile with an abrupt decrease of $\sim$30 m s^{-1} near the tropopause for non-AACP storms (like the 20 m s^{-1} decrease employed in O'Neill et al. (2021) and Homeyer et al. (2017)) led to a domain-wide Kelvin-Hemholtz instability at the tropopause which enhanced cross-tropopause mixing (not shown). Thus, these results are likely more indicative of cross tropopause-transport in real-world storms since the shape of the UTLS wind profile is more consistent with observed storm environments.

It was additionally found that more expansive AACPs, more TST, and deeper overshoots occurred in double tropopause environments. Finally, while impacts to the lower stratosphere were relatively limited in non-AACP storms, greater STT occurred in those storm simulations. However, greater downward transport of overworld air to the lowermost stratosphere was found in the AACP-producing storm simulations, which was further enhanced in a double tropopause environment (by 0.5%). Downward transport led to less substantial changes overall, likely reflecting constraints of the relative mass differential for such transport (i.e., it is more difficult to have substantial composition change from STT since a unit volume of lower stratosphere air has far less mass than that in the upper troposphere).

Based on these differences in AACP-producing and non-AACP storms, this chapter analyzed vertical cross sections for each storm throughout its evolution to identify potential mechanisms responsible for these differences. One mechanism involved in STE in all four simulations is the mechanical oscillation driven by the overshoot. The oscillation was found to be deeper, stronger, and more symmetric in the non-AACP producing storms, which is likely why there is more downward cross-tropopause transport in these simulations. The mechanical oscillation in AACP-producing storms becomes

coupled with the apparent hydraulic jump that is critical to AACP formation, which appears to be responsible for the enhanced downward transport of overworld air to the lowermost stratosphere found in those storms.

Chapter 3

Airborne observations of upper troposphere and lower stratosphere composition change in active convection producing above-anvil cirrus plumes

The recently completed NASA Dynamics and Chemistry of the Summer Stratosphere (DCOTSS) field campaign provides unprecedented observations of tropopause-overshooting convection that have exceeded all prior records of stratospheric depth (Homeyer et al., 2023). The primary goal of the DCOTSS mission was to improve understanding of the dynamical and chemical processes that influence the composition of the extratropical summertime stratosphere, with several core science questions including: (a) How much tropospheric air and water is irreversibly injected into the stratosphere by convection?, and (b) What dynamical mechanisms lead to the irreversible injection of material into the stratosphere by convective storms? DCOTSS completed at least 18 flights sampling material from overshooting convection, but it is currently uncertain how many of these flights sampled material from AACP-producing storms (versus non-AACP

storms). Multiple active convection flights were completed, but only one flight (on 31 May 2022) specifically targeted and repeatedly sampled an actively-generated AACP as it was deemed safe to do so. In this chapter, in situ airborne observations of this event are presented. The measurements obtained throughout this flight by the versatile DCOTSS instrument payload provide unique insight into UTLS composition changes associated with the storm. This analysis in this chapter utilizes these observations to assess how the composition of the UTLS is altered by an AACP-producing storm and compare these observations with results from recent modeling studies.

3.1 Data and Methods

3.1.1 DCOTSS Overview

The DCOTSS field campaign used the National Aeronautics and Space Administration (NASA) ER-2 high-altitude research aircraft to investigate the impact of intense convection on the summertime stratosphere over North America from June to August 2021 and May to July 2022. The focus was on sampling air from active, recent, and aged overshooting events over the United States, but science flights also sampled pyrocumulonimbus smoke, outflow from storms occurring over the Sierra Madre Occidental in Mexico, and surveyed the large-scale structure of the North American Monsoon Anticyclone. DCOTSS was based primarily in Salina, Kansas (38.84°N, 97.61°W) and the ER-2 flew 29 science flights with research-quality data (depending on the instrument) during the campaign: 14 in 2021 and 15 in 2022. Active convection was sampled during three flights (31 May 2022, 08 June 2022, and 24 June 2022), with the most extensive sampling of active convection during the 31 May 2022 flight. The 31 May 2022 flight sampled multiple convective enhancements (both inside and outside of cloud material)

throughout the flight, featuring a bisect and profile of an AACP. The DCOTSS instrument payload consists of twelve instruments and was designed to provide myriad in situ measurements of trace species and meteorological parameters in the UTLS necessary to evaluate transport, mixing, and the net chemical impact of summertime convection on the UTLS.

3.1.2 DCOTSS Observations

In this analysis the multiple select trace constituents selected are those that are useful for diagnosing convective transport within the UTLS. These include H_2O, O_3, CO, methane (CH_4), total water (vapor + ice), and several additional trace species with anthropogenic sources at the surface. Harvard Water Vapor (HWV) measures ambient H_2O mixing ratios at 1 Hz. The HWV instrument is composed of the Harvard Lyman-α photo-fragment fluorescence instrument (LyA) and the Harvard Herriot Hygrometer (HHH), a tunable diode laser direct absorption instrument. Only the HHH observations are used in this chapter. The measurements have an accuracy of 5-10% and a precision better than 0.1 ppmv (Sargent et al., 2013). The Rapid OZone Experiment (ROZE) is a cavity-enhanced ultraviolet absorption instrument that measures in situ O_3 by direct absorption, obtaining measurements at 1 Hz with a precision of 1 ppbv in the stratosphere and an accuracy of 6% (Hannun et al., 2020). The Harvard University Picarro Cavity Ringdown Spectrometer (HUPCRS) is a modified G-2401m Picarro gas analyzer (Crosson, 2008) that measures CO_2, CH_4, and CO every $\sim$2.2 secs; CH_4 data are reported at 1 Hz with 0.2 ppbv uncertainty and CO data are reported at 0.1 Hz with 3.2 ppbv uncertainty. The Water Isotopologues – Integrated Cavity-Output Spectrometer (WI-ICOS) measures total water (vapor + ice) and its major isotopologues at 1 Hz. WI-ICOS uses cavity enhanced absorption, and an isokinetic inlet and heaters are used to measure total water, which is the only measurement used in this chapter.

WI-ICOS total water measurements have an accuracy of 0.1 ppmv and an uncertainty of 10% (Sayres et al., 2009).

The Advanced Whole Air Sampler (AWAS) consists of 32 stainless-steel canisters mounted in the center belly pod of the ER-2. The canisters were typically filled on-demand to target samples from specific features during a research flight. The time for AWAS to collect a sample varies depending on altitude, between 20-200 s (with shorter times at lower altitudes). After each flight, canisters were analyzed using gas chromatography with mass spectrometry, a flame ionization detector, and an electron capture detector to determine the mixing ratio of a variety of tracers. AWAS measures more than 20 constituents with varying lifetimes and provides valuable measurements of short-lived and very short-lived tracers (Flocke et al., 1999; Schauffler et al., 1999). AWAS constituents of interest for the 31 May 2022 flight include ethane, ethyne, and propane. Ethane (C_2H_6) has a tropospheric lifetime of 52 days (Chelpon et al., 2021), and is primarily sourced from crude oil and natural gas production, with additional sources from biomass and fossil fuel burning. Propane (C_3H_8) is also primarily a product of crude oil and natural gas production, with additional sources from biomass and fossil fuel burning, and has a tropospheric lifetime of 9.4 days (Chelpon et al., 2021). Ethyne (C_2H_2) has a tropospheric lifetime of 9.8 days (Chelpon et al., 2021), and is primarily sourced from biomass and biofuel burning, but can also result from crude oil and natural gas production.

Meteorological parameters including temperature, potential temperature, horizontal winds, and vertical winds are examined to gain further insight regarding STE processes throughout the flight. The Meteorological Measurement System (MMS) provides calibrated, high resolution measurements of ambient meteorological parameters, including temperature, pressure, the 3-dimensional wind vector, and turbulent energy dissipation rate (TEDR), at 20 samples per second. The MMS potential temperature

has an accuracy of 0.5-1.5 K, temperature has an accuracy of ±0.3 K, horizontal and vertical winds have a combined accuracy of ±1 m s^{-1}, and the GPS altitudes have an accuracy of 15 m (Scott et al., 1990). For contextual campaign-wide analysis, this chapter leverages feature identifications outlined in Homeyer et al. (2023). Namely, convective versus non-convective observations are based on manual identification of H_2O enhancements above prevailing background conditions within the stratosphere that have been linked to overshooting convection (identified with radar and satellite observations) via trajectory matching.

3.1.3 ERA5 Reanalysis

Version 5 of the European Centre for Medium-range Weather Forecasts (ECMWF) reanalysis, ERA5, is used for tropopause identification within this chapter (Hersbach et al., 2020). The ERA5 used here consists of hourly global assimilations of the atmospheric state on 37 pressure levels and a 0.25° latitude-longitude grid. These ERA5 vertical profiles are linearly interpolated to a regular 200-m grid before the lapse-rate tropopause (LRT) definition (World Meteorological Organization, 1957) is applied, which allows finer localization of the tropopause than that possible on the coarse grid and increased agreement with finer-resolution data. Resulting LRT altitudes are interpolated linearly in time and space to aircraft location as well as radar and satellite grids for analysis. ERA5 LRT altitudes calculated on the native model grid have been demonstrated to have minimal bias with uncertainties ≤250 m (e.g., Hoffmann and Spang, 2022). Although ERA5 output is available on the full 137 model grid, those data yield minor refinement. Specifically, global comparison of our LRT altitudes based on the 37-level pressure grid and the native model grid demonstrate that they commonly agree to within ±500 m (not shown). This minimal refinement led to the decision to use the coarser 37 pressure level data to minimize storage and computa-

tional cost. Moreover, a tropopause altitude uncertainty of ±500 m for global model output such as ERA5 is a long-demonstrated standard and tolerable for the analyses and interpretations presented in this chapter.

3.1.4 Radar Observations

Gridded NEXRAD WSR-88D Radar (GridRad) data version 4.2 is used for high resolution analyses of overshooting convection in the contiguous United States (Homeyer and Bowman, 2022). GridRad merges individual NEXRAD WSR-88D data onto a common three-dimensional grid, and is available at 10-minute intervals for this chapter. The grid has ∼0.02° latitude-longitude (∼2-km) resolution, with a domain spanning 24-50°N latitude and 235-294°E longitude. Altitude spacing of the GridRad data is 0.5-km at altitudes below 7 km above mean sea level (AMSL) and 1-km otherwise up to 22 km AMSL. The sole variable from the GridRad volumes used for analysis in this chapter is the radar reflectivity at horizontal polarization (Z_{H}). Tropopause-overshooting convection is identified as $Z_{\mathrm{H}} = 15$ dBz echo-top altitudes above the ERA5 LRT. Quality control metrics consistent with previous radar climatologies (Solomon et al., 2016; Cooney et al., 2018; Homeyer and Bowman, 2021) are applied, and GridRad echo-top altitudes are unbiased with an uncertainty of 1 km.

3.1.5 Satellite Observations

Imagery from the Geostationary Observing Earth Satellite (GOES) platform over North America is used to enable AACP identification and to complement radar observations for analysis of the 31 May 2022 flight. Here, only GOES-16 (GOES-East) imagery is used at 1-minute intervals over the domain of the flight. Namely, visible (VIS; channel 2 with a central wavelength of ∼0.64 μm) and infrared (IR; channel 13

with a central wavelength of ∼10.3 μm) satellite imagery from the GOES Advanced Baseline Imager (ABI) are used (Schmit et al., 2017). AACPs are commonly identifiable in VIS as an area with relatively smooth texture that casts a shadow on the underlying anvil, especially at times approaching sunset when the solar inclination angle is high. In IR, AACPs representing stratospheric injection of cloud material can be identified by anomalously warm brightness temperatures compared to the storm anvil (Murillo and Homeyer, 2022).

3.2 Results

3.2.1 Storm Characteristics and Flight Overview

The 31 May 2022 flight was designed to target active and ongoing overshooting convection in western Oklahoma. On 31 May 2022, a cluster of storms formed in western Oklahoma and the adjacent northern portion of Texas near 21:00 UTC. Overshooting convection began near 22:00 UTC on 31 May 2022 and dissipated near 6:30 UTC on 1 June 2022, leading to ∼8.5 hours of sustained overshooting within this cluster of storms. Overshoots reached a maximum echo-top height of 19 km at 22:00 UTC, with persistent echo-top heights near 17-18 km for the majority of the storms' lifetimes (including the sampling timespan of the 31 May 2022 flight). Figure 3.1 shows radar reflectivity, echo-top heights, and IR & VIS satellite imagery of the storms for select times, including throughout the sampling time period (00:20 UTC through 02:10 UTC). Material from the overshoot and accompanying AACP in western Oklahoma (indicated by the yellow and cyan circles in Fig. 3.1, respectively) was targeted. This specific cell had sustained overshooting from 22:00 UTC on 31 May until it decayed near 01:00 UTC on 1 June (3 consecutive hours of overshooting), while the AACP

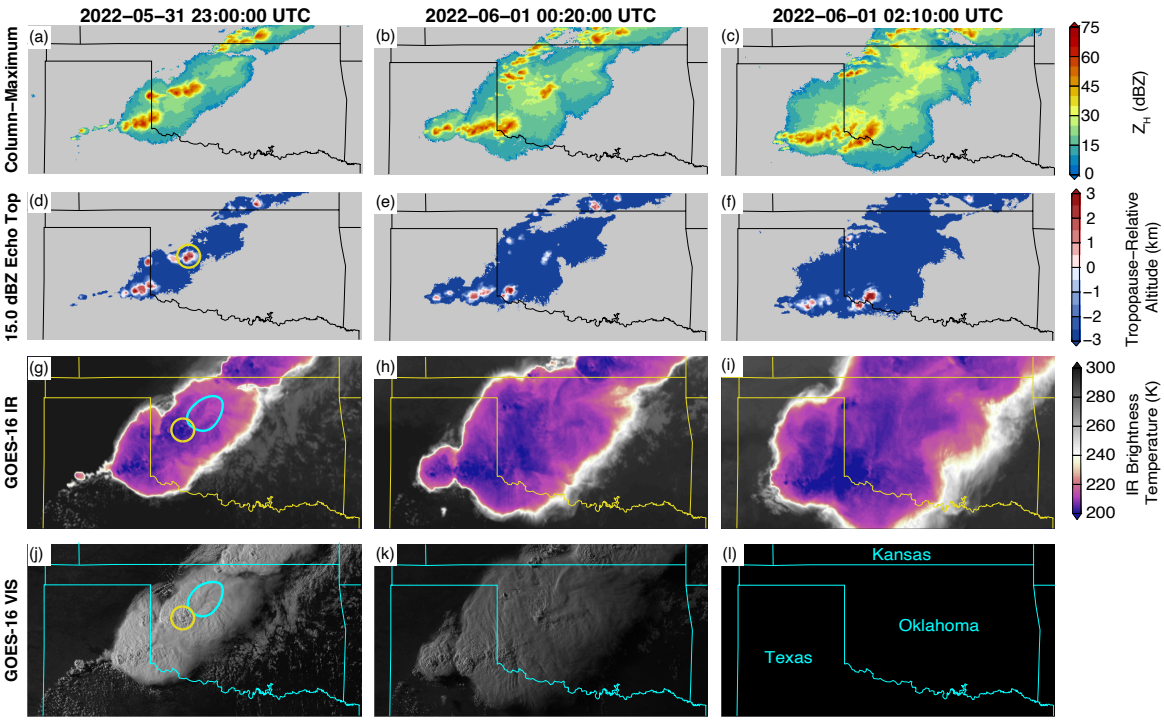


Figure 3.1: From top to bottom, GridRad radar reflectivity (Z_H; panels a–c), GridRad Z_H = 15.0 dBZ tropopause-relative echo top heights (km; panels d–f), GOES-16 infrared imagery (panels g–i), and GOES-16 visible imagery (panels j–l) at: (left) 23:00 UTC on 31 May 2022 (takeoff), (middle) 00:20 UTC on 01 June 2022 (convective sampling begins), and (right) 02:10 UTC on 01 June 2022 (start of the AACP bisects). The latitude and longitude domain span 33.3-37.5°N, 94.0-103.5°W. The targeted overshoot is annotated with a yellow circle, while the targeted AACP is annotated with a cyan oval.

remained until at least ∼03:00 UTC on 1 June. The convectively influenced air from the overshooting storm was advected to the east, while the storm that produced the AACP moved eastward more slowly. As a result, the ER-2 could safely sample the overshoot material downstream of the storm for an extended period of time. The 31 May 2022 flight was the first active convection flight of DCOTSS and the only flight to target an AACP.

Figure 3.2 shows the entire flight track of the 31 May 2022 flight colored by altitude and H_2O measurements, with points of interest labeled. The flight began with takeoff at 22:59 UTC on 31 May 2022 and the ER-2 ascended to an altitude of 20 km while

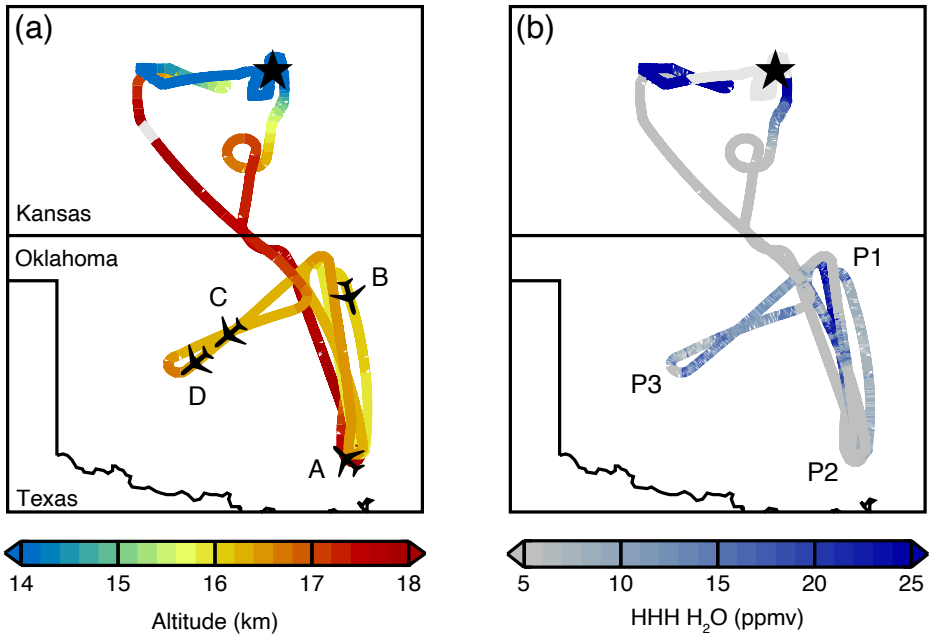


Figure 3.2: ER-2 aircraft flight track for the 31 May 2022 flight shaded by (a) altitude in km, and (b) HHH H_2O in ppmv, spanning a domain of 33.0-39.5°N, 96.0-100.5°W. The star symbol indicates the location of Salina, KS, the base of the DCOTSS field campaign. The plane symbols labeled A, B, C, and D coincide with ER-2 camera imagery shown in Fig. 3.3. Point 1 (P1) is the starting point of the racetrack sampling, point 2 (P2) is the endpoint of the racetrack sampling, and point 3 (P3) was the endpoint of the AACP bisect sampling.

approaching the targeted storms in western Oklahoma, approximately 1-2 hours after their initial overshooting. The aircraft descended to the first level leg at an altitude of 14.5 km near point A at 00:20 UTC (Figs. 3.2 & 3.3a), and completed a series of stacked level legs between points P1 and P2, at altitudes of 14.5, 15, 14.75, 15.5, and 16.5 km (Fig. 3.2). The AACP of the targeted storm can be seen in ER-2 camera imagery from the level legs in Figs. 3.3a (facing forward) and 3.3b (facing right of the aircraft, towards the west). Beginning at 02:07 UTC (∼3:10 hours of flight time), following the radar-indicated collapse of the target cell near point P3 at approximately 01:00 UTC (seen in Fig. 3.1d, e, & f), the ER-2 was able to sample between points P1 and P3 at an altitude of 15.75 km, bisecting the AACP. The ER-2 image midway through the AACP bisect shows a layer of light distinguishing the AACP from the broader anvil below (Fig. 3.3c; facing right of the aircraft). The pilot encountered turbulence near point P3 and briefly ascended to 16.75 km before turning northeast and returning to 15.75 km, resulting in a fortuitous vertical profile through the AACP. Fig. 3.3d shows the AACP as the ER-2 ascends above it during the vertical profile near P3. The camera was again facing to the right. As the ER-2 approached point P1 following the AACP bisect, it was routed back to Salina, KS at 02:48 UTC due to convection near the airport that could impact landing. The ER-2 ascended to an altitude of 20 km and returned to Salina, KS at 04:07 UTC, completing the 5 hour, 8 minute flight.

3.2.2 UTLS Composition Changes

Multiple segments of convectively influenced air at different altitudes were sampled during the 31 May 2022 flight. Figure 3.4a shows a timeseries from 00:17-02:44 UTC on 1 June of WI-ICOS total water (vapor + ice), aircraft altitude, ERA5 tropopause geopotential height, and HHH H_2O, with subjectively-identified convective enhancements in

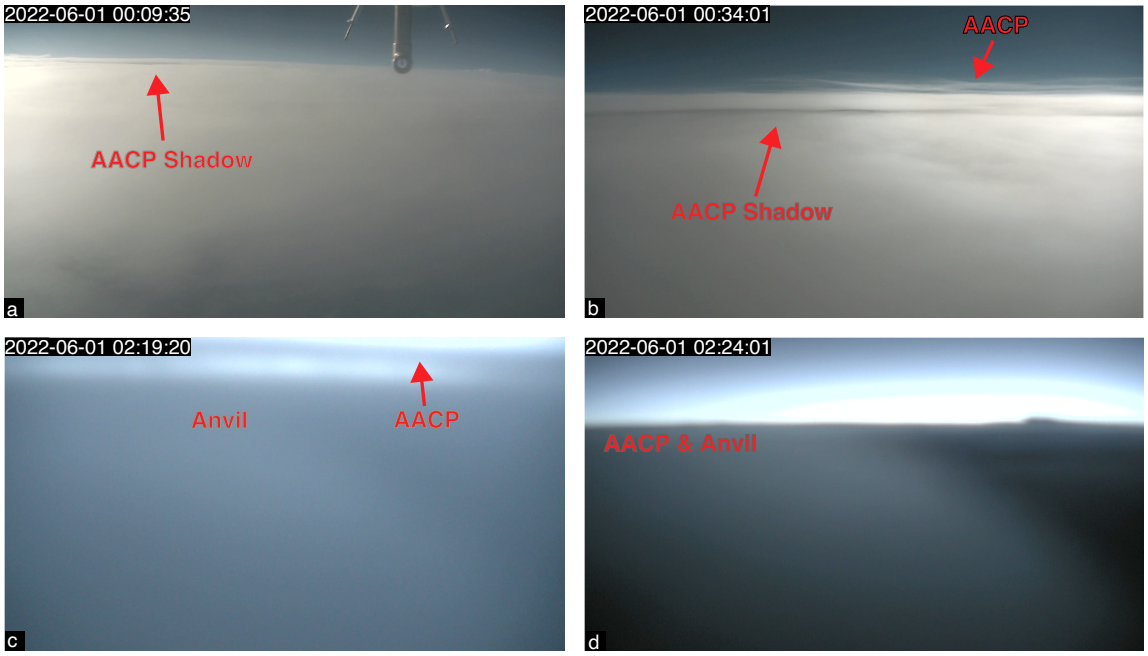


Figure 3.3: Visible imagery from the rotatable camera aboard the NASA ER-2 aircraft taken at (a) 00:09 UTC where the camera is facing forward toward the northwest, (b) 00:34 UTC where the camera is facing right of the aircraft towards the west, (c) 02:19 UTC where the camera is facing right of the aircraft towards the northwest, and (d) 02:24 UTC on 01 June 2022 where the camera is facing to the right of the aircraft toward the northwest. These images correspond to the plane symbols labeled A, B, C, and D in Fig. 3.2.

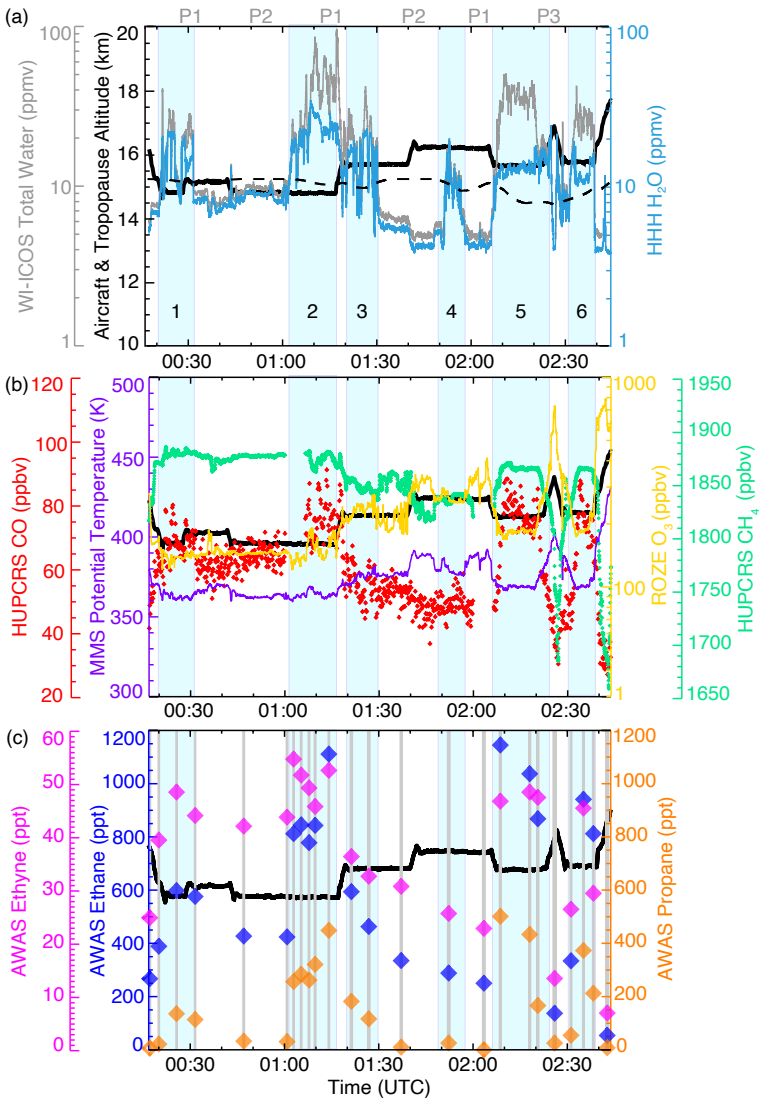


Figure 3.4: The convective sampling period (in UTC) of the DCOTSS 31 May 2022 flight shown as timeseries. All timeseries include the MMS GPS aircraft altitude (thick black line) and illustrations of the convective sampling segments (light blue shading, labeled 1–6 in timeseries (a)). The top timeseries (a) includes WI-ICOS total water (gray), ERA5 LRT altitude (dashed black line), and H_2O mixing ratio (blue). Points P1, P2, and P3 from Fig. 3.2 are labeled (gray) atop timeseries (a). The middle timeseries (b) includes HUPCRS CO (red), MMS potential temperature (purple), ROZE O_3 mixing ratio (yellow), and HUPCRS CH_4 (green). The lower timeseries (c) includes AWAS ethyne (magenta), ethane (blue), propane (orange), and canister fill time (vertical gray bars of varying width).

H_2O (mixing ratios that greatly exceed background at that altitude for several minutes) shaded in blue. Background H_2O mixing ratios in the lower stratosphere range from 4 to 6 ppmv during this flight. The first two H_2O enhancements (convective segments 1 and 2) occur mostly below the tropopause at altitudes of 14.75 km and 15.25 km, with H_2O reaching near ∼30 ppmv. Convective segment 1 contains enhanced H_2O at two altitudes and includes the ascent between them. For both segments 1 & 2, the ER-2 is sampling near or within the tropopause-reaching anvil cloud, as revealed by total water exceeding H_2O periodically during these segments, indicating that ice was present in addition to vapor. Measurements where the difference between H_2O and total water is greater than the combined variability of the two measurements are indicative that the aircraft is within cloud material. The next two convective H_2O enhancements (convective segments 3 and 4) are at higher, stratospheric altitudes of ∼15.75 and ∼16.25 km (0.5-1.5 km above the tropopause), with H_2O reaching up to 20 ppmv (an approximate quadrupling of the background mixing ratio). Enhancement 4 occurs outside of cloud material, as seen by total water being approximately equivalent to H_2O. The final two H_2O enhancements (convective segments 5 and 6) occur within the AACP bisect while the ER-2 is broadly within cloud as total water substantially exceeds H_2O. Elevated H_2O is observed within the AACP before and during the vertical profile, with enhancements spanning 10–20 ppmv that maximize during the vertical profile.

Figure 3.4b is a time series including HUPCRS CO, MMS potential temperature, ROZE O_3, and HUPCRS CH_4. Potential temperature and O_3, stratospheric tracers, follow similar trends to one another throughout the flight, and will be discussed in greater detail in subsequent analysis. CO and CH_4, tracers of tropospheric origin, are substantially elevated above adjacent measurements within the H_2O convective enhancements 5 and 6. CO is also elevated in segments 1 and 2. These four convective segments are when the ER-2 was within cloud, skimming the anvil (convective segments

1 & 2) and bisecting the AACP on either side of the vertical profile (convective segments 5 & 6). The AACP feature will be highlighted further in subsequent analyses. It is worth noting that while H_2O is enhanced at the beginning of the vertical profile (near the end of convective segment 5), tropospheric tracers are not. This leaves segments 3 and 4, when the ER-2 is sampling predominantly outside of cloud and at stratospheric altitudes, as primarily a H_2O signal. Tropospheric tracers, such as CO and CH_4, experience greatest convective enhancement within cloud material (convective segments 2, 5, and 6), especially within the AACP, and at closer proximity to the tropopause altitude (convective segment 1). CO reaches near 90 ppbv at an altitude of 14.75 km while the ER-2 is skimming the anvil beneath the tropopause, and is enhanced to ∼87 ppbv within the AACP bisect (∼1.2 km above the tropopause, where the typical background mixing ratio is ∼40 ppbv). These results show that CO and CH_4 reach similar enhancement within the AACP compared to the anvil, even though the AACP is above the tropopause and occurs at a higher altitude and potential temperature. The maximum altitude of elevated H_2O for the 31 May 2022 flight occurred out of cloud material and was linked to the target storm at an altitude of ∼17 km (∼2 km above the LRT) during the final ascent to return home (at ∼02:42 UTC, which is not shaded in Fig. 3.4a), while the maximum altitude of elevated tropospheric tracers was 15.75 km (∼1.2 km above the LRT) and occurred within the AACP (convective segment 6). The maximum altitude of enhanced H_2O relative to the ERA5 tropopause was 2.3 km and occurred out of cloud material but within the vertical profile of the AACP (near the end of convective segment 5 in Fig. 3.4a). Thus, it is abundantly clear from these measurements that H_2O enhancements reached higher absolute and tropopause-relative altitudes than tropospheric tracers, which is consistent with a common yet unexplained result from previous modeling work (Homeyer, 2015; Phoenix and Homeyer, 2021, Chapter 2). Specifically, both previous modeling work and these observational results

indicate that elevated H_2O can reach stratospheric altitudes at least 1 km higher than enhanced passive tracers.

Since longer-lived tropospheric tracers (CO and CH_4) appear to be most enhanced within cloud material, shorter-lived tracers from AWAS samples are examined as well. Figure 3.4c is a timeseries of AWAS ethane, ethyne, and propane. Overall, these short lived tracers exhibit similar characteristics to the CO and CH_4 measurements as they are most enhanced when the ER-2 is within cloud material (predominantly convective segments 2, 5, and 6). In particular, ethane and propane maximize within the AACP bisect (convective segments 5 and 6), reaching 1145 ppt and 501.4 ppt, respectively. Ethyne also exhibits enhancements throughout the 31 May 2022 flight, with a maximum of 54.6 ppt occurring within the anvil segment (convective segment 2), and additional enhancements within the AACP peaking at 48.4 ppt (convective segments 5 and 6). Enhancements in ethyne, ethane, and propane demonstrate a clear signal for stratospheric delivery of short-lived tropospheric trace gases from oil and natural gas sources when sampling within cloud for the 31 May 2022 flight, with limited enhancement outside of cloud material. Furthermore, nearly all tropospheric gases measured during DCOTSS were enhanced within the AACP and anvil, including maximum values of multiple tropospheric gases measured during the AACP (e.g., ethane and propane shown here) rather than the anvil (e.g., ethyne, CO, and CH_4). This supports the distinct impact of AACP-producing storms on UTLS composition, as suggested in prior model simulations (Homeyer et al., 2017; O'Neill et al., 2021, Chapter 2).

Given the demonstrated unique impact of the AACP on tropospheric tracer and H_2O enhancements in the lower stratosphere, this chapter focuses on the AACP samples and vertical profile to further examine these composition changes and gain insight into what processes could be occurring. To provide context for the detailed evaluation of AACP sampling that follows, Fig. 3.5 illustrates how the storm was sampled by the

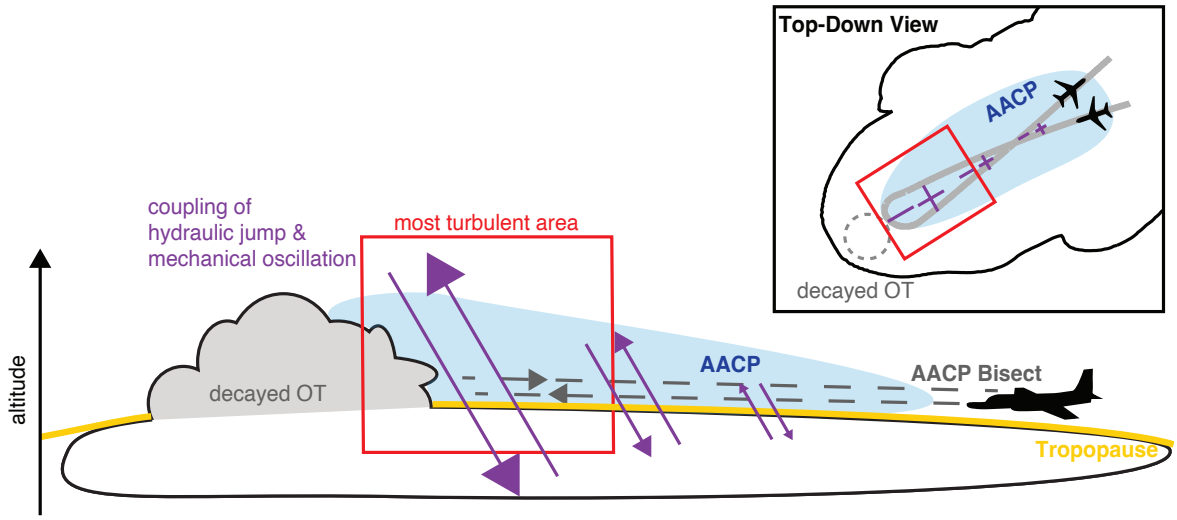


Figure 3.5: An illustration of AACP sampling during the 31 May 2022 flight. Dynamic processes which would be expected to encounter (based on prior modeling work) and their feature-relative locations are indicated, including the decayed overshoot (gray), the AACP (blue), mixing associated with the coupling of the hydraulic jump and mechanical oscillation (purple), and the expected location of maximum turbulence (red). The ER-2 is shown in black, and an outline of the flight track along the AACP bisects is denoted in gray in the top-down view panel.

ER-2 and what dynamic features one would expect to encounter throughout the AACP bisect based on insights from prior modeling work. The ER-2 bisected the AACP while traveling towards the decayed overshoot where it encountered a region with increasing turbulence, eventually resulting in a turbulence-avoidance vertical profile near the location of the decayed overshoot. The co-location of the most turbulent area with the overshoot is a common result in all modeling work focused on AACP-producing storms, owing to the establishment of a hydraulic jump that leads to gravity wave breaking and AACP formation (as outlined in the Introduction). This is also the location where a coupling of the hydraulic jump and overshoot-driven mechanical oscillation lead to increased vertical mixing and enhanced downward transport of overworld air to the lowermost stratosphere (Chapter 2). Simulations show the mechanical oscillation decreases in magnitude as distance from the overshoot increases, further contributing to

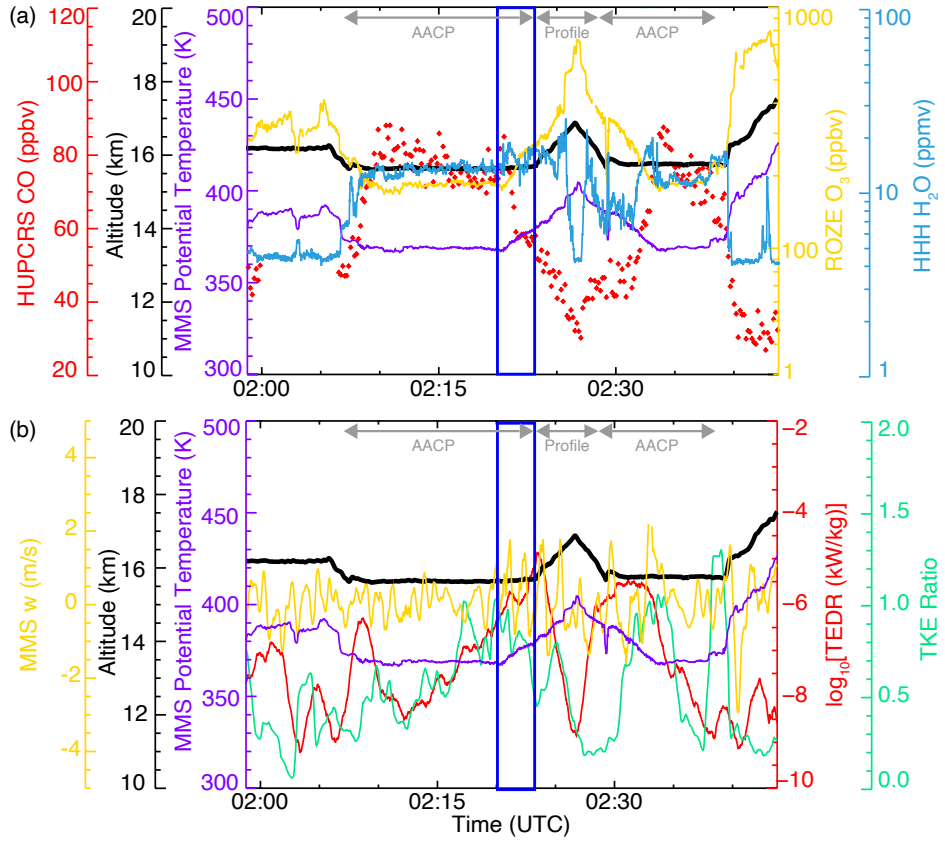


Figure 3.6: AACP sampling during the 31 May 2022 flight (in UTC) shown as timeseries. Both timeseries include the MMS GPS aircraft altitude (thick black line) and potential temperature (purple line). The top timeseries (a) uniquely includes HUPCRS CO (red), ROZE O_3 mixing ratio (yellow), and HHH H_2O mixing ratio (blue). The lower timeseries (b) uniquely includes MMS measurements of the vertical wind speed (m s^{-1}; yellow), the $\log_{10}$ of the Turbulent Eddy Dissipation Rate (TEDR; red), and the vertical-to-horizontal TKE ratio (green). The dark blue box in each timeseries denotes the time period of the 'stratospheric signal' near the end of the first AACP bisect, and gray horizontal lines with arrows at each end denote times when the ER-2 is within the AACP and in the turbulence-avoidance vertical profile.

the area near the overshoot being the most turbulent. It is through this model-informed lens of transport and mixing processes and the known storm-relative sampling during this flight that is used to interpret the in situ data collected during the AACP sampling.

To examine composition changes within the AACP bisect and vertical profile components of the 31 May 2022 flight, Fig. 3.6a is a timeseries from 1:59–2:44 UTC and includes HUPCRS CO, MMS GPS Altitude, MMS Potential Temperature, ROZE O_3, and HHH H_2O. The AACP bisect begins at ∼02:07 UTC and continues until the turbulence-avoidance vertical profile occurs from 02:23–02:28 UTC, and resumes thereafter until 2:39 UTC when the ER-2 begins to ascend to maximum altitude and return to Salina. Tropospheric tracers, such as CO, are elevated within both passes through the AACP, with an exception near the ends of the horizontal segments bounding the vertical profile. Note that CO data from 02:00–02:06 UTC are missing due to a routine in-flight calibration of the HUPCRS instrument. Potential temperature and O_3 begin to increase at 02:20 UTC, shortly before the vertical profile begins and when altitude is constant. The increase in stratospheric tracers and decrease in tropospheric tracers (except for H_2O) at constant altitude suggests a reduction in the amount of tropospheric air transport to the stratosphere (i.e., a H_2O-dominant convective signature with no or minimal impacts to other trace gases). This apparent "stratospheric signal" at constant altitude (annotated in Fig. 3.6a) implies a change in the physical/dynamic process leading to convectively influenced air above the tropopause. A change in controlling processes is also likely present within the second AACP bisect, as potential temperature and O_3 are elevated and then decrease while at constant altitude. Note that inspection of ERA5 output suggests there are no alternative large-scale explanations for an increase in potential temperature from a pre-existing isentropic gradient in this region. Therefore, the stratospheric signal, evident as a unique signature in trace species concentrations distinct from those in the broader AACP feature, suggests

different mixing processes are occurring near the end of the first AACP bisect and the beginning of the second AACP bisect (02:28–02:33 UTC) closest to the decayed overshoot.

To identify what processes are primarily driving the stratospheric signal (corresponding with the time that substantial turbulence was encountered, resulting in the eventual ascent of the ER-2 out of the AACP), this chapter examines the turbulent energy dissipation rate (TEDR), turbulence kinetic energy (TKE), and vertical wind speed measured by MMS (w; Fig. 3.6b). TEDR combines both vertical and horizontal components of turbulent motion in one metric, and was smoothed with a 90-second centered average to show turbulent bursts throughout the flight. Horizontal and vertical TKE was calculated using MMS wind speeds after application of a high-pass filter (removing power at time scales greater than 4 seconds to isolate turbulent motions) followed by calculating the 20-second variance of these filtered winds. A 90-second centered average was then applied to the horizontal and vertical TKE components before calculating the ratio (vertical:horizontal) shown in Fig. 3.6b. These time intervals were chosen to best capture the spatial and temporal differences throughout the flight. The absolute vertical winds are also shown to provide additional context, which were calculated using a low pass filter (removing power at time scales less than 4 seconds, thus emphasizing the broader scales of motion including those at the scale of gravity waves and the hydraulic jump) and applying a 20-second average to be consistent with the 20-second variance used for TKE calculations.

Converting displayed $\log_{10}$(TEDR) values to TEDR dissipation rates throughout this portion of the flight shows an increase in turbulent motion within the stratospheric signal prior to the vertical profile (near 10^{-2} W/kg at 02:23 UTC), and within the AACP following the vertical profile (near $3.2*10^{-3}$ W/kg at 02:31 UTC). This suggests that peak turbulence is occurring within the stratospheric signal and near the decayed

overshoot, coinciding with the turbulence-avoidance vertical profile. This is consistent with what is expected based on Fig. 3.5, where the most turbulent region within the AACP is located near the overshoot. Examining the TKE ratio within these areas of elevated TEDR provides additional insight towards the contributions of vertical and horizontal mixing to the increasing turbulence. For the majority of the 31 May 2022 flight, horizontal TKE exceeds vertical TKE, as indicated by the TKE ratio being consistently well below a value of 1. However, there is a rapid increase in TKE ratio to a value near 1 shortly prior to and within the stratospheric signal during the first (02:17–02:23 UTC) and second (02:31–02:35 UTC) AACP bisects. This suggests that increased vertical mixing is associated with the emergence of the stratospheric signal. It is worth noting that the TKE ratio also increases to a value near 1 (suggesting increased vertical mixing) within elevated TEDR at a flight time of approximately 02:31 UTC. This coincides with sampling the AACP cloud boundary following descent from the short vertical profile, which resides within the most turbulent area of the AACP near the decayed overshoot (as seen in Fig. 3.5dcotss). Similar trace gas changes, including decreasing O_3 with increasing H_2O and CO, are seen near these vertical TKE peaks in Fig. 3.6a. Low-pass filtered vertical wind speed (w) provides additional context towards the contributions of vertical mixing with turbulent regions. Throughout the majority of the sampling period shown in Fig. 3.6b, w oscillates between -0.5 and 0.5 m s^{-1}. However, the oscillation increases in magnitude throughout the first AACP bisect, and reaches a range of near -1 to 1 m s^{-1} at the onset of the stratospheric signal (when the ER-2 is near the decayed overshoot). Similarly, w shows a strong oscillation within the second AACP bisect following the descent from the vertical profile ranging from -1.5 to 2 m s^{-1}, when the ER-2 is near the decayed overshoot. A stronger oscillation and vertical mixing near the decayed overshoot is in agreement with the key dynamic mechanisms illustrated in Fig. 3.5, where vertical mixing associated with

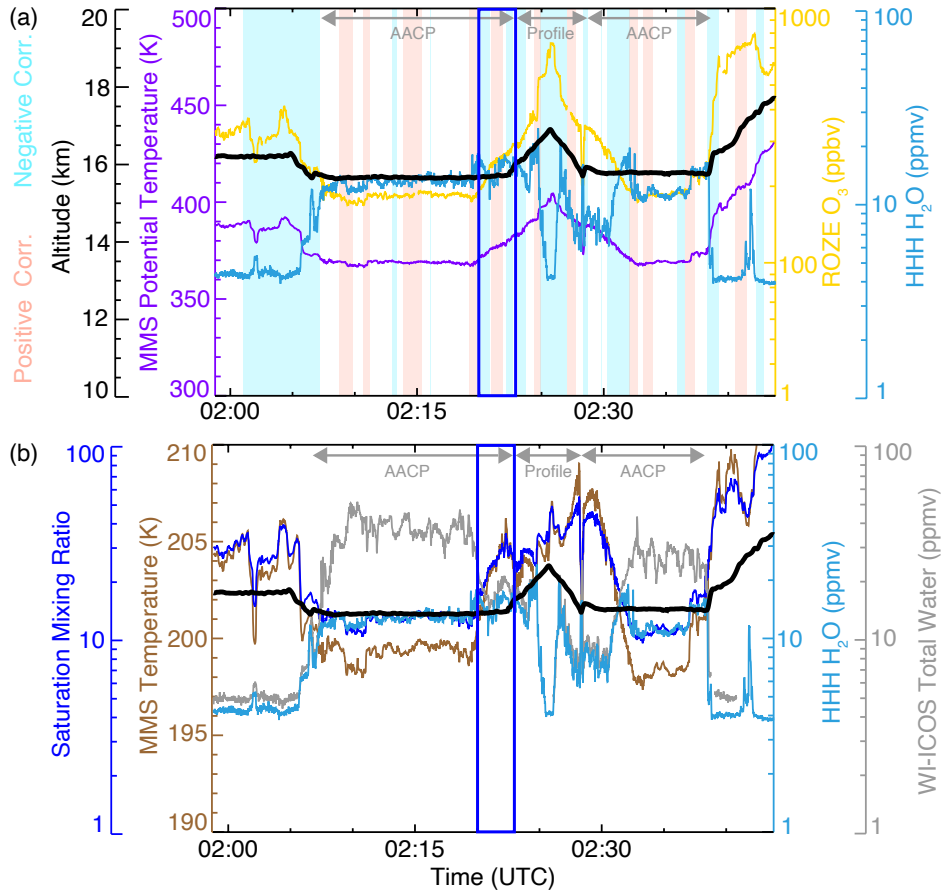


Figure 3.7: As in Fig. 3.6, but with top timeseries (a) of MMS GPS altitude (black), MMS potential temperature (purple), ROZE O_3 mixing ratio (yellow), HHH H_2O mixing ratio (blue), positive O_3-H_2O correlations (blue shading), and negative O_3-H_2O correlations (pink shading). The lower timeseries (b) includes MMS GPS altitude (black), MMS saturation mixing ratio (dark blue), MMS temperature (brown), H_2O mixing ratio (light blue), and WI-ICOS total water (gray).

the coupling of the hydraulic jump from the AACP and overshoot-induced mechanical oscillation is strongest near the overshoot and decreases in strength as distance from the overshoot increases. Given this close coupling between prior simulations and the DCOTSS measurements, it is therefore believed that the stratospheric signal represents the downward mixing of stratospheric air from higher altitudes in the vicinity of the coupled hydraulic jump and mechanical oscillation.

Next, this chapter examines relationships between O_3 and H_2O during the AACP

bisect and in the segment with the stratospheric signal where the O_3 mixing ratio increases. O_3-H_2O correlations for the AACP bisect and profile components of the 31 May 2022 flight are shown in Fig. 3.7a. Strong linear correlations were identified via the Pearson correlation coefficient, which was calculated over an observation-centered time window of ± 10 seconds. A strong positive correlation is considered to be ≥ 0.5 and, similarly, a strong negative correlation is ≤ -0.5. There are many strong negative and positive O_3-H_2O correlations throughout the AACP bisect. These correlations can change frequently as the ± 10-second time window captures fine scale changes within the dynamic environment being sampled and helps mitigate potential biases that result from pre-existing large-scale gradients in the trace gases. Correlations are least informative during vertical profiling since they can arise directly from the pre-existing vertical gradients in these trace gases, especially the rapid increase in O_3 with altitude in the stratosphere. The variety of positive and negative correlations seen in constant-altitude segments suggests that varied physical and dynamic constraints may be important to the composition impacts and resulting correlation, with some processes dominating over others. Generally, with overshooting convection it is expected that air of high H_2O, cloud ice, and low O_3 composition will mix with stratospheric air of high O_3 and low H_2O composition, resulting in a negative O_3-H_2O correlation (Fig. 3.8). Therefore, it is not surprising to see the frequency of negative O_3-H_2O correlations associated with STE. The occurrence and frequency of positive O_3-H_2O correlations was unexpected. There are multiple positive correlations coinciding with the AACP bisect and at the onset of stratospheric signal. To better understand the potential factors leading to positive O_3-H_2O correlation, this chapter further examines multiple tracers and meteorological variables.

Figure 3.7b shows a time series for the AACP bisect and profile components of the 31 May 2022 flight including MMS temperature, the saturation mixing ratio (SMR),

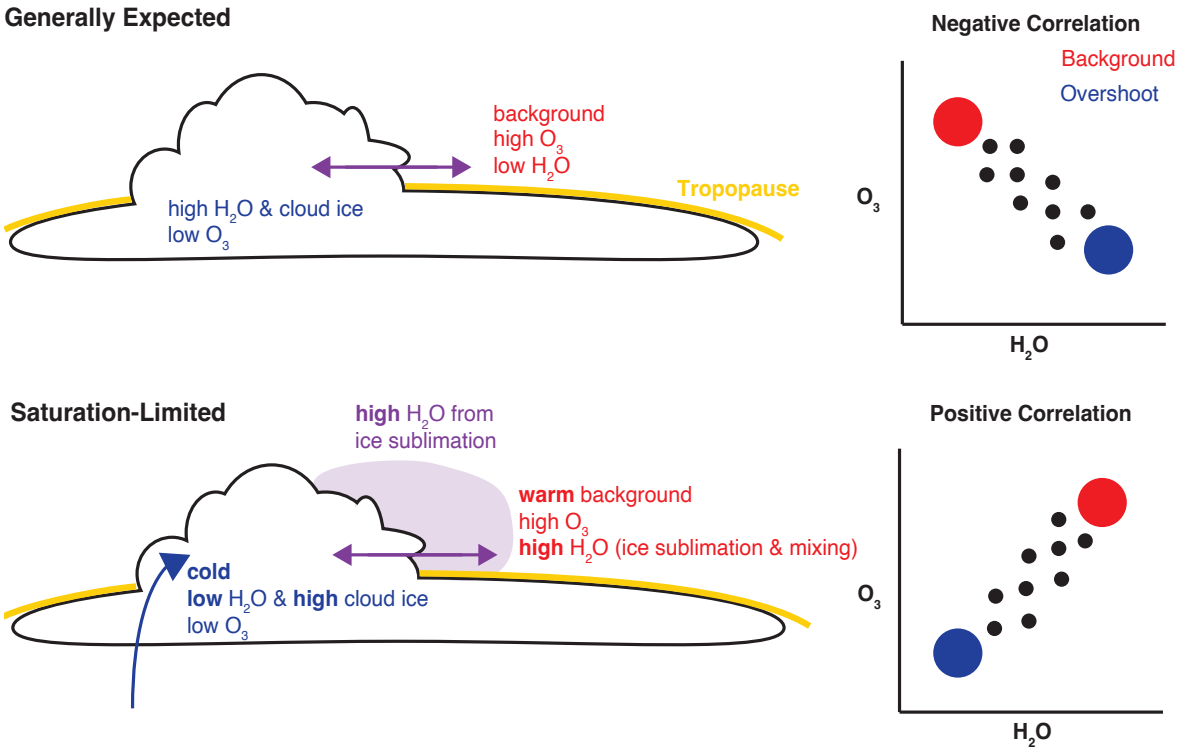


Figure 3.8: Illustration of the process that is generally expected for an overshoot which results in a negative O_3-H_2O correlation (top panels), and a saturation-limited overshoot and hypothesized process resulting in a positive O_3-H_2O correlation (bottom panels).

HHH H_2O, and WI-ICOS total water (vapor + ice). During the first AACP bisect (flight time of 02:07-02:22 UTC), temperature broadly decreases to ∼199 K, followed by a sharp increase to ∼206 K during the stratospheric signal (beginning at 02:20 UTC), consistent with sampling a warmer stratospheric environment. Total water also drops at the onset of the stratospheric signal from 30-40 ppmv to 10-20 ppmv, while H_2O remains elevated between 10 and 20 ppmv. Such changes in total water and H_2O at this time suggest that mixing of AACP air with the warmer stratospheric environment is significant, which is in agreement with prior analyses and with the broad occurrences of negative O_3-H_2O correlations at the beginning and end of this time segment. In contrast, when the temperature is low throughout the remainder of the first AACP bisect, H_2O is nearly equal to the SMR, demonstrating that the air is saturated and H_2O within the convectively lofted air is constrained to the SMR. Notably, the O_3-H_2O correlations observed during this saturation-limited period of sampling are almost entirely positive. When the temperature increases at the onset of the stratospheric signal, the SMR exceeds H_2O and the air becomes subsaturated while the O_3-H_2O correlation sign flips to negative. When the temperature rapidly decreases following the vertical profile and near the start of the second AACP bisect, total water rapidly increases to values exceeding H_2O and the AACP air is once again saturated. Similar patterns in the O_3-H_2O correlations are also observed within the second AACP bisect. Given these relationships, a plausible explanation for the occurrence of positive O_3-H_2O correlations is that H_2O within the overshoot and AACP air is saturation-limited due to the low temperature within the overshoot. In the absence of a saturation-limited condition at low temperatures, there is significantly more H_2O in the overshoot than the stratospheric environment. However, with these particular overshoots, the temperature decreases to a point where the SMR is less than the maximum possible H_2O concentration in the environmental stratospheric air, resulting in less water in

the vapor phase and more in the ice phase within the overshoot. To account for this H_2O imbalance, the cloud ice along the periphery could preferentially sublimate into the warm stratospheric environment (rather than remaining in the overshoot), while subsequent mixing between this hydrated stratosphere air and the relatively dry overshoot leads to a positive O_3-H_2O correlation, as illustrated in Figure 3.8.

While the preceding analyses have been focused on understanding the dynamic and physical processes constraining stratospheric hydration and STE, one question that remains is whether the 31 May 2022 AACP observations differ from the typical range of lower stratosphere composition impacts from overshooting convection (AACP-producing or otherwise). Therefore, to assess the uniqueness of these active convection observations, measurements of H_2O and CO from the 31 May 2022 flight are compared to samples of overshooting convection from all other DCOTSS research flights. Figure 3.9 shows the density of convective observations as a function of trace gas concentration and ERA5 LRT-relative altitude, with the convective observations (red) and AACP observations (yellow) from the 31 May 2022 flight overlaid. For additional context, the density of background (i.e., non-convective) observations from all DCOTSS flights except for the 31 May 2022 flight are shown in additional panels. Background DCOTSS observations of CO range from 28-70 ppbv near the tropopause and 10-50 ppbv throughout much of the stratosphere. Convective samples from remaining DCOTSS flights span approximately 40-95 ppbv near the tropopause and 20-60 ppbv throughout much of the lower stratosphere (up to $\sim$3 km above the tropopause). Most of the enhanced CO (>40 ppbv) in convective samples at an LRT-relative altitude of 2-3 km originate from the 08 June 2022 and 10 June 2022 flights that targeted recent/active convection (not shown). Measurements from the 31 May 2022 active convection flight show an above-average mixing ratio of CO in overshoot material, and exceptional values within the AACP at a LRT-relative altitude of 0.5-1.2 km. The majority of H_2O

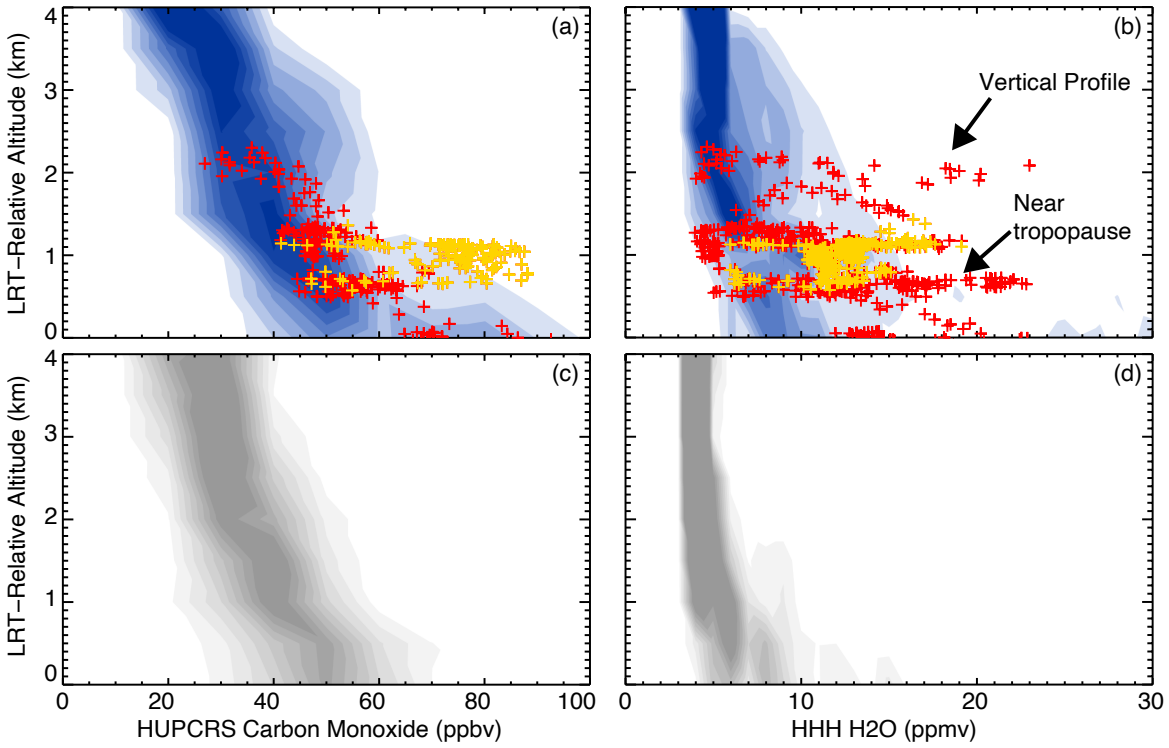


Figure 3.9: Density of CO (left) and H_2O (right) in LRT-relative altitude of convective segments (blue; a and b) and background segments (gray; c and d) from all DCOTSS 2021 and 2022 flights except for the 31 May 2022 flight. Convective sampling from 31 May 2022 flight (red) and AACP sampling from 31 May 2022 flight (yellow) are shown atop the respective convective sampling densities. Density is determined using a 10.0 ppbv x 0.5 km bin resolution for CO and a 1.0 ppmv x 0.5 km bin resolution for H_2O. For the 31 May 2022 convective samples, every 5th H_2O measurement is shown to be more consistent with the frequency of CO, which results in no loss of qualitative detail. Measurements obtained when skimming the anvil near the tropopause and during the vertical profile are annotated.

convective sampling for all DCOTSS flights ranges from 3-15 ppmv, while the density of background observations is 3-5 ppmv throughout much of the stratosphere, especially at LRT-relative altitudes >1 km. The 31 May 2022 active convection flight sampling of H_2O is largely consistent with convective measurements from other DCOTSS flights, with greater extremes than those commonly measured at altitudes near the tropopause and >1.5 km above the tropopause. The most prominent example of exceptional H_2O observed during the 31 May 2022 flight is near a LRT-relative altitude of ∼2.1 km where H_2O reaches ∼23 ppmv. This H_2O enhancement occurs within the vertical profile as the ER-2 emerged from the first AACP bisect and stratospheric signal, which was primarily a H_2O convective signal (as tropospheric tracers were not strongly enhanced). H_2O sampled within the AACP bisects is near or slightly above the typical range of H_2O mixing ratios for all DCOTSS convective sampling at the LRT-relative altitudes spanned by the AACP. As demonstrated in Fig. 3.8, H_2O concentrations in the AACP are limited by the SMR set by the low temperatures in the AACP air, making these enhancements less exceptional than those seen with CO compared to remaining DCOTSS flights.

3.3 Summary

This chapter analyzes observations from the DCOTSS 31 May 2022 flight obtained within convective outflow and an actively-generated AACP from a storm over Oklahoma. UTLS composition changes from the storm are evaluated and discussed in comparison with results from recent model simulations. Multiple segments of convectively influenced air with pronounced changes in stratospheric hydration and air mass composition were sampled throughout the flight. Consistent with previous modeling studies, observations showed that H_2O enhancements reached higher altitudes than

passive tropospheric tracer enhancements (Figs. 3.4 & 3.6a). Convective enhancements of short-lived tracers including CO, ethyne, ethane, and propane were found to be most enhanced when sampling within cloud material, specifically when bisecting the storm anvil and AACP (Figs. 3.4 & 3.6a). This suggests that AACP-producing storms have a unique impact on UTLS composition, especially with respect to TST of tropospheric air. In addition to enhanced tropospheric tracers within the AACP, there was an apparent "stratospheric signal" at constant altitude near the end of the first AACP bisect and beginning of the second AACP bisect, where O_3 and potential temperature increased while CO, CH_4 and total water decreased and H_2O remained elevated (or vice versa). This stratospheric signal seems to be associated with enhanced vertical mixing, based on both composition changes and turbulence analyses (Fig. 3.6b). Observations of vertical mixing and downward transport of deeper stratospheric air near the AACP edge (in close proximity to the once-active overshooting top) supports the novel finding in recent modeling work (Chapter 2). O_3-H_2O correlations were examined throughout the flight, and multiple fine-scale positive and negative correlations were observed. There are notable positive O_3-H_2O correlations throughout the AACP bisects that appear to be the result of preferential sublimation of cloud ice into the warm stratospheric environment and subsequent mixing between overshoot/AACP and hydrated stratosphere air (illustrated in Fig. 3.8). Tropospheric tracer enhancements including CO and H_2O observed from the 31 May 2022 flight are unique compared to remaining DCOTSS flights. While H_2O enhancements observed during the AACP bisect were not extraordinary in comparison to remaining observations during the flight due to the aforementioned saturation-limited condition, CO measurements within the AACP are exceptional when compared to remaining DCOTSS observations (Fig. 3.9). These comparisons support the perceived impactful nature of AACPs on air mass composition within the UTLS inferred from model simulations, in addition to their

increasingly-appreciated impact on stratospheric hydration.

Chapter 4

Examining Stratosphere-Troposphere Exchange in Idealized Simulations of Tropical Cyclones

Previous studies exploring STE in TCs have revealed contributing processes, however there is limited understanding regarding which STE processes are most influential on overall STE and how much total STE occurs in a TC. One contributing factor towards this limited knowledge is that previously identified processes were studied or revealed predominantly in case studies and have not been comprehensively or complementarily tested from modeling systems or multiple observational platforms, of which the former will be addressed in this chapter. It also remains unknown how TC intensity and environmental deep-layer VWS impacts the amount and role of STE processes. Motivated by these limitations, this chapter seeks greater understanding of the influence of various STE processes within TCs and their impact on UTLS composition change. Three idealized simulations of tropical cyclones are carried out using the 3-D TC setup of the Bryan Cloud Model 1 (CM1) to address these questions. A suite of customized passive tracers and H_2O are used to quantify transport between the stratosphere and

troposphere. The first two questions are addressed using a simulation with maximum SST and no deep-layer VWS ($TC_{noshear}$), the analysis of which is published in Gordon and Homeyer (2025). The third question is addressed using a simulation with reduced SST (TC_{lowSST}) and a simulation including moderate deep-layer VWS (TC_{shear}).

4.1 Model Setup and Design

4.1.1 Model Configuration

Release 21.0 of the Cloud Model 1 (CM1) is used in this chapter (Bryan and Fritsch, 2002). CM1 is a three dimensional, non-linear, non-hydrostatic, time-dependent numerical model that is commonly used for convective studies. Here, three idealized TC simulations using the CM1 3D TC set-up are designed and carried out, which by default includes a modified Rankine vortex on an f plane. No background wind speed is included in the initial conditions for the first simulation ($TC_{noshear}$), which has a base SST of 29°C and serves as the "control" simulation. The second simulation has no background wind speed and a base SST of 27°C, to generate a weaker "steady-state" TC. The third simulation, as in $TC_{noshear}$, has a base SST of 29°C, but incorporates moderate deep-layer (850–200 hPa) westerly VWS (TC_{shear}), which is gradually introduced during the first 12 hours of integration and reaches a maximum magnitude of 6 m s^{-1} thereafter (Rios-Berrios et al., 2018).

A reference latitude of 20°N is used for all three simulations, which corresponds to a domain-wide Coriolis parameter (f) of 0.00005 s^{-1}. The horizontal grid spacing is 2 km within 1000 km of the domain center, beyond which the grid stretches incrementally from 2 km to 60 km at the outermost extent of the domain. The total size of the domain is 10,052 km × 10,052 km. Open lateral boundary conditions are employed. The

vertical grid spacing stretches from 20 m at the surface to 200 m by an altitude of 5060 m, above which the vertical grid spacing remains constant at 200 m up to the model top of 25060 m. The horizontal grid tracks with the TC center over time, ensuring that the TC core remains at grid center. The model is initialized using the (Dunion, 2011) moist tropical temperature profile with adjustments to stratospheric H_2O mixing ratio to be uniformly low (4–4.5 ppmv) at all altitudes above the tropopause and thus more comparable to observed background concentrations (e.g., Tilmes et al., 2010). The Yonsei University (YSU) planetary boundary layer parametrization (Hong et al., 2006) is employed. Additional parametrization schemes employed in the model include Morrison double-moment microphysics (Morrison et al., 2009) and horizontal Smagorinsky turbulence (Bryan and Rotunno, 2009). No radiative effects are included, as the domain size is too large for idealized implementation.

4.1.2 Passive Tracer Design

A set of custom passive tracers in the CM1 simulations is implemented that includes tropospheric, stratospheric, and convective tracers, which are used in combination with H_2O to evaluate cross-tropopause transport. A boundary layer tracer (PT_{bl}) is initialized as 100% of the air mass at altitudes less than 1000 m (the approximate top of the boundary layer in the idealized environment). The stratospheric passive tracer (PT_{strat}) is set to 100% at altitudes above the initial tropopause height of 16.6 km. The initial tropopause was calculated using the lapse-rate tropopause (LRT; World Meteorological Organization, 1957) and potential temperature gradient tropopause (PTGT; Tinney et al., 2022) definitions. The LRT and PTGT tropopause definitions were evaluated throughout the simulation and both yielded similar results but, due to the complex changes within convection, neither produce reliable definitions of the transition between the troposphere and stratosphere beyond initialization. Therefore, an

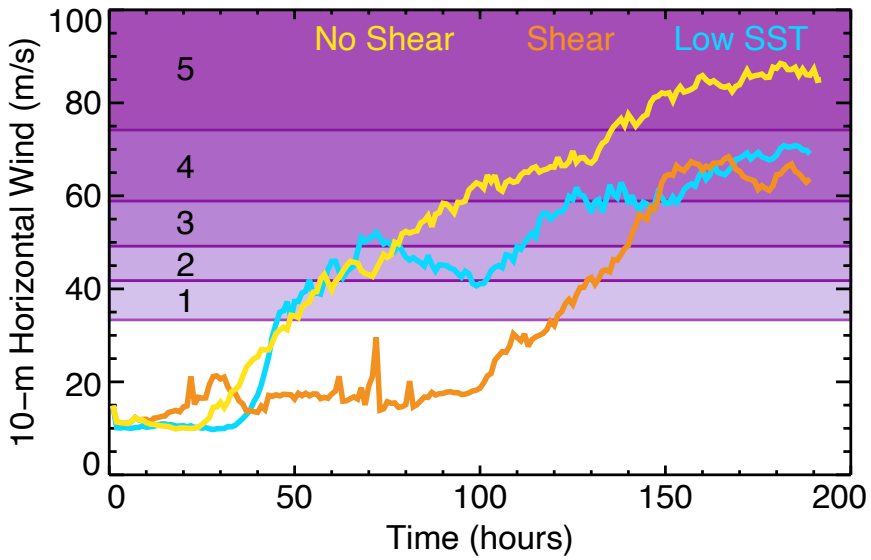


Figure 4.1: Maximum azimuth-averaged 10-m horizontal wind speed within 500 km of TC center throughout the model run time of 192 hours for all simulations, with hurricane categories 1-5 shaded and annotated based on the Saffir-Simpson Hurricane Wind Scale.

isentrope of 383 K is used to approximately represent the tropopause altitude, which remains broadly coincident with trustworthy LRT and PTGT definitions throughout the simulation. The convective passive tracer (PT_{conv}) is designed specifically to track convectively-influenced air over time. This tracer is initialized as 0 everywhere and re-initialized as 100% at each model time step in volumes where vertical wind speed is greater than or equal to 2 m s^{-1} and cloud is present (sum of cloud droplet and ice mixing ratios is greater than 1.0×10^{-6} kg kg^{-1}), following similar implementation in the Weather Research and Forecasting (WRF) model by Phoenix and Homeyer (2021).

4.2 Results

The TC simulations are run for 8 days (192 hours) and reach a peak intensity consistent with a Category 5 hurricane ($TC_{noshear}$) or a Category 4 hurricane (TC_{lowSST} and TC_{shear}), based on the Saffir-Simpson Hurricane Wind Scale. The evolution of the

maximum 10-meter azimuthally averaged horizontal wind of the TC simulations are shown in Fig. 4.1.

To explore bulk composition change for each simulation, average profiles of H_2O, PT_{bl}, and PT_{strat} within the inner TC ($\leq$300 km), outer TC (300–1000 km), and total TC (0-1000 km) at the end of each simulation (hour 192) are shown in Fig. 4.2. Stratospheric hydration is greatest overall in $TC_{noshear}$, followed by TC_{shear} and TC_{lowSST}, respectively (Fig. 4.2a,b,c). Within the TC, stratospheric hydration is greatest within the inner core. Similarly, TST of boundary layer air is greatest in $TC_{noshear}$, followed by TC_{shear} and TC_{lowSST} (Fig. 4.2d,e,f). Although TC_{shear} and TC_{lowSST} have less transport to the stratosphere, TC_{lowSST} has the greatest transport to the upper troposphere at the maximum outflow altitude. Overall, the inner and outer TC have similar contributions to TST of boundary layer air. Focusing on the stratospheric tracer reveals that STT overall (Fig. 4.2g) and in the TC inner core (Fig. 4.2i) is greatest in TC_{shear}, while the outer TC has the most STT in TC_{shear} and TC_{lowSST} depending on altitude (Fig. 4.2h). However, overall differences between the simulations for STT are slight. This analysis suggests that STE processes contributing to stratospheric hydration and TST may be more influenced by changes in intensity and VWS than those affecting STT.

As previously discussed, overshooting tops are a known process by which STE occurs, within and outside of TCs. Thus, the frequency of overshooting tops is examined throughout our TC simulations (Fig. 4.3). To explore overshoot frequency within the TC, pronounced overshoots (cloud tops reaching or exceeding an altitude of 17.56 km - approximately 1 km above the initial tropopause) are counted within each grid box. The resulting spatial distribution of overshoots (Fig. 4.3a) in $TC_{noshear}$ shows that they are most frequent in the inner TC (within 150 km of TC center), where the southern half experiences the greatest amount of overshoots. This suggests that overshoots pri-

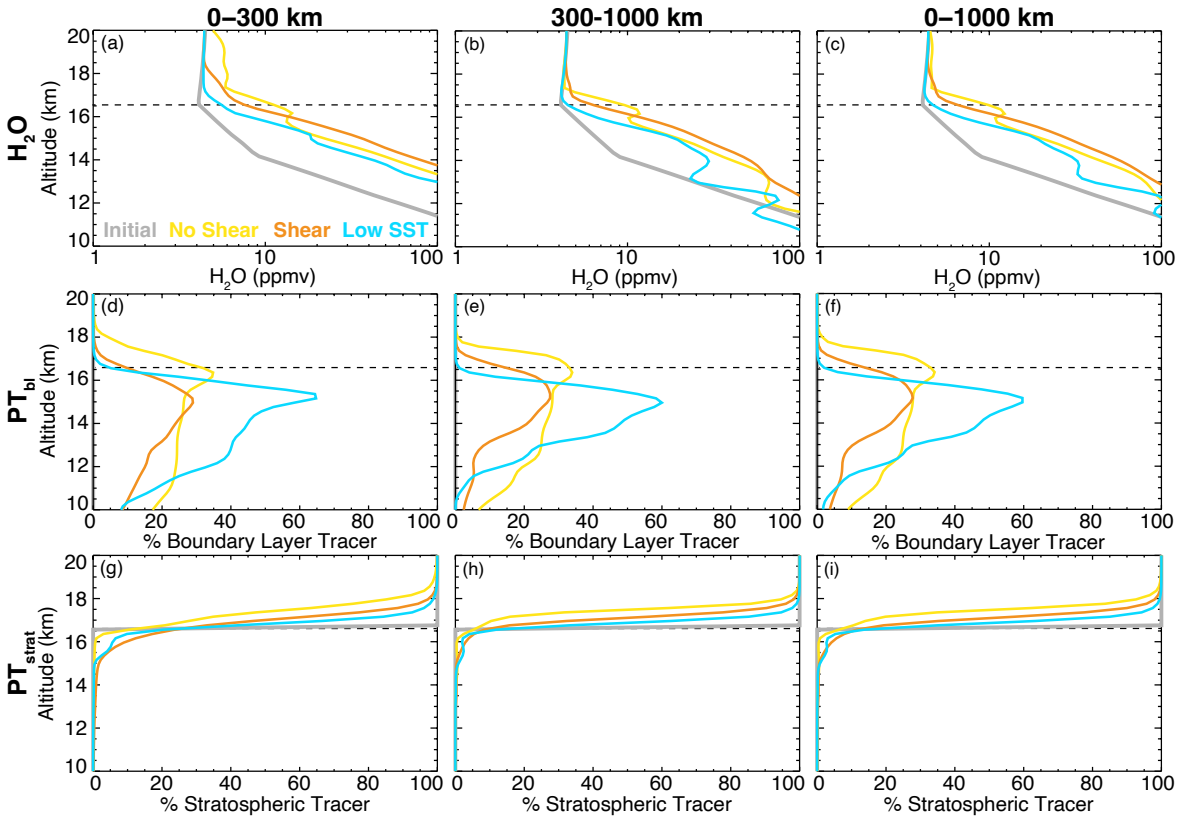


Figure 4.2: Average profiles of (top-to-bottom) H_2O, boundary layer passive tracer: PT_{bl}, and stratospheric passive tracer: PT_{strat} from (left-to-right) 0-300 km, 300-1000 km, and 0-1000 km. In each panel, the approximate tropopause altitude is shown by the dashed black line, initial model profiles are shown by the thick gray line, and remaining colored lines represent end-of-simulation averages for $TC_{noshear}$ (yellow), TC_{shear} (orange), and TC_{lowSST} (blue).

marily occur within intense eyewall convection in the simulation. Timeseries of the total number of overshoots within the domain and within 150 km of TC center are also examined (Fig. 4.3b). Overshoot frequency sharply increases starting near hour 90 of the simulation, when $TC_{noshear}$ reaches major hurricane status. The inner portion of the TC contains nearly all overshoots throughout the simulation, until the plateau stage beyond hour 160 (when the TC is a category 5), where overshoots are also found in the outer portion of the TC and generally decrease in frequency thereafter. It is not known whether the large variability in overshoot count (especially in the latter stages of the $TC_{noshear}$ simulation) is a reasonable depiction of a real TC, as prior observational work has not evaluated time evolution of overshooting in such detail.

Overshoot frequency is also examined in the TC_{shear} and TC_{lowSST} simulations. In TC_{shear}, overshoots are most common in the inner TC core (Fig. 4.3c), similar to $TC_{noshear}$. Specifically, overshoots are most frequent in the downshear left (northeast) quadrant. This TC-relative shift maxima in the TC_{shear} simulation is expected, as prior work has shown that convection in hurricanes exposed to deep-layer VWS matures downshear (Corbosiero and Molinari, 2002; Nugent and Rios-Berrios, 2018). Overshoot frequency sharply increases as the simulated TCs intensify. Accordingly, periods of rapid intensification (RI) for each simulation were identified and compared to overshoot frequency throughout time (Fig. 4.3b,d,f). For TC_{shear}, the number of overshoots peaks during RI, and then decreases when the TC is at its maximum intensity and approximately steady-state. This suggests that RI is important for overshoots in the TC_{shear} simulation. Meanwhile, overshooting in $TC_{noshear}$ appears to be less related to RI, as peak overshoots occur once major hurricane status is attained, and beyond.

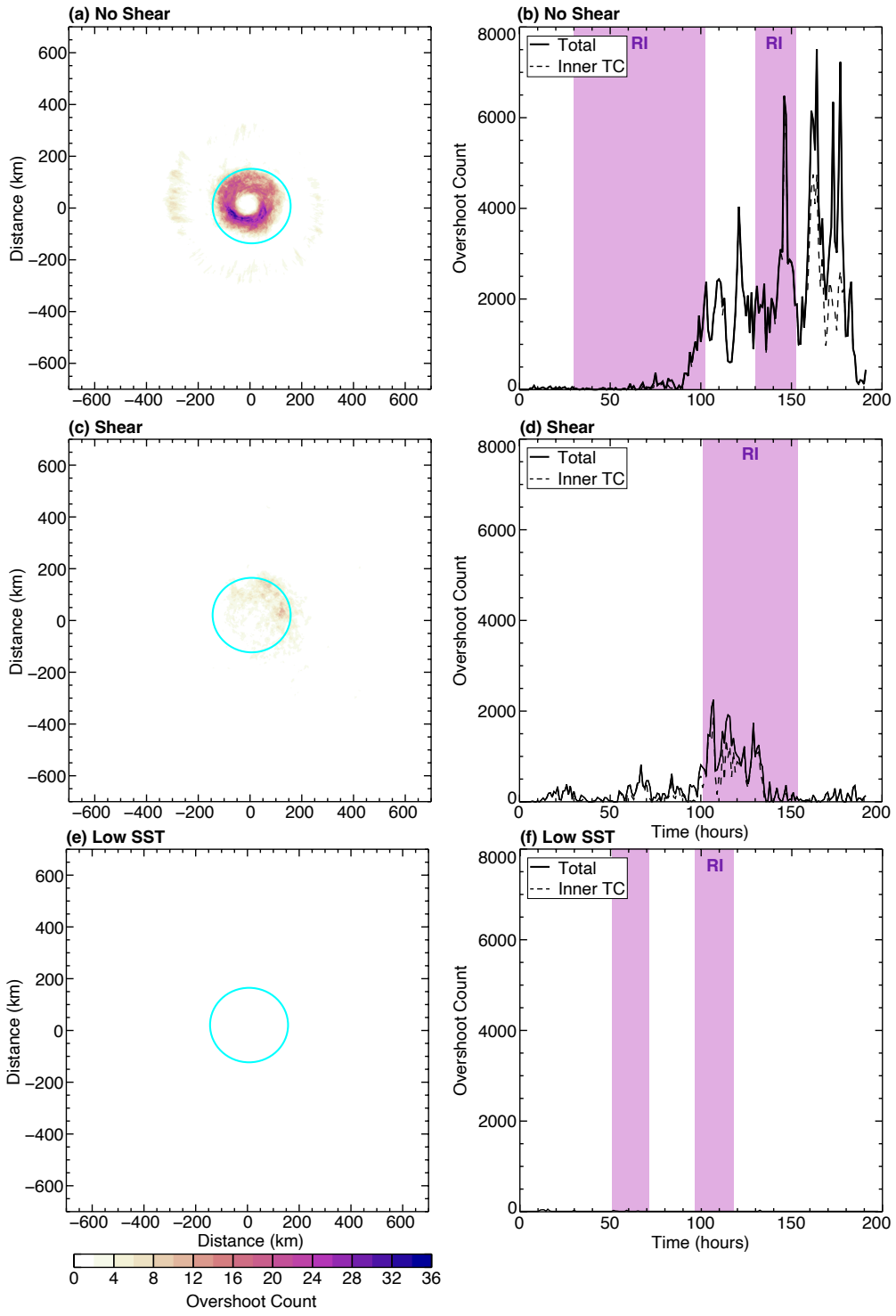


Figure 4.3: Overshoot count (cloud tops reaching or exceeding 17.56 km) (left) spatial distribution, and (right) timeseries for the total TC domain (solid line) and inner 150 km from TC center (dashed line) for $TC_{noshear}$ (a,b), TC_{shear} (c,d), and TC_{lowSST} (e,f). The inner 150 km of the TC is indicated by the cyan circle (a,c,e).

4.2.1 Processes Contributing to Exchange in Tropical Cyclones

The evolution of TC structure, TST (at an altitude of 17.56 km; ∼1 km above tropopause), and STT (at an altitude of 15.56 km; ∼1 km below tropopause) in $TC_{noshear}$ are examined with H_2O, PT_{bl}, PT_{strat}, and PT_{conv} in Fig. 4.4. Above the tropopause, several overshoots are seen with enhanced H_2O (Fig. 4.4a,e,i), PT_{bl} (Fig. 4.4b,f,j), and PT_{conv} (Fig. 4.4d,h,l) at each hour, suggesting that overshoots are contributing to TST within $TC_{noshear}$. The area of enhanced H_2O at 17.56 km is confined to the TC core and reaches approximately 18 ppmv (>3× background). PT_{bl} is less enhanced - maximizing at approximately 10% near overshoots and covering a greater area from TC center compared to H_2O (Figs. 4.4i and j). The increasing potential temperature of the maximum PT_{bl} enhancement over time suggests that the TC outflow altitude steadily increases. The evolution of PT_{conv} (Figs. 4.4d,h,l) shows similar character to H_2O at earlier times and to PT_{bl} at later times, well exceeding the spatial extent of H_2O enhancement.

In contrast, the evolution of $TC_{noshear}$ structure and cross tropopause transport of PT_{strat} ∼1 km below the tropopause shows that stratospheric air is transported downwards throughout the TC outflow, maximally (up to 10% enhancement) just outside of the TC core and within the eye and expanding radially outward over time (Fig. 4.4c,g,k). Subsidence within the eye is evidenced by extreme PT_{strat} values within a narrow distance from TC center (∼50 km) at all times. As the TC intensifies (Fig. 4.4c and g), there appears to be locally enhanced stratospheric air up to 4% near the TC outflow edge and overall downward transport extending to distances ∼1000 km from TC center. This suggests multiple processes are contributing to STT in for $TC_{noshear}$, including overshoots and subsidence within the eye, which will be discussed in greater detail in subsequent analysis.

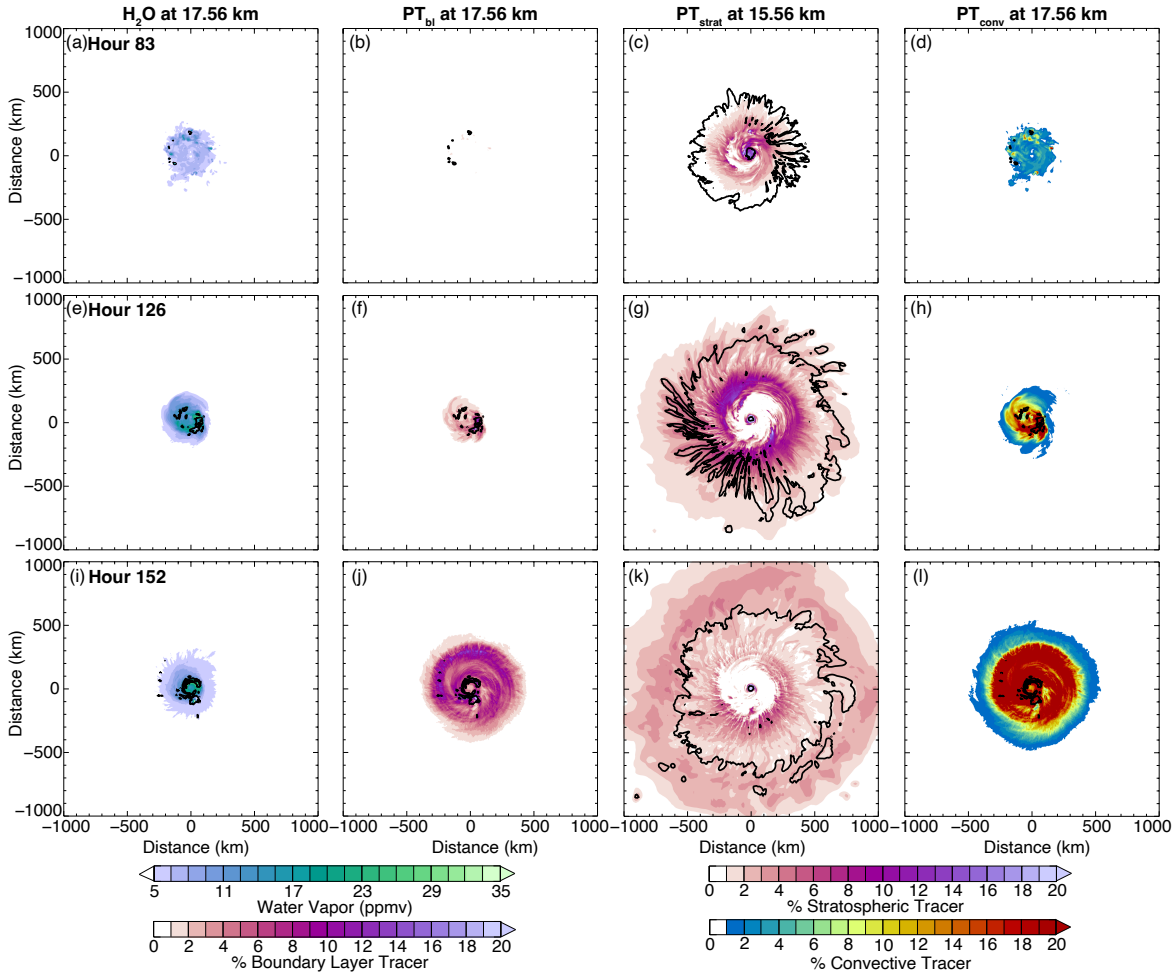


Figure 4.4: Constant-altitude TC-centered plots of $\mathrm{TC}_{noshear}$ of (left-to-right) H_2O at 17.56 km, boundary layer passive tracer (PT_{bl}) at 17.56 km, stratospheric passive tracer (PT_{strat}) at 15.56 km, and convective passive tracer (PT_{conv}) at 17.56 km for (top-to-bottom) hours 83, 126, and 152 of simulation time. The black contour outlines the cloud boundary (sum of cloud and ice mixing ratios is greater than 1.0×10^{-6} kg kg^{-1}).

4.2.1.1 Troposphere-to-Stratosphere Transport

To determine the extent and evolution of UTLS hydration in $TC_{noshear}$, varied examination of H_2O in space and time is provided (Fig. 4.5). A space-time diagram (Fig. 4.5a) shows that H_2O enhancements at 17.50 km (approximately 1 km above the initial tropopause) emerge early and become more prominent when the TC can be classified as a major hurricane. The spatial extent of H_2O enhancement exceeding 6 ppmv remains $\leq$220 km from TC center throughout the simulation, with the strongest H_2O enhancements located $\leq$100 km from TC center, especially after hour 120. Periodic fluctuations in the spatial extent of H_2O and magnitude of H_2O enhancement are seen about every 12 hours during TC intensification periods as a major hurricane, which is likely a result of convective development cycles within the TC. The extreme H_2O enhancements become further confined to $\sim$50 km from TC center near and following when the TC intensity begins to plateau. The H_2O curtains in Figs. 4.5b-d show H_2O enhancement up to 17 ppmv at an altitude of 18 km. By hour 106, the H_2O enhancement begins to reach altitudes higher than 18 km and distances 50-150 km from TC center, and the shape of the stratospheric H_2O enhancement resembles a "bottleneck" with enhancement confined to smaller distances from TC center near the tropopause. A seemingly drier layer emerges between 15 and 16 km by the end of the simulation.

Vertical cross-sections through TC center in $TC_{noshear}$ demonstrate that overshooting convection contributes substantially to stratospheric enhancements in H_2O, as Figs. 4.6a and b show coincident overshooting tops and H_2O extremes as high as $\sim$20 ppmv extending to altitudes near 19 km. Weaker overshoots are seen at later times (Figs. 4.6c and d). This analysis suggests that overshoots in eyewall convection are a dominant stratospheric hydration process within TCs. Figure 4.6 also reveals prevalent gravity waves near/within the overshoots that likely contribute to STE, as indicated

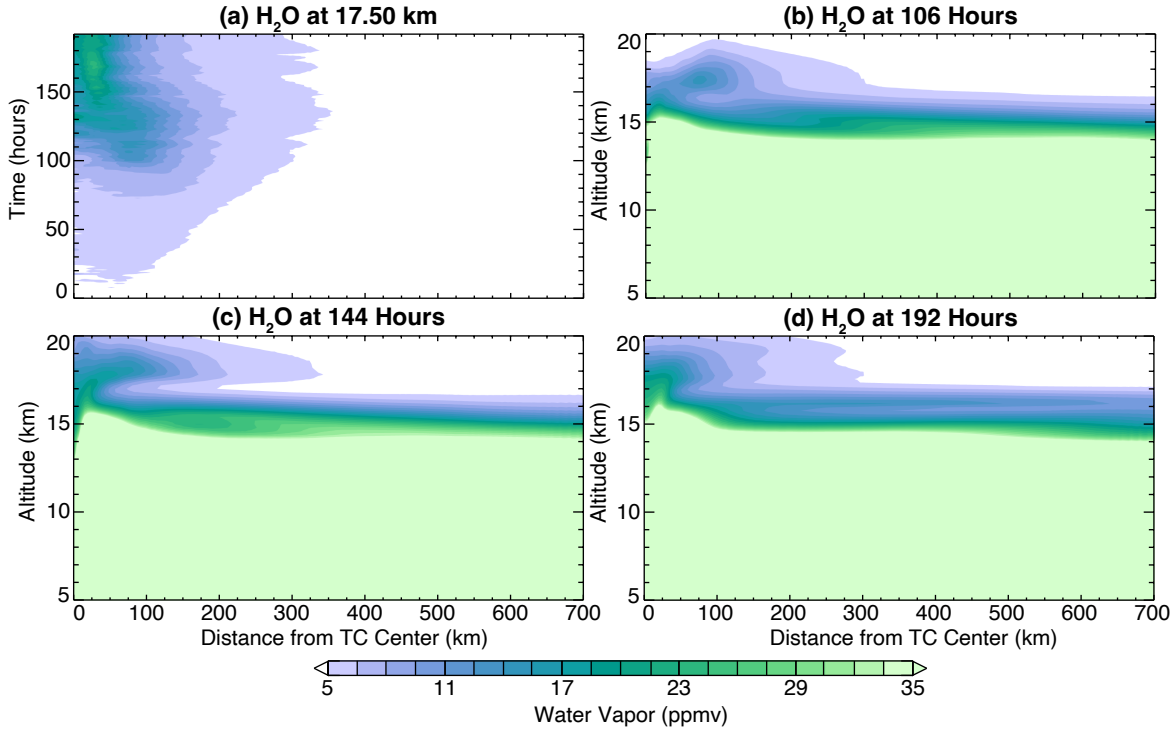


Figure 4.5: For H_2O in $TC_{noshear}$, (a) space-time diagram at an altitude of 17.50 km, in coordinates of distance from TC center and simulation time, and (b-d) storm-average curtains of H_2O in distance from TC center and altitude at hours 106, 144, and 192, respectively. Storm averaging occurs in 4-km radial bins over all 360 degrees of the TC.

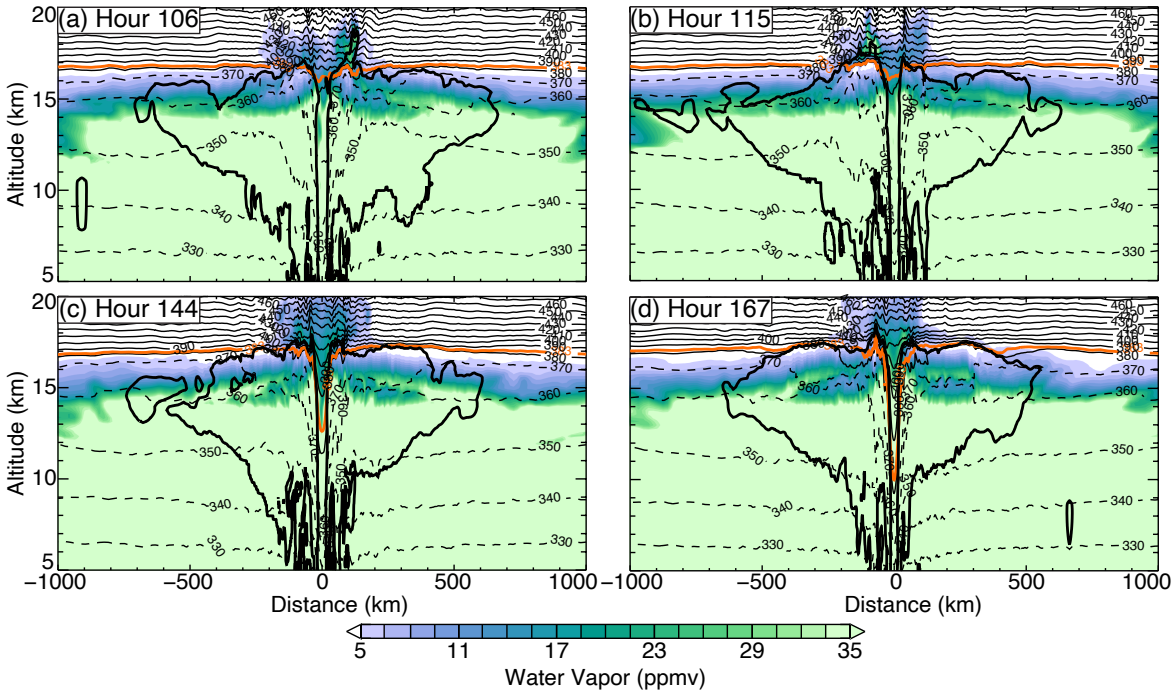


Figure 4.6: Vertical cross-sections of water vapor (H_2O; ppmv) in $TC_{noshear}$ at hour 106 (a), 115 (b), 144 (c) and 167 (d). Potential temperature contours are shown in black in each panel in 10 K intervals (with solid contours for 380 K and above, and dashed below). The orange contour shown in each panel is the potential temperature of the environmental tropopause (383 K).The cross-section is taken through the meridional center of the TC, going from west to east.

by the altitude variability of stratospheric isentropes near TC center in for $TC_{noshear}$. In all times shown in Fig. 4.6, the enhanced H_2O remains near the inner TC, as seen previously in the space-time diagrams. The previously-diagnosed less-hydrated 15-16 km altitude layer becomes increasingly evident throughout the simulation, spanning distances of ∼100–300 km from TC center. Due to the lack of enhanced H_2O present within the cloud boundary and near cloud top, there is likely a high concentration of ice present there. These less hydrated portions of the TC agree with previous work, where the upper troposphere and tropopause become dehydrated compared to its surrounding environment (Jiang et al., 2020; Allison et al., 2018).

To consider physical constraints on the limited spatial extent and bottleneck shape

of enhanced H_2O along with the drier layer that emerges within the TC outflow in $TC_{noshear}$, temperature anomalies throughout the TC simulation are explored (Fig. 4.7). Temperature anomalies are calculated as the difference between the temperature at each simulation time and the initial temperature at each altitude. A space-time diagram (Fig. 4.7a) of temperature anomalies at 17.00 km (∼0.5 km above tropopause) shows that the inner ∼50 km of the TC exhibits increasingly positive values, which is expected due to its warm core. Beyond 50 km, temperatures at 17 km decrease with time. Looking at temperature anomaly structure with altitude (Figs. 4.7b-d), a cool layer exists early near 16 km altitude, becomes more pronounced over time, and rises to a central altitude of ∼17 km. This layer coincides with the dry layer occurring near cloud top across the TC outflow seen in Figs. 4.5 and 4.6 and is coincident with the narrow TC-relative element of the stratospheric bottleneck feature. At later times, a secondary, weaker cool layer emerges near 19-20 km altitude and a third weak cool layer emerges near 15-16 km. This third layer coincides with the dry layer seen in Figs. 4.5 and 4.6 and is seemingly connected with the convective outflow of the TC, specifically its deepening and intensification with time.

Temperature profiles 50 km, 100 km, and 200 km from TC center similarly reveal the emergence of the three cold layers in (Fig. 4.8). By the end of the $TC_{noshear}$ simulation (Fig. 4.8d), all 3 cold layers are distinguishable. The structure of these temperature profiles is similar to those seen with RO data in TCs (Rivoire et al., 2016; Biondi et al., 2015, 2013). The cold anomalies seen in Figs. 4.7 and 4.8 suggest a saturation-limited environment, where the low temperatures restrict the amount of H_2O that can exist in air at equilibrium. This environment effectively acts as a "cold trap" and would prevent H_2O from being transported to the stratosphere at greater distances from TC center, thus reinforcing spatially-confined H_2O enhancements throughout the TC simulation. This characteristic also provides a possible explanation for the bottleneck H_2O shape

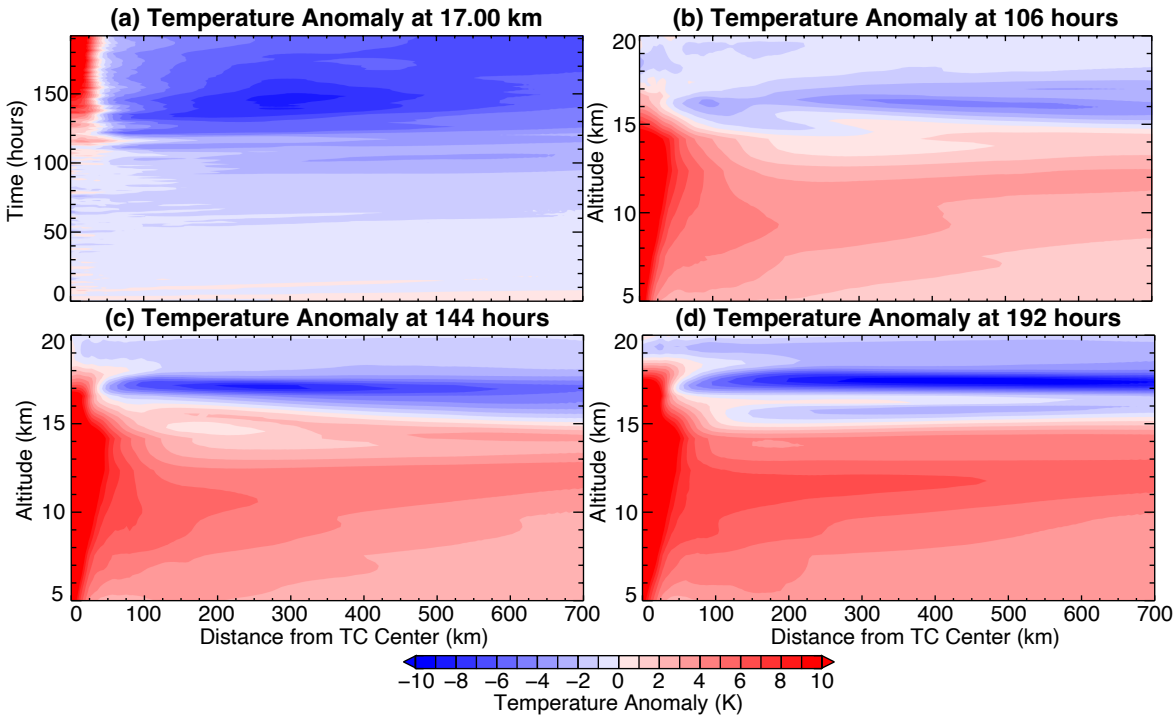


Figure 4.7: As in Figure 4.5, but for temperature anomalies in $TC_{noshear}$.

seen in Fig. 4.5 and the differences in spatial extent of H_2O and PT_{bl} seen in Fig. 4.4. As no radiation effects are included in the TC simulation, these temperature anomalies must arise due to TC dynamics, such as adiabatic cooling from convective ascent, rather than TC cloud-top cooling by radiation. The contribution to cooling from convective ascent supports similar arguments in previous work that cloud-top radiative effects are unable to account for such rapidly introduced low temperatures near the tropopause.

To understand why convective air within the TC in $TC_{noshear}$ is not as spatially limited as H_2O, vertical cross-sections of convectively influenced air (PT_{conv}; Fig. 4.9) and its spatial extent at an altitude of 17.56 km (Figs. 4.4d,h,l) are examined. The cross sections show that convectively influenced air exists within and in proximity to overshoots near the TC core, similar to that seen for H_2O (Fig. 4.6). However, while stratospheric H_2O enhancements are largely confined to the inner 220 km of the TC (Fig. 4.4a, e, i), convective air reaches 20% near 300 km from TC center at altitudes

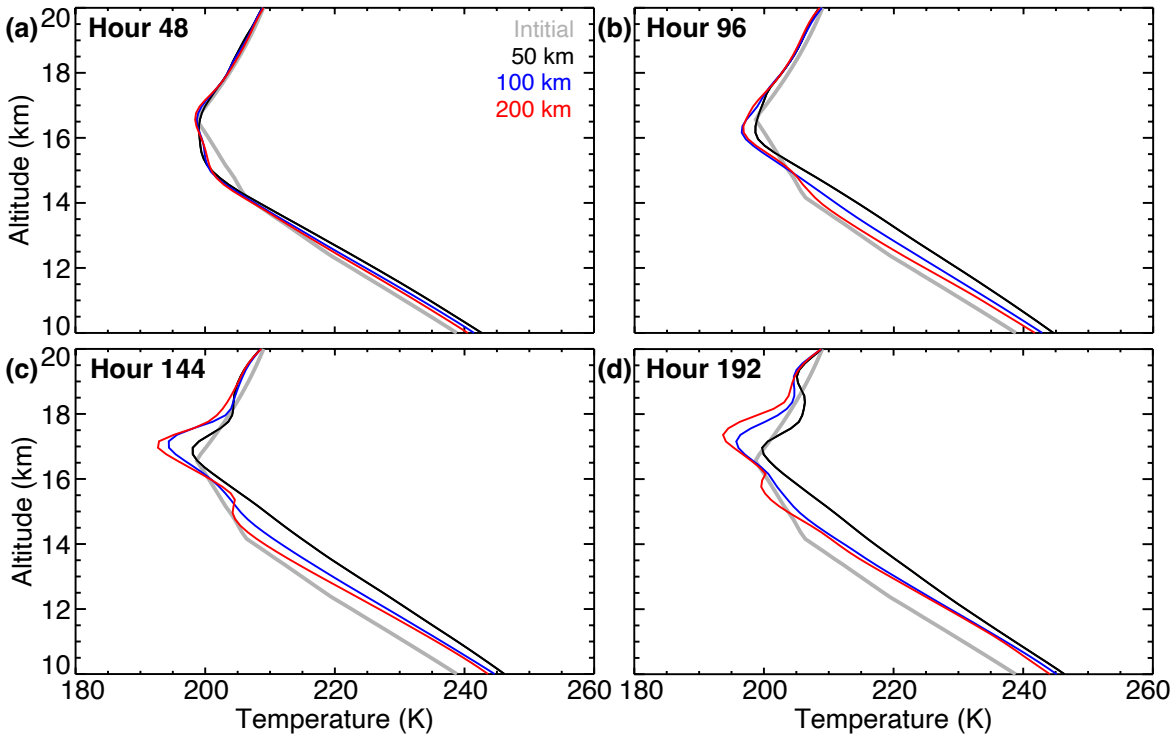


Figure 4.8: Vertical temperature profiles in $TC_{noshear}$ at distances from TC center of 50 km (red), 100 km (blue) and 200 km (black) for hour 48 (a), 96 (b), 144 (c), and 192 (d). The initial TC temperature profile is shown in gray in all panels.

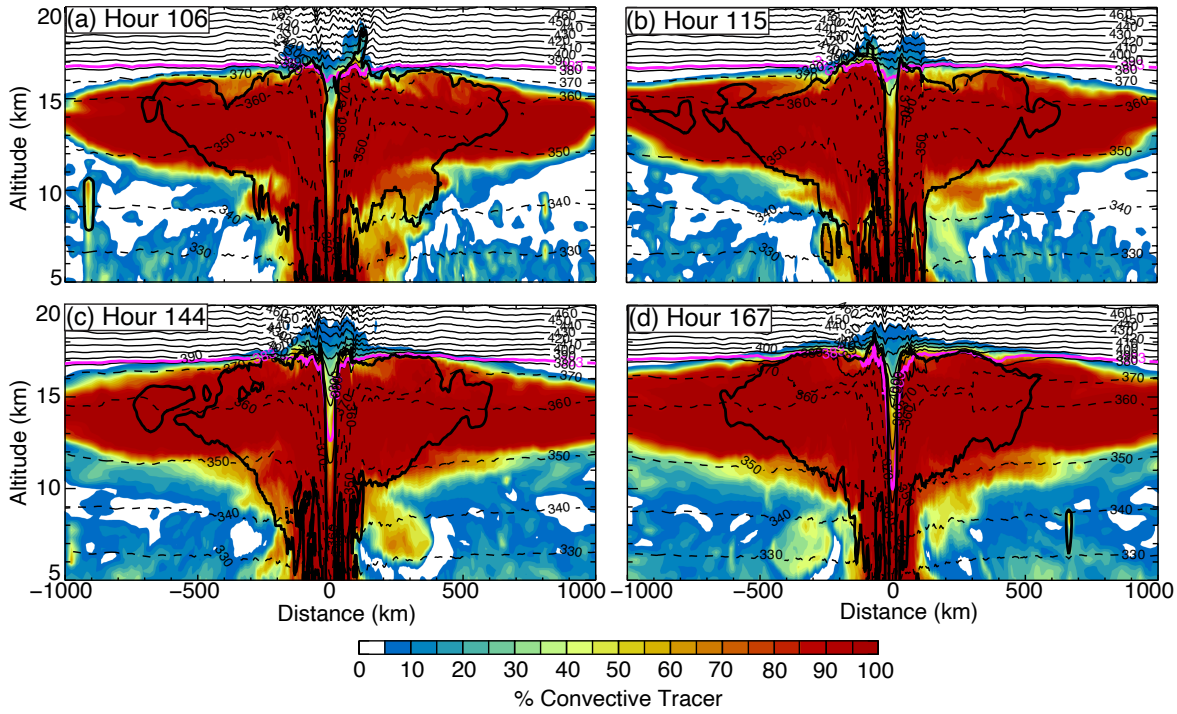


Figure 4.9: As in Fig. 4.6, but for the percentage of convective passive tracer (PT_{conv}) in $TC_{noshear}$.

up to 1 km above tropopause (Fig. 4.4d, h, l). These differences in the spatial extent of PT_{conv} and H_2O reinforce that the limited spatial extent of H_2O in the stratosphere is due to a saturation-limited environment, rather than a lack of convective influence.

Figure 4.10 includes a space-time diagram of boundary layer air (PT_{bl}) at an altitude of 17 km (∼0.5 km above the initial tropopause; Fig. 4.10a) and radius-altitude curtains at several times (Figs. 4.10b-d) in $TC_{noshear}$. There seems to be minimal TST until the TC develops into a major hurricane, where PT_{bl} enhancement reaches ∼10% at 17 km and further increases in magnitude and spatial extent during the remainder of the simulation. PT_{bl} experiences the greatest enhancement in magnitude and depth near the TC core, and the maximum outflow altitude increases in an absolute sense about 1 km over time. The maximum altitude of PT_{bl} enhancement overall reaches about 18 km (≥1% enhancement), which is a lower maximum altitude than H_2O. This indicates

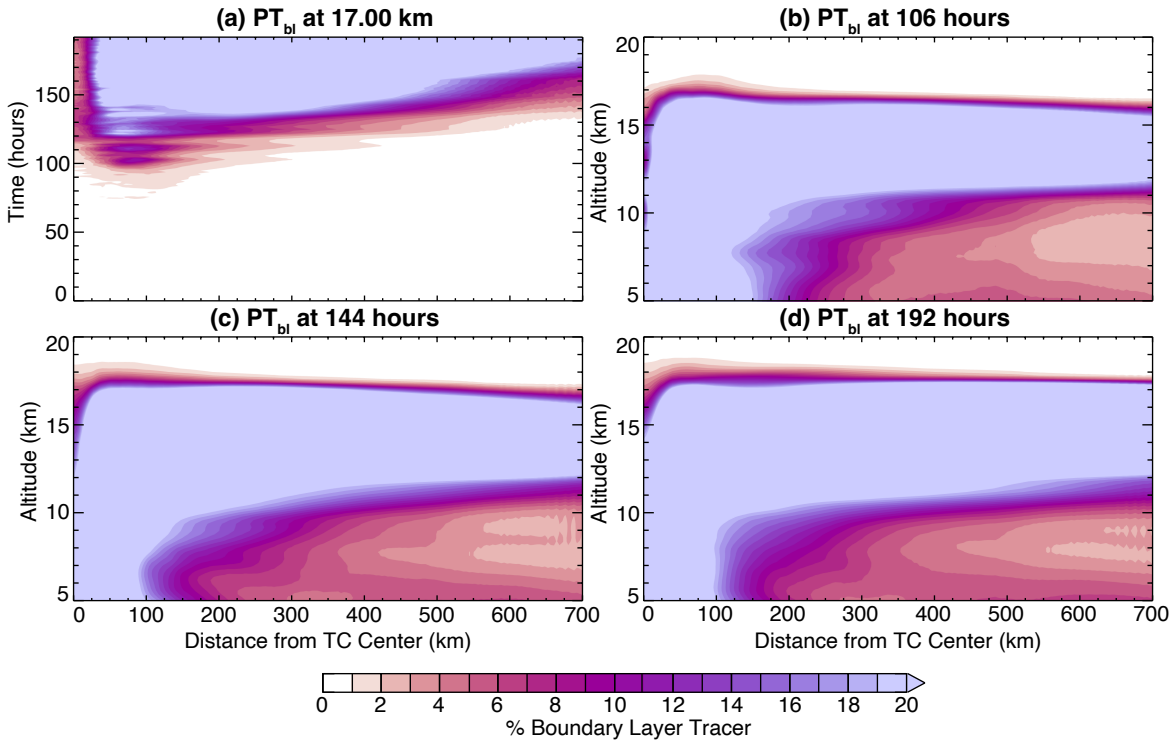


Figure 4.10: As in Figure 4.5, but for the percentage of boundary layer passive tracer (PT_{bl}) in $TC_{noshear}$.

that H_2O reaches higher altitudes than boundary layer air as seen in Fig. 4.14, which has been similarly found in simulations of mid-latitude convection (Homeyer, 2015; Phoenix and Homeyer, 2021; Gordon and Homeyer, 2022) and is likely due to the fact that H_2O can be transported both through air mass transport and the lofting and sublimation of cloud ice (Chapter 3).

Cross-sections of PT_{bl} (Fig. **??**) in $TC_{noshear}$ show that overshoots facilitate cross-tropopause transport of boundary layer air, but again not as prevalent as that for H_2O and PT_{conv}. It is likely that PT_{bl} is more efficiently transported isentropically since it is not constrained by temperature. This is supported by the distribution of enhanced PT_{bl} near the inner TC core throughout the evolution in the cross sections of Fig. 4.11, as it appears to accumulate and expand radially outward in the stratosphere along near-tropopause isentropes.

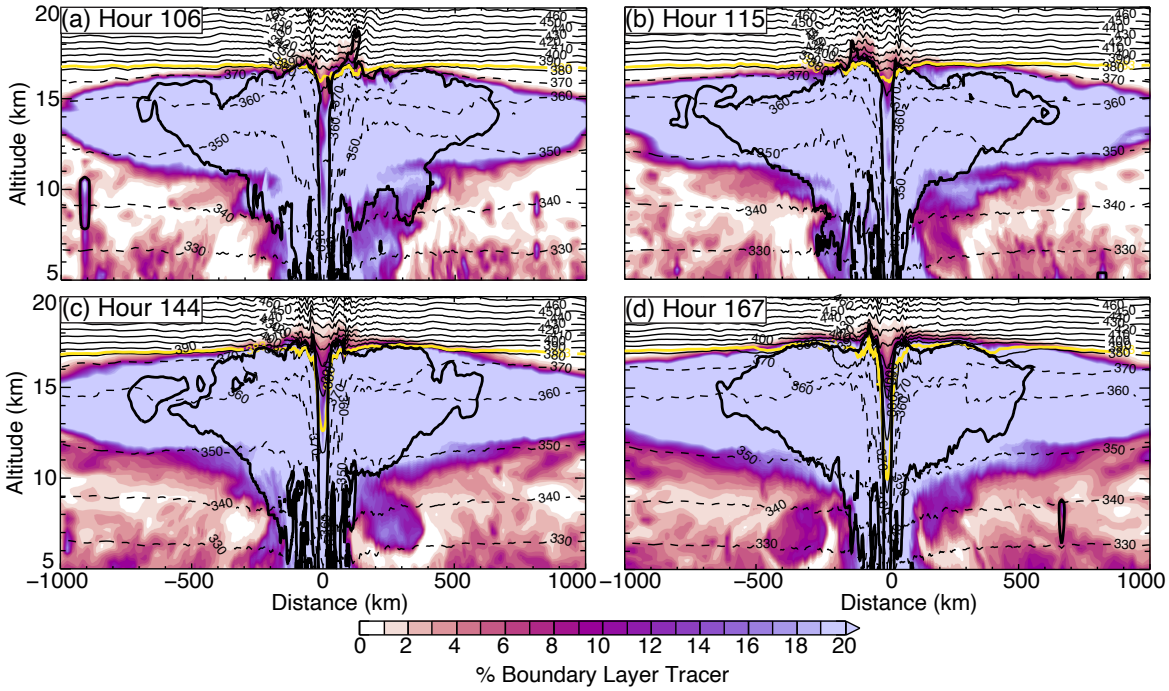


Figure 4.11: As in Figure 4.6, but for the percentage of boundary layer passive tracer (PT_{bl}) in $TC_{noshear}$.

4.2.1.2 Stratosphere-to-Troposphere Transport

STT in $TC_{noshear}$ is assessed using PT_{strat}. Figure 4.12 shows a space-time diagram of PT_{strat} at an altitude of 15.5 km (∼1.1 km below the initial tropopause) and PT_{strat} radius-altitude curtains. The space-time diagram (Fig. 4.12a) shows that downward transport of PT_{strat} begins early in the simulation, and becomes more prominent near and following becoming a Category 2 hurricane. STT is largest within the eye (inner ∼50 km) of the TC throughout the simulation with PT_{strat} increasing by 10% at altitudes as low as 7 km, and deepening over time. Beyond the deep subsidence within the eye, the spatial extent of STT increases with time, reaching outwards of 700 km. From hours 90–130, there are enhanced features of PT_{strat} spanning 100–400 km from TC center, suggesting the importance of additional transport processes. Outside of the eye, PT_{strat} reaches altitudes as low as ∼14.75 km, with the largest below-tropopause

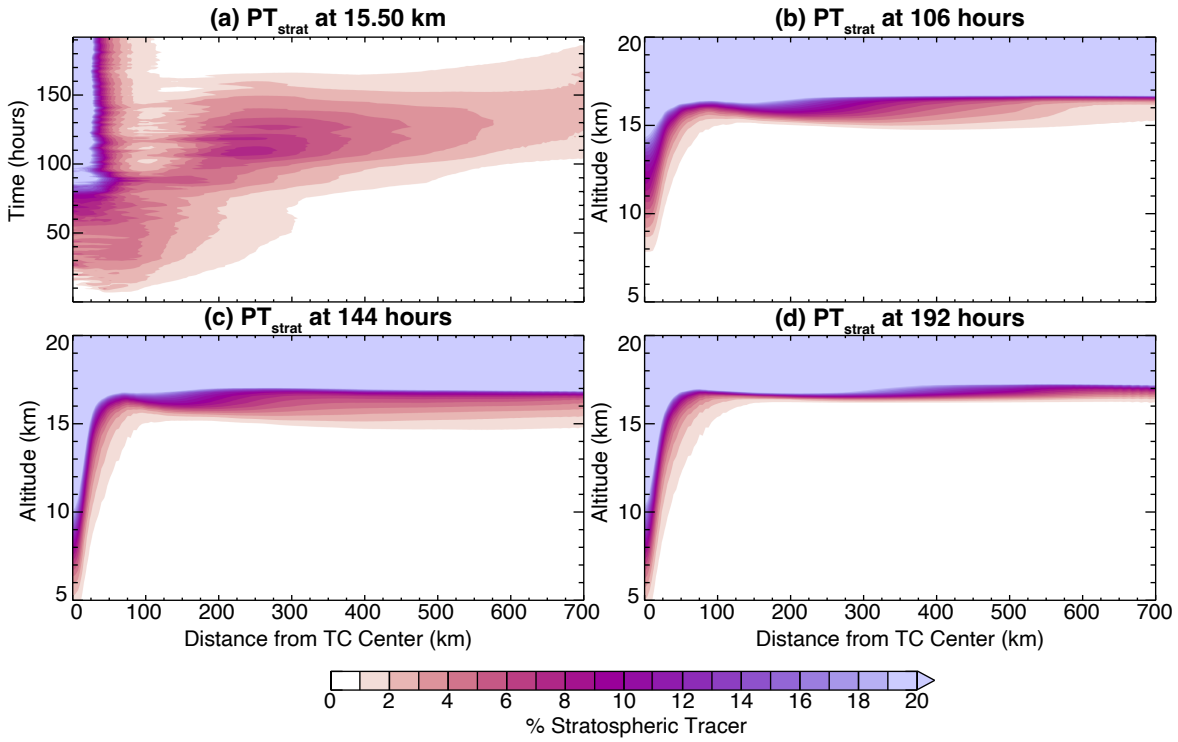


Figure 4.12: As in Figure 4.5, but for the percentage of stratosphere passive tracer (PT_{strat}; stratospheric air) in $TC_{noshear}$.

enhancements in PT_{strat} near the inner TC and weakening as distance from TC center increases (Figs. 4.12b, c). By the end of the simulation, this below-tropopause enhancement of PT_{strat} is broadly reduced, with merely a slight, shallow enhancement at distances greater than 500 km from TC center (Fig. 4.12d).

Cross-sections of PT_{strat} (Fig. 4.13) help reveal the multiple processes influencing STT in $TC_{noshear}$. Specifically, it is again clear that STT primarily occurs via subsidence in the eye and throughout tropopause-level outflow. Subsidence within the eye has the greatest vertical extent. Downward transport of PT_{strat} throughout the tropopause-level outflow of the TC appears to result primarily from overshooting eyewall convection and subsequent mixing and mostly isentropic advection to greater distances from TC center. Figure 4.4 shows transverse banding-like cloud and PT_{strat} structures (panel g) which has been previously linked to turbulence in TCs (Lenz et al.,

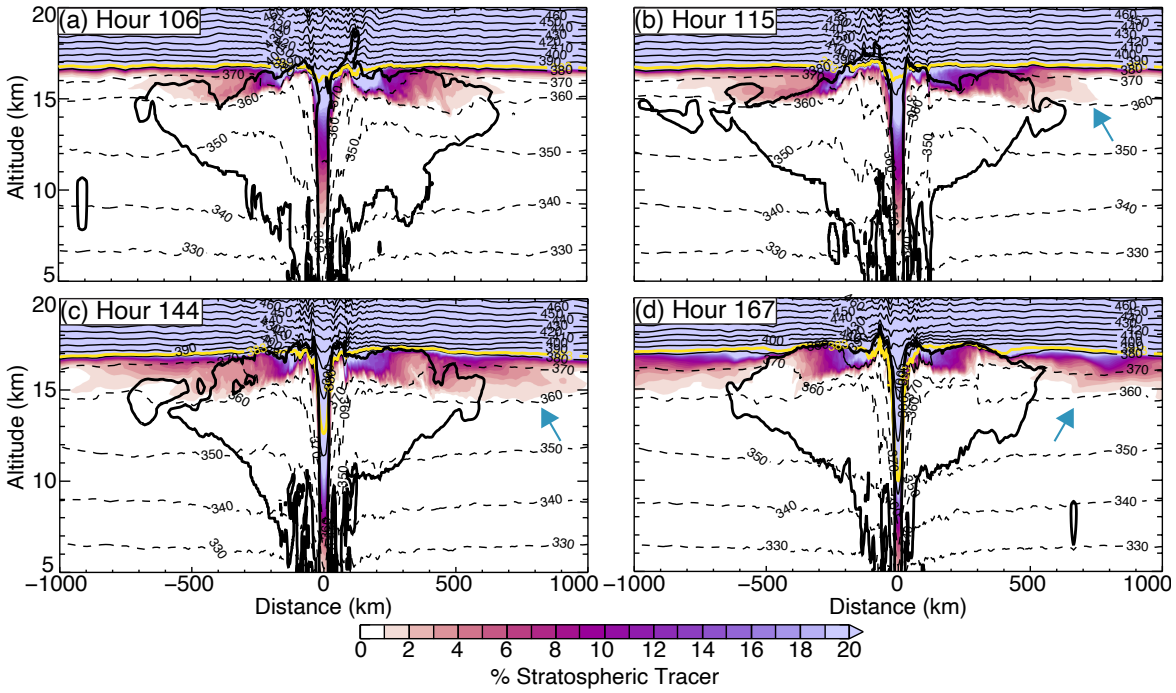


Figure 4.13: As in Figure 4.6, but for the percentage of stratosphere passive tracer (PT_{strat}) in $TC_{noshear}$. Blue arrows indicate the local maxima of stratospheric air advected radially outward from the TC.

2009). Examining eddy viscosity (not shown) suggests that turbulence is associated with the filaments of enhanced PT_{strat} air in these features, although it does not seem to be the sole contributor. Transport throughout the tropopause-level outflow reaches a maximum of 10% PT_{strat} air at 15 km. This suggests that subsidence within the eye leads to deeper STT within a TC, but STT throughout the tropopause-level outflow has a greater spatial extent.

The snapshots in Fig. 4.13 show a filament of enhanced PT_{strat} at the TC outflow edge in $TC_{noshear}$ which propagates radially outward from TC center over time. This outward propagation and emergence from the TC cloud boundary is also seen in the maps of Figs. 4.4g and 4.4k. This is further supported by the temperature profiles shown in Fig. 4.8, as the cool layer and PT_{bl} maximum that develop near 15 km increase in altitude over time, suggesting they are associated with deepening and strengthening

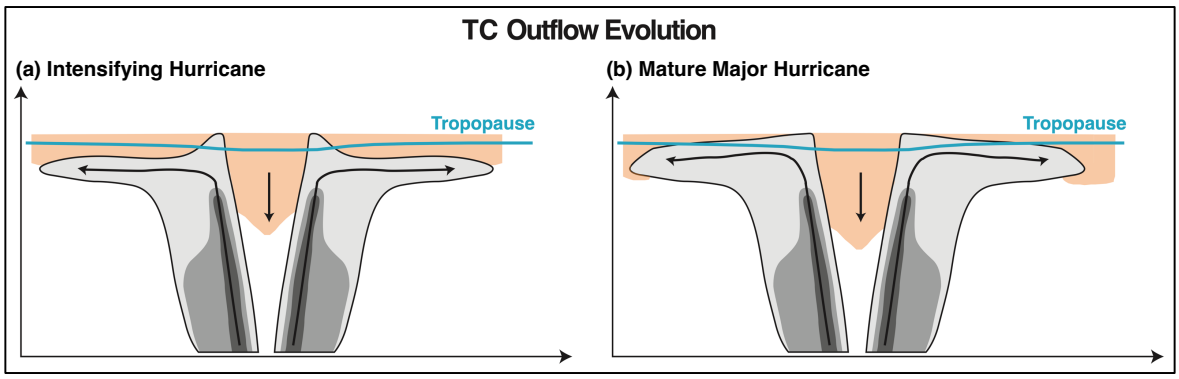


Figure 4.14: Illustration of the evolution of TC convective outflow in $TC_{noshear}$ from (a) an intensifying hurricane and to (b) a mature major hurricane, and its impact on downward transport of stratospheric air. Notable aspects of the outflow evolution include the secondary circulation deepening and strengthening as the storm intensifies, resulting in the eyewall convection and outflow impinging upon the tropopause.

convective outflow, which is summarized in the schematic shown in Fig. 4.14. Earlier development (Fig. 4.14a) as a weaker but intensifying hurricane is characterized by near-tropopause PT_{strat} enhancement from stirring by frequent overshooting. As the storm intensifies and deepens to become a mature major hurricane (Fig. 4.14b), the secondary circulation deepens and strengthens, eyewall convection and outflow impinge upon the tropopause, and PT_{strat} enhancement from previous STT is advected radially outward and replaced by lofted lower troposphere air. The presence of stratospheric air near the outflow edge after being advected radially outward results in an apparent O_3 wrapping feature, due to the stratospheric air location coinciding with where one would expect it to be after wrapping. Thus, rather than local downward transport, the radial outward advection of stratospheric air outside the TC outflow in the upper troposphere may be the cause behind previously documented "wrapping" cases, such as those discussed in Baray et al. (1999) and De Bellevue et al. (2006).

4.2.2 Transport Sensitivity to Intensity

STE sensitivity to TC intensity is investigated using TC_{lowSST} and comparing to the preceding analysis of $TC_{noshear}$. Given that TC_{lowSST} has a lower initial SST than $TC_{noshear}$ (27^oC versus 29^oC) it will have a weaker maximum intensity (as demonstrated in Fig. 4.1). To examine TST and STT in TC_{lowSST}, cross sections of H_2O, PT_{bl}, PT_{strat}, and PT_{conv} at a Category 2 and 4 hurricane intensity are shown in Figure 4.15. Enhanced H_2O reaches an altitude of approximately 17.5 km, extending up to 100 km away from TC center during the simulation. There are overshooting tops (relative to the broader TC cloud top) present in both the inner TC core and outer TC (Fig. 4.15a) that lead to enhanced H_2O. However, since the outflow is about 2 km below the tropopause, these overshoots do not penetrate the tropopause, are not counted as overshoots in Fig. 2.3, and therefore lead to less stratospheric hydration.

Increased H_2O near the inner TC core resulting from overshoots is similar to the result in $TC_{noshear}$. However, the limited radial extent of enhanced H_2O in $TC_{noshear}$ is due to low temperatures and a saturation-limited environment that acts as a "cold trap", as shown in Figs. 4.5 and 4.7, and H_2O, PT_{bl}, and PT_{conv} spatial differences in Fig. 4.4. In TC_{lowSST}, there is minimal transport to the stratosphere of PT_{bl}, as it is maximized at the primary outflow level where it reaches near 1000 km from TC center (Figs. 4.15c,d). Comparing H_2O and PT_{conv} for TC_{lowSST} reveals that they have similar spatial extents, and that H_2O reaches a higher altitude than PT_{conv} (Figs. 4.15a,b,g,h). This suggests the limited spatial extent of H_2O is not due to temperature constraints, but rather the convectively influenced air simply does that reach that high of an altitude in this case.

For STT, there is minimal transport of PT_{strat} when TC_{lowSST} is a Category 2 hurricane, which is not surprising given that the TC outflow does not impinge upon

the tropopause (Fig. 4.15e). When TC_{lowSST} reaches a Category 4 hurricane intensity, there is downward transport in the eye and along the TC outflow (Fig. 4.15f), similar to $TC_{noshear}$. One notable difference is the filament-like shape of the stratospheric air along the outflow in TC_{lowSST}. This is likely a result of TC_{lowSST} not impinging on the tropopause, and therefore the stratospheric air is not getting replaced by outflow air as it does in $TC_{noshear}$ (Figs. 4.13 and 4.14). The radially-outward extending filamentary structure of stratospheric air below the tropopause results from mixing and stirring by tropopause-nearing eyewall convection and subsequent advection by the outflow rather than wrapping. However, it does resemble the two-layer stratospheric air signatures identified in previous balloon profiles, outlined in Baray et al. (1999) and De Bellevue et al. (2006), which sample from storms with Category 4 hurricane intensity. Overall, this suggests that the proximity of outflow to the tropopause altitude is critical to determining the impact of overshooting tops on transport, and therefore stratospheric hydration, and STT associated with TCs.

4.2.3 Transport Sensitivity to Deep-Layer Shear

Deep-layer environmental VWS is known to impact the distribution of convection in a TC, but it is unknown if these asymmetries persist in the stratosphere and how they impact STE. Thus STE sensitivity to VWS is investigated using TC_{shear} and comparing to $TC_{noshear}$. Cross-sections of H_2O for $TC_{noshear}$ and TC_{shear} at Category 4 hurricane intensity are shown in Fig. 4.16–similar wind speeds are chosen to provide an accurate comparison between the simulations. Stratospheric hydration in TC_{shear} reaches $\approx$10 ppmv at an altitude of 18.5 km, and extends outwards of 800 km downshear of the TC (Fig. 4.16b). Overshooting tops in the inner TC are the primary source of enhanced H_2O in TC_{shear}, similar to $TC_{noshear}$. The altitude and magnitude of enhanced H_2O is greater in $TC_{noshear}$, but the spatial extent (at least on the downstream side) is greater

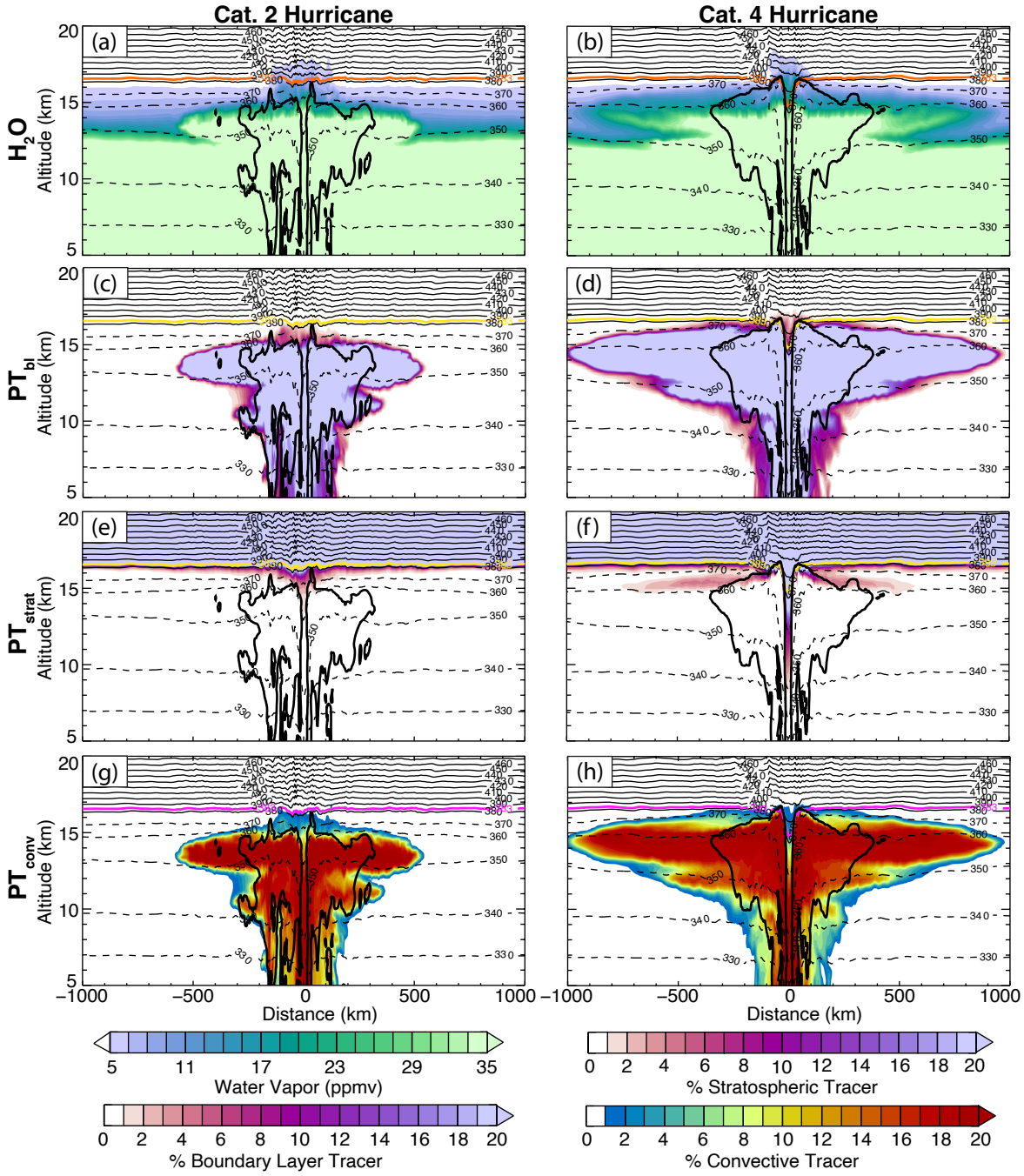


Figure 4.15: Vertical cross-sections of TC_{lowSST} taken from west to east through the meridional center of the TC. These include (H_2O; ppmv, (a,b)), percentage of boundary layer passive tracer (PT_{bl} (c,d)), percentage of stratospheric passive tracer (PT_{strat} (e,f)), and percentage of convective passive tracer (PT_{conv} (g,h)) at Category 2 (left) and 4 (right) hurricane intensity, respectively. Potential temperature contours are shown in black in each panel in 10-K intervals (with solid contours for 380 K and above, and dashed below). The orange, yellow, or pink contour shown in each panel is the potential temperature of the environmental tropopause (383 K).

for $TC_{noshear}$.

To explore differences in the spatial extent of stratospheric hydration, temperature anomalies for $TC_{noshear}$ and TC_{shear} are shown in Fig. 4.17, once again at Category 4 hurricane intensity. Low temperatures were shown to be an important constraint for the spatial extent of enhanced H_2O in the $TC_{noshear}$ (Figs. 4.5, 4.7), but the cooling near the tropopause for TC_{shear} is not as strong and does not extend as close to TC center. The differences in near tropopause cooling and asymmetries in storm structure for TC_{shear} likely contribute to the stratospheric H_2O enhancement having a greater spatial extent downshear.

To further explore asymmetries in STE resulting from VWS, space-time diagrams of H_2O at 17.5 km ($\sim$1 km above tropopause) within each shear-relative quadrant of TC_{shear} are shown in Fig. 4.18. Overall, this further demonstrates stratospheric hydration is greatest downshear of the TC, especially in the downshear left quadrant of the TC. Overshooting tops were also most frequent in the downshear left quadrant (Fig. 4.18). The asymmetries of transported boundary layer air at 17.0 km ($\sim$0.5 km above the tropopause) are shown in Fig. 2.4. PT_{bl} is increased downshear of the TC, and the maximum enhancement of PT_{bl} occurs in the downshear right quadrant (Fig. 2.4d). The TST of H_2O and PT_{bl} in TC_{shear} reveals that the asymmetries in a sheared TC, where convection is recognized to be most intense downshear, persist into the stratosphere and impact STE.

The evolution of downward transport of PT_{strat} for $TC_{noshear}$ (Category 3 and 5 hurricane) and TC_{shear} (Category 2 and 4 hurricane) at 15.56 km ($\sim$1 km above tropopause) is shown in Fig. 4.20. STT in TC_{shear} occurs via subsidence in the eye and through mixing and stirring across the outflow near the tropopause, similar to $TC_{noshear}$. There is also no apparent wrapping in TC_{shear}. Rather, filaments of stratospheric air are transported down to the troposphere (Fig. 4.20c) and then become

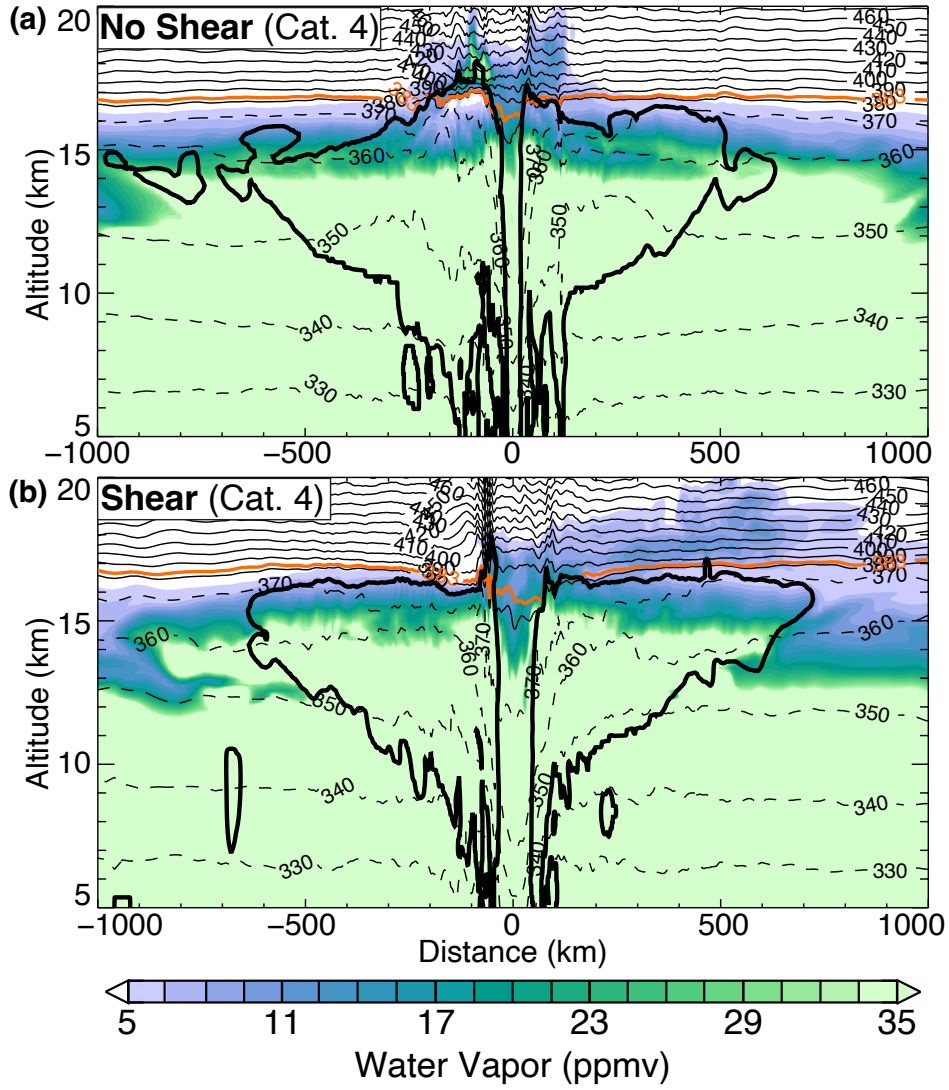


Figure 4.16: Vertical cross-sections of water vapor (H_2O; ppmv) category 4 hurricane intensity for $TC_{noshear}$ (a; hour 115) and TC_{shear} (b; hour 155). Potential temperature contours are shown in black in each panel in 10-K intervals (with solid contours for 380 K and above, and dashed below). The orange contour shown in each panel is the potential temperature of the environmental tropopause (383 K).The cross-section is taken from west to east through the meridional center of the TC.

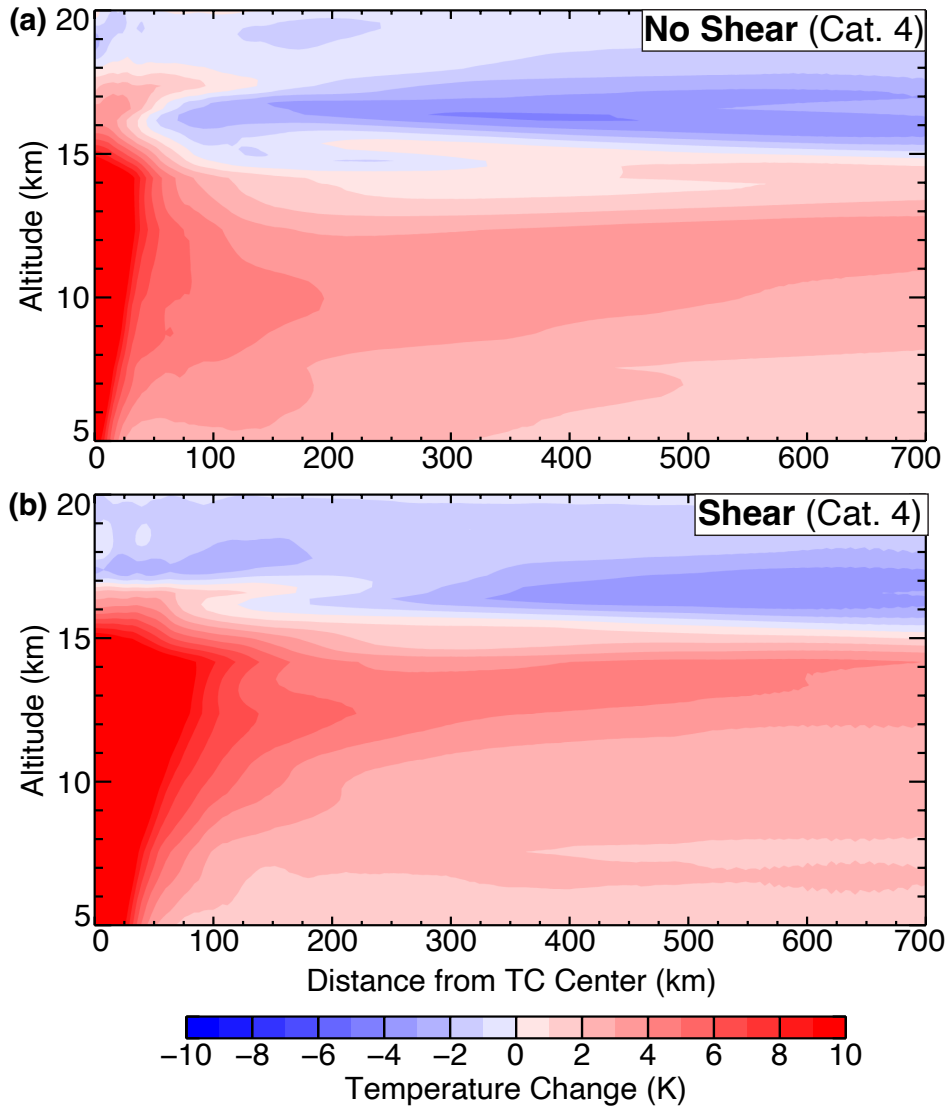


Figure 4.17: Storm-average curtains of temperature anomalies in distance from TC center and altitude at Category 4 hurricane intensity for $TC_{noshear}$ (a) and TC_{shear} (b). Storm averaging occurs in 4-km radial bins over all 360 degrees of the TC.

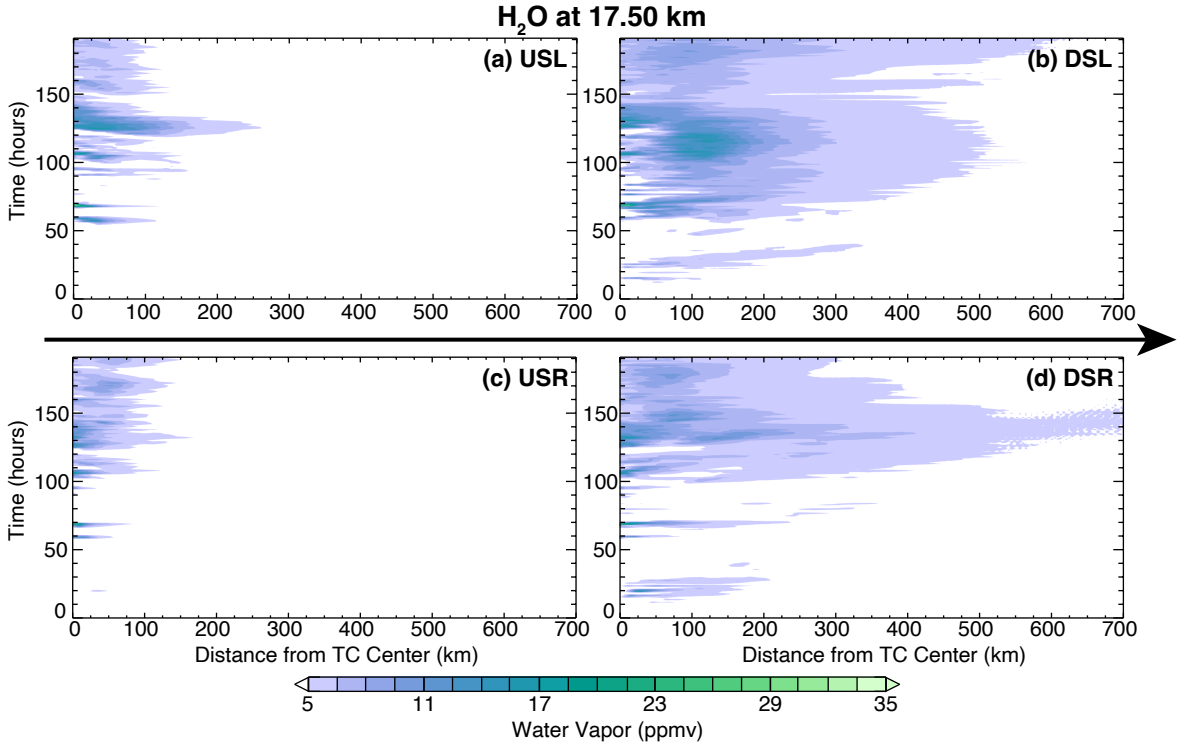


Figure 4.18: For H_2O, space-time diagram at an altitude of 17.50 km for the upshear left (a), downshear left (b), upshear right (c), and downshear right (d) quadrants. The arrow indicates the direction of the VWS vector. Storm averaging occurs in 4-km radial bins over the TC.

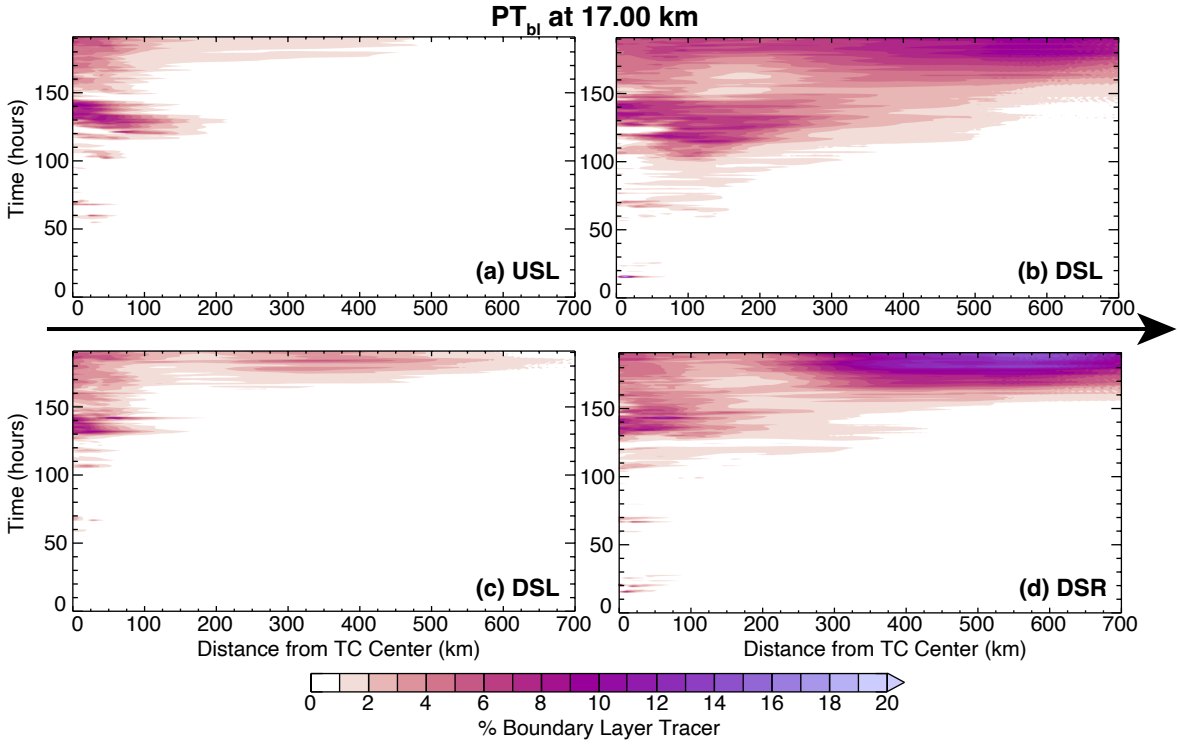


Figure 4.19: As in Figure 4.19, but for the percentage of boundary layer passive tracer (PT_{bl}; boundary layer air) at 17.0 km.

caught in the broader primary circulation of the TC, resulting in maxima of stratospheric air outside of the TC outflow (Fig. 4.20d). This differs slightly from $TC_{noshear}$, where the strengthening of the secondary circulation pushes the transported stratospheric air away from TC center (Fig. 4.20a,b) and transport is symmetric around the TC. The asymmetries introduced by incorporating VWS likely contribute to these differences, as the majority of transported PT_{strat} in TC_{shear} is downshear.

Downward transport in the TC eye for TC_{shear} is visible in all four quadrants and spans a greater area than that in $TC_{noshear}$. The transport of PT_{strat} across the outflow differs by quadrant, as there is greater transport overall in the downshear half of the TC. The upshear quadrants see less of an increase in PT_{strat} until the later in the simulation (hour 160), when the TC_{shear} reaches its maximum intensity and wind speeds begin to decrease (Fig. 4.1). Transport of PT_{strat} increases in the downshear quadrants throughout the simulation, with the downshear left quadrant featuring filaments of high PT_{strat} along the outflow in hours 60-130. These filaments occur when TC_{shear} is intensifying, and is likely associated with the increase of overshoots downshear and subsequent mixing and stirring across the outflow (Fig. 4.3).

4.3 Summary

This chapter used three idealized simulations to examine STE processes and UTLS composition change associated with TCs and their sensitivity to TC intensity and deep-layer environmental wind shear. Within the simulations, H_2O and a suite of passive tracers were evaluated to determine which STE processes were present and influential. For $TC_{noshear}$, overshooting tops were most frequent within the intense eyewall convection of the inner TC rather than the outer rainbands, which agrees with Preston et al. (2019) and differs from Allison et al. (2018), though the choice of model hori-

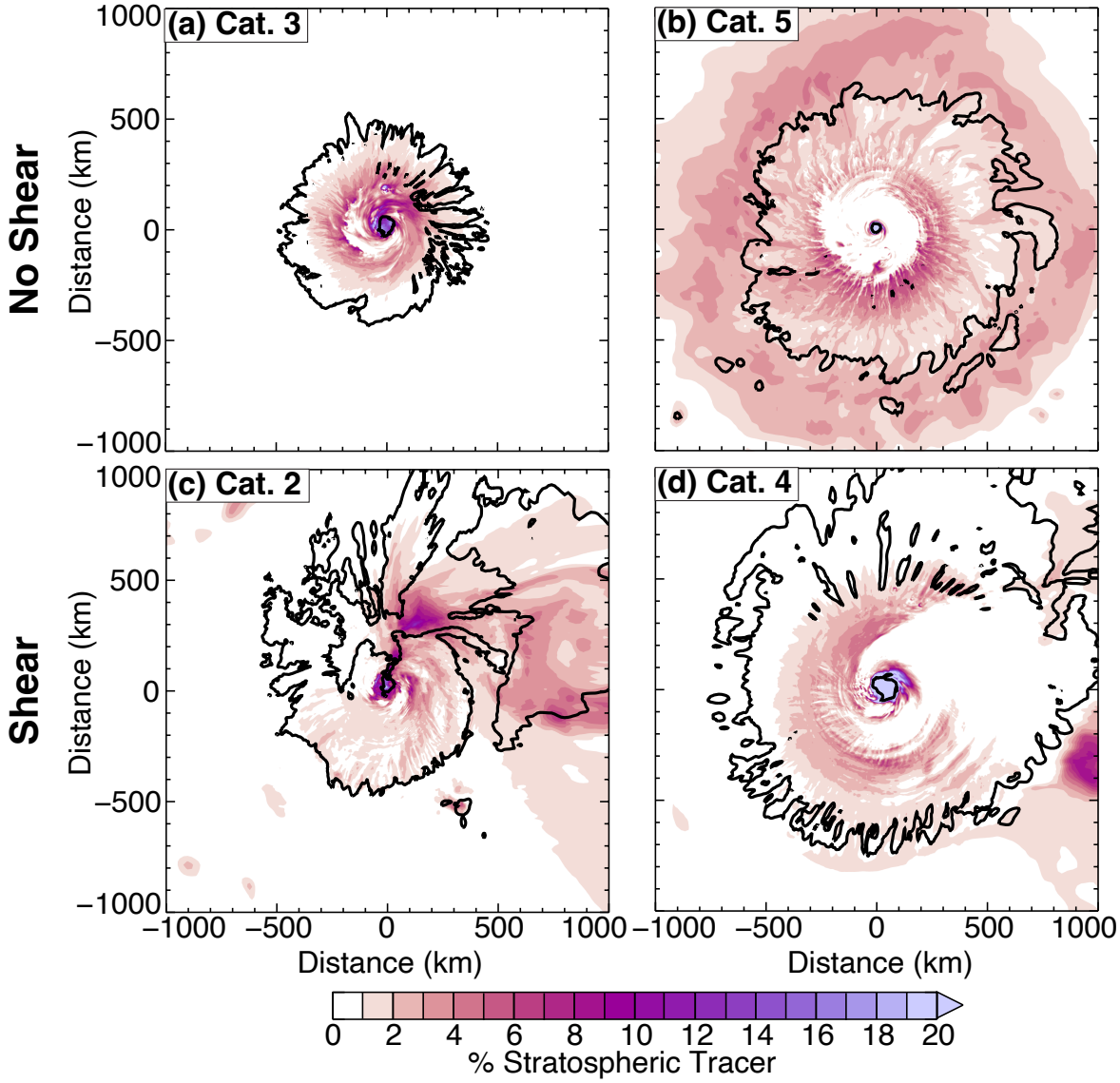


Figure 4.20: Constant-altitude TC-centered plots of stratospheric passive tracer (PT_{strat}) at 15.56 km for $TC_{noshear}$ at category 3 (a) and category 5 (b) intensity and TC_{shear} at category 2 (c) and category 4 (d) intensity. The black contour outlines the cloud boundary (sum of cloud and ice mixing ratios is greater than 1.0×10^{-6} kg kg^{-1}).

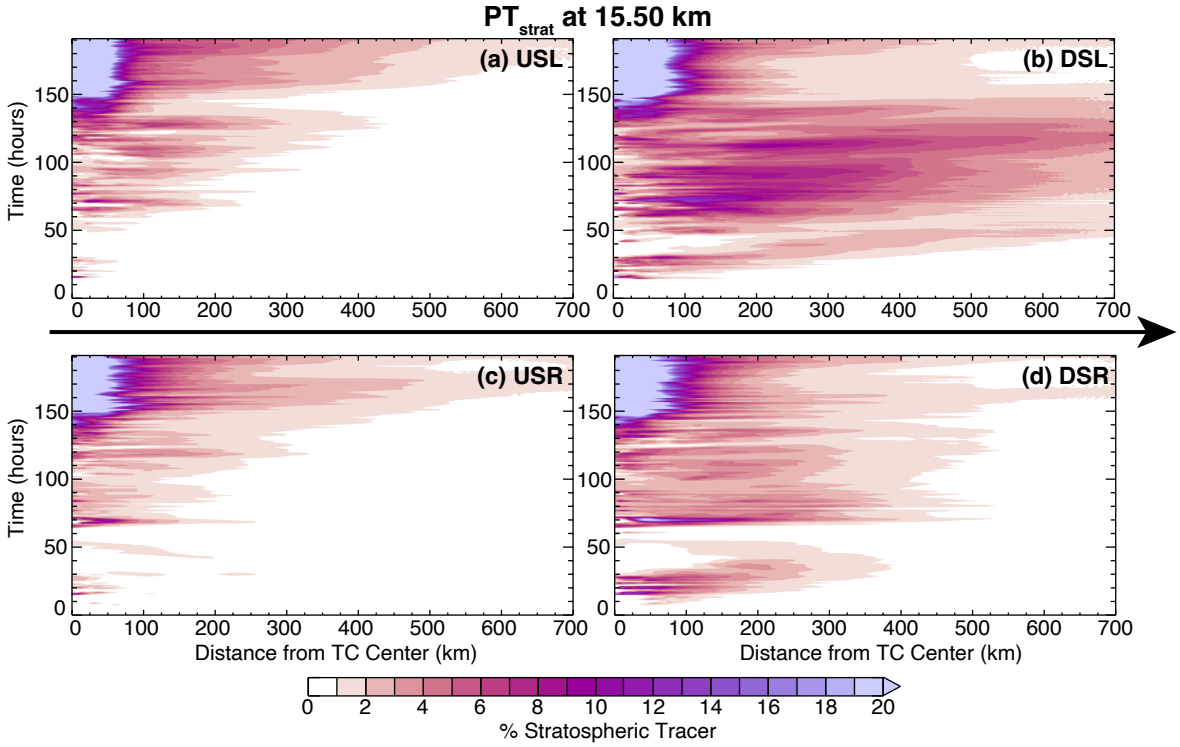


Figure 4.21: As in Figure 4.19, but for the percentage of stratosphere passive tracer (PT_{strat}; stratospheric air) at 15.5 km.

zontal grid spacing could influence overshoot location. Furthermore, overshooting tops were the dominant process associated with H_2O transport to the stratosphere. H_2O reached nearly 20 ppmv at 18.5 km and exhibited enhancements above background at altitudes up to 20 km. The stratospheric H_2O enhancement structure exhibited a "bottleneck" shape with the spatial extent limited to approximately 250 km from TC center and minimized near the tropopause. This shape and spatial confinement is likely due to a saturation-limited environment driven by anomalously low temperatures near tropopause level and at distances outside the inner TC. Cold layers emerge at three central altitudes throughout the simulation, and appear to be related to adiabatic cooling associated with convection. The H_2O bottleneck feature and overall confinement of stratospheric H_2O enhancements to distances within 300 km of TC center are transport outcomes diagnosed for the first time in this chapter. By the time the simulated TC had reached major hurricane intensity, H_2O concentrations in the inner core ($\leq$150 km from TC center) had more than doubled throughout the lower stratosphere and remained as high throughout the remainder of the simulation.

Based on subjective evaluation and comparison of cross-sections like that in Figs. 4.6 and 4.11, TST of boundary layer air (PT_{bl}) appears to be impacted more by isentropic mixing rather than overshooting convection alone. H_2O reaches higher altitudes than boundary layer air, which is consistent with previous modeling work of myriad convective systems (Phoenix and Homeyer, 2021; Gordon and Homeyer, 2022; Preston et al., 2019). Differences in the spatial extent of TST of tropospheric air and H_2O in TCs were identified for the first time in this chapter, with substantial tropospheric air enhancements up to $\sim$1 km above tropopause at distances out to 1000 km from TC center. STT (evidenced by PT_{strat}) primarily occurs via subsidence in the eye, and via overshooting tops and subsequent mixing and advection throughout the tropopause-level outflow. Subsidence in the eye extends deeper into the troposphere and reaches

greater magnitudes but is generally confined to distances <50 km from TC center, while the transport associated with tropopause-level outflow affects a greater area. STT is impacted by changes to TC outflow from intensification, which can lead to features of stratospheric air in the upper troposphere outside the TC outflow that are reminiscent of a stratospheric wrapping signature at later simulation times. The clear evidence of STT in the eye helps resolve some conflicting observational results in the established literature (e.g., Rodgers et al., 1990; Joiner et al., 2006), while the potential nuance in the dynamical explanation of the emergence of a stratospheric wrapping-type feature motivates deeper exploration into STT outside of the eye.

The weaker TC in TC_{lowSST} resulted in the storm outflow remaining ∼2 km below the tropopause in throughout the simulation, rather than impinging upon it as occurred in $\mathrm{TC}_{noshear}$. Thus, although eyewall convection exhibited overshooting tops relative to the broader cloud top, they did not penetrate the tropopause in TC_{lowSST} and consequently there was limited TST of H_2O and PT_{bl}. Although the storm largely remained below the tropopause, frequent STT still occurred and there was a filament of PT_{strat} along the top of the TC outflow. Although not a result of wrapping, this filament exhibits the two-layered stratospheric air signature that was observed and discussed in Baray et al. (1999) and De Bellevue et al. (2006). These difference in UTLS composition change suggest that the height of the TC outflow relative to the tropopause is important for the amount and character of STE in TCs, regardless of TC intensity.

The impacts of deep-layer environmental VWS on TC STE were explored with TC_{shear}. Introducing VWS has been recognized to result in convective asymmetries in the TC in the troposphere, but it was unknown if these asymmetries persisted into the stratosphere and impacted STE. The TC_{shear} simulation revealed that overshoots were most common in the downshear half of the TC, specifically in the downshear left

quadrant, where convection is commonly observed to be strongest. As overshoots are a dominant process for stratospheric hydration, enhanced H_2O was greatest downshear of the TC. H_2O reached greater altitudes and magnitudes in $TC_{noshear}$, but spanned greater distances from TC center in TC_{shear}. This was associated with both higher temperatures near the tropopause and shear-induced differential advection of lower stratosphere air in TC_{shear}. Similar to $TC_{noshear}$, there was no apparent wrapping in TC_{shear}. Rather, PT_{strat} was transported down along the outflow via mixing and stirring by overshooting convection, and subsequently carried by the primary and secondary circulations of the TC. Similar to H_2O and PT_{bl}, the greatest transport of PT_{strat} occurred in the downshear half of TC_{shear}. This demonstrates that convective asymmetries in the troposphere resulting from VWS persist through the top of the TC and impact STE processes and UTLS composition change.

Chapter 5

Discovery of Tropical Cyclone-Driven Stratospheric Temperature Anomalies using Radio Occultation Observations

As demonstrated in Chapter 4, the idealized TC simulations in this dissertation demonstrated that tropopause level cooling is an important constraint for TC impacts on UTLS H_2O. Given that these simulations are unable to incorporate radiation and the impacts vary across the few cases explored, examining TC-induced UTLS temperature change from observations is warranted. However, historically few observations exist in close proximity to a TC throughout its lifecycle over the open ocean to enable detailed evaluation. Satellite-based radio occultation (RO) data offer a modern observational pathway for fine-scale evaluation of TC impacts on UTLS temperature structure.

The Radio Occultation Modeling Experiment (ROMEX; Anthes et al., 2024) conducted during September-November 2022 is a transformative effort to quantify the impact of dense RO observations on weather forecasting, during which all data from the rapidly growing fleet of operational private and public satellites were made publicly available, resulting in nearly 5 times more profiles per day than previous constellations

(∼35,000 daily profiles). Thus, ROMEX provides an unprecedented number of global RO observations of the stratosphere during the NH peak in TC activity and enables fine-scale examination of TC impacts on UTLS temperature. By leveraging ROMEX data in combination with TC tracks from the International Best Track Archive for Climate Stewardship (IBTrACS; Knapp et al., 2010), over 55,000 RO measurements co-located with 31 TCs are analyzed to reveal robust stratosphere temperature perturbations from TCs at altitudes up to 40 km for the first time. Sensitivities to TC intensity, location, and timing are explored and potential dynamic, chemical, and radiative influences are considered and discussed.

5.1 Data and Methods

5.1.1 ROMEX Temperature

In this chapter, RO dry atmospheric temperature retrieval profiles from ROMEX are extracted along Northern Hemisphere TC tracks in the Atlantic, East Pacific, and West Pacific Ocean basins, using the IBTrACs TC positions at 3-hour temporal resolution. ROMEX temperature profiles have a vertical resolution of 100 m. ROMEX profiles that occur within 2000 km and ± 1.5 hours of a given TC track point are retained for analysis. These distance and time thresholds assure that no RO profiles are double counted. TCs must also have a minimum wind speed of 35 kts to trigger ROMEX extraction, as this equates to a Tropical Storm classification on the Saffir-Simpson Hurricane wind speed scale.

To ensure analyzed profiles are consistent with that of the prevailing tropical environment, only profiles with a latitude equatorward of 30°N and a tropopause altitude (using the WMO lapse-rate tropopause definition; World Meteorological Organization,

1957) exceeding 14.5 km are included. To test our calculations, sample non-TC tracks are evaluated which are calculated for comparison following this same methodology, but simply substituting latitudes in the Southern Hemisphere rather than the Northern Hemisphere, where no TCs were present. Additional Southern Hemisphere samples were computed by shifting longitudes in either direction to account for different land and sea combinations, which produced similar results. All ROMEX profiles are aggregated in 100 km bins (total profiles per bin shown in Figure 5.1) of radial distance from TC center out to 1800 km, with temperature anomalies calculated relative to the far-field average temperature from 1900-2000 km. Anomalies calculated for individual TCs are aggregated in 200 km bins from TC center to ensure sufficient sampling per bin. Example tracks and included ROMEX profile locations are shown in Figure 5.2 for Hurricane Fiona (Atlantic basin), Tropical Storm Madeline (East Pacific basin), and Very Strong Typhoon Noru (West Pacific basin). Any profiles in which a temperature at any altitude exceeded three times the standard deviation of the mean at that altitude were considered erroneous and therefore omitted. Overall, approximately 55,000 profiles from 31 TCs are included in the analysis.

5.1.2 ERA5 Reanalysis Temperature and Wind

To provide additional context to ROMEX data analysis, temperature and winds for September – November 2022 are obtained from the version 5 reanalysis produced by the European Centre for Medium-Range Weather Forecasts (ERA5; Hersbach et al., 2020). Temperature profile extractions and the calculation of temperature anomalies follow the same process as those identified for ROMEX data above. ERA5 u and v wind components were additionally extracted and converted to azimuthal (tangential) and radial components relative to TC center. For additional insight into the validity of wind, 1-D gradient wind balance was calculated using ERA5 temperatures and

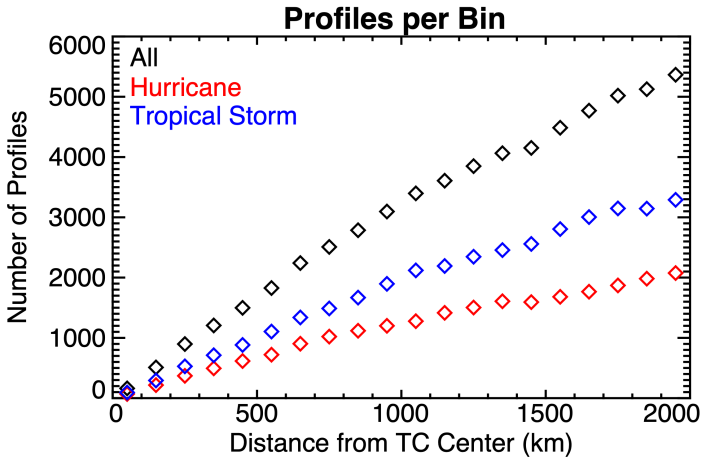


Figure 5.1: Number of ROMEX profiles included in each 100 km bin from TC center for all extracted TC profiles (black), hurricane (red), and tropical storm (blue) profiles.

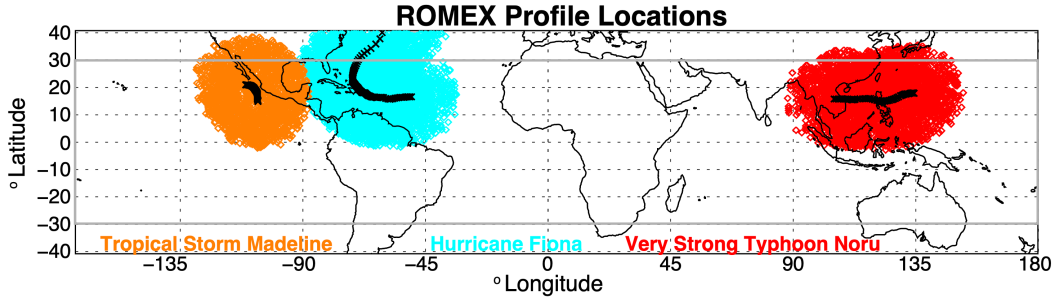


Figure 5.2: Extracted ROMEX profiles for three example storms included in ROMEX data: Tropical Storm Madeline (orange), Hurricane Fiona (cyan) and Very Strong Typhoon Noru (red). TC track points are indicated by black X's. Selected profiles are only equatorward of 30 deg. N, as indicated by the gray box.

following the process described in Rivoire et al. (2016) and Demuth et al. (2004). An alternative approach to calculate anomalies relative to the background climatology was also explored using ERA5, which yields similar results.

5.2 Results

Ubiquitous stratosphere imprints of tropical cyclones

To comprehensively evaluate TC impacts on UTLS temperature structure, temperature anomalies relative to the far-field mean are calculated in 100 km bins from TC center and shown in Figure 5.3a. The mid-to-upper troposphere warm core and near-tropopause cooling explored in prior studies are evident. The warm core anomaly reaches 3 K near TC center and decreases in magnitude as distance from TC center increases, extending outwards of 1400 km from TC center. The near-tropopause cooling extends to ∼1200 km from TC center, and the cooling is greater in magnitude at radii where the warm core anomalies are larger (closer to TC center).

Robust temperature anomalies are also observed at higher stratospheric altitudes in Figure 5.3a. Namely, there is a secondary cold layer in the lower stratosphere (distinct from the tropopause layer) centered at an altitude of 21 km, as large as -1 K near TC center and extends out to ∼1400 km from TC center. Additionally, there is a deep warm layer in the middle stratosphere centered at an altitude of 33 km, as large as 1.75 K near TC center and extends out ∼1600 km from TC center. These stratospheric cold and warm layers have not been previously identified, as previous work has been limited to a vertical extent of 20 km. These stratospheric temperature anomalies are statistically significant based on the numerous ROMEX observations (Fig. S2), exceeding 3x the standard error of the observations for all color-filled areas in Figure 5.3. TCs are a potent source of stratospheric gravity waves (Nolan, 2020; Pahlavan et al., 2023), but such related temperature perturbations are transient features that exhibit "cone-shaped" structure in TC-relative coordinates (as seen in Fig. 11 of Pahlavan et al. (2023)), sloping upward in altitude as distance from TC center increases. This behavior

is very different to the observed quasi-stationary, horizontal 'pancake-like' structures that suggest links to large-scale TC circulations or radiative effects.

Examining anomalies by TC intensity through separating tropical storm and hurricane profiles (Figure 5.3b,c) shows the tropospheric warm-core and near-tropopause cooling are of greater magnitude in hurricanes, in agreement with prior literature (Rivoire et al., 2016). However, the lower stratosphere anomalous cooling and middle stratosphere warming layers aloft are consistently greater in magnitude within tropical storms (Figs. 5.3b,c & 5.4). These differences between tropical storm and hurricane intensity are statistically significant, exceeding 3x the standard error of the observations. These anomalies are present from the onset of tropical storm intensity (Figure 5.3c)), indicating they appear early on and last throughout the TC lifecycle. Additionally, these anomalies are present regardless of ocean basin or latitude (within 0-30°N) and no notable influence from the diurnal cycle is seen. Due to the high density of ROMEX data, there is a sufficient number of profiles to examine individual storms which was not feasible with prior RO capabilities. Focusing on single storms across varying ocean basins and intensities (Figure 5.5) further reveals that the stratospheric temperature anomalies are ubiquitous in TCs. There is some variability in the altitude, magnitude, and radial extent of the layers; however, the general temperature structure is consistent in all cases.

All TC temperature anomalies were alternatively evaluated in tropopause-relative and pressure coordinates and the anomaly structure remains nearly identical, demonstrating vertical coordinate choice does not influence the result. To test the sampling methodology, a similar analysis for ROMEX profiles not co-located with TCs showed no similar layered temperature anomaly structure, providing confidence that these are TC-driven perturbations (Fig. 5.4a). Moreover, these temperature anomalies seem to be unique to TCs as they do not appear in similar studies focusing on deep convection

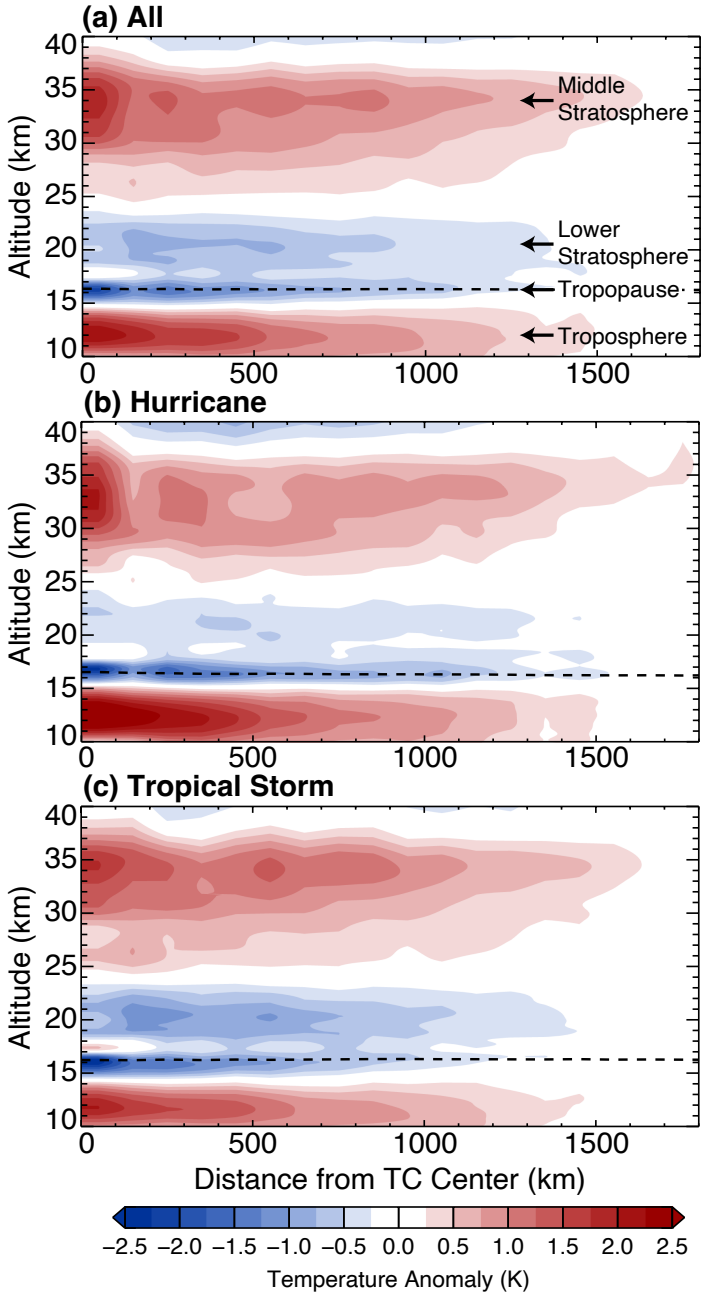


Figure 5.3: ROMEX RO temperature anomalies for (a) all extracted TC profiles, (b) hurricane profiles, and (c) tropical storm profiles. Anomalies are calculated in 100 km bins, relative to far-field temperatures. The black dashed line is the lapse-rate tropopause.

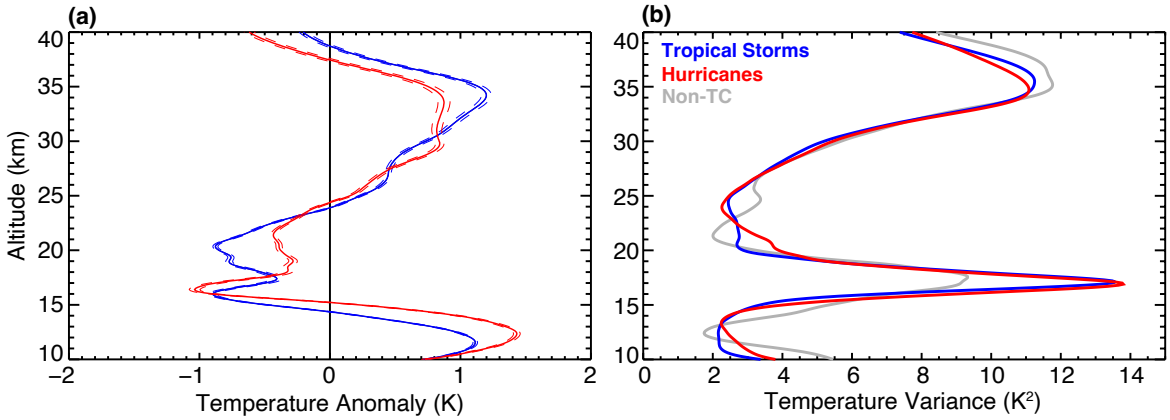


Figure 5.4: Mean temperature anomaly profiles (a) from 0-900 km for non-TC profiles (black), tropical storms (blue) and hurricanes (red). Dashed lines indicate plus or minus the standard error. Temperature variance (b) from 0-900 km for non-TC profiles (black), tropical storms (blue), and hurricanes (red).

(Kim et al., 2018).

Possible Mechanisms Contributing to Stratospheric Features

Given the discovery of ubiquitous TC stratospheric temperature anomalies, this chapter explores possible contributing atmospheric processes. These include dynamical influences of TC circulations extending deep into the stratosphere, effects of gravity waves, and radiative impacts of TC tropospheric temperatures, composition changes and clouds. Each process is considered because they have been demonstrated to impact UTLS temperatures in prior work. For further evaluation of these anomalous structures, ERA5 is used to create comparable TC-centered temperature anomalies for all ROMEX TCs (figure 5.6), as well as case studies of individual TCs (Figure 5.5). ERA5 reanalysis temperature anomalies show good agreement with ROMEX, including capturing the stratospheric cold and warm layers. These similarities are not necessarily surprising, as ERA5 assimilates RO data, although with much less data density than is available from ROMEX. Balanced azimuthal wind calculations computed from 1-D

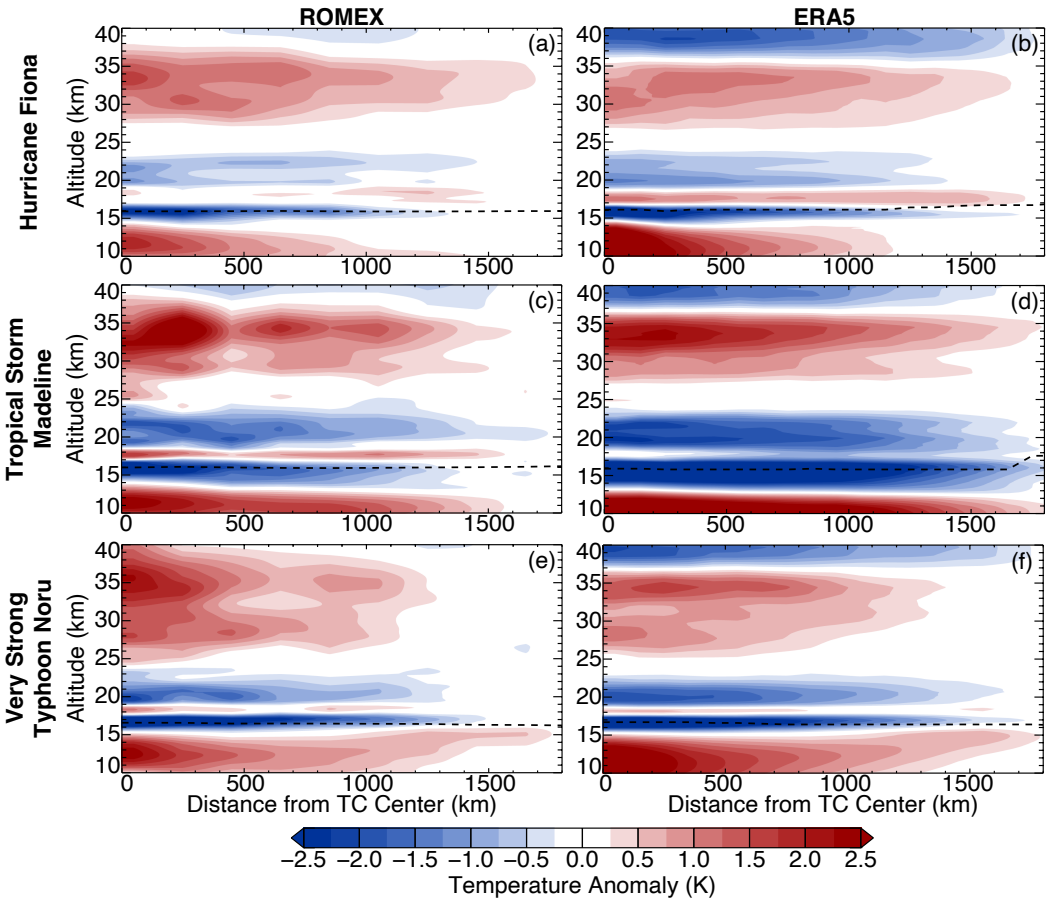


Figure 5.5: **Anomaly structure present for individual storms.** As in Figure 5.3, but for individual storms with ROMEX(left) and ERA5 (right) for Hurricane Fiona (a,b), Tropical Storm Madeline (c,d) and Very Strong Typhoon Noru (e,f).

gradient wind balance (Figure 5.6) show that the lower stratospheric cold layer acts to reduce anticyclonic circulation between the upper troposphere and ∼25 km, reinforcing impacts of the near-tropopause cold layer. The middle stratosphere warm layer is tied to a secondary anticyclonic jet centered near 35 km. This upper-level jet is another TC feature not observed previously.

Mean TC circulations are explored using ERA5 reanalysis radial and azimuth winds and vertical motion in TC-relative coordinates. The analyzed azimuthal winds in the stratosphere are in reasonable agreement with the balanced wind estimates shown in (Figure 5.6). Mean radial winds and vertical motions (i.e., overturning circulations

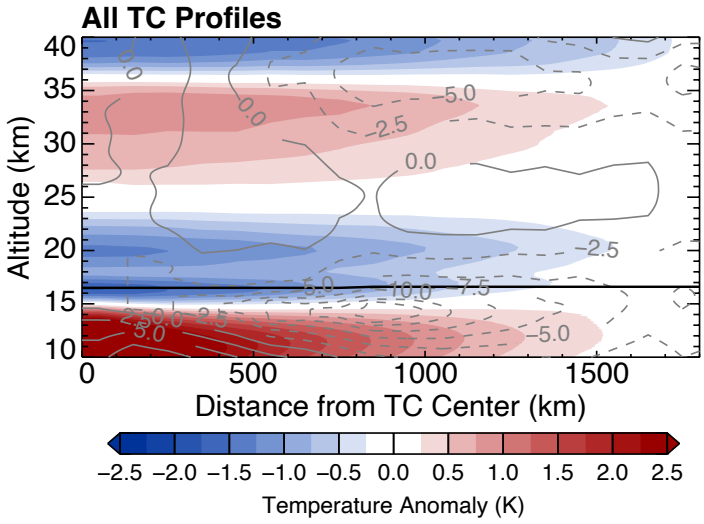


Figure 5.6: ERA5 TC temperature anomalies and gradient wind balance contoured in gray for all extracted TC profiles. Solid gray lines indicating positive gradient wind values and dashed contours indicating negative. The tropopause is indicated by the solid black line.

in the radius-altitude plane) in TCs are weaker and more difficult to evaluate from observations, and results from ERA5 show no systemic structures in the stratosphere linked to the layered temperature anomalies (not shown). This result is not surprising as no related stratospheric wind observations are assimilated in ERA5. Hence, mean circulations derived from ERA5 do not reveal a likely cause for these cold and warm stratospheric layers.

The rectified effects of dissipating or breaking gravity waves are known to force large-scale stratospheric circulations; for example, gravity waves are part of the forcing for the QBO (Pahlavan et al., 2024; Yu et al., 2025). The presence of propagating or breaking gravity waves tied to TCs can be identified in the RO observations by regions of enhanced temperature variance. Results from ROMEX data organized in TC coordinates (Fig. 5.7a,b) show high variance spanning two distinct layers at all distances from TC center, with maxima near and above the tropopause (16-18 km) and atop the middle stratosphere (33-40 km). These maxima atop the middle stratosphere

are characteristic of stratospheric background conditions over low latitudes (Fritts and Alexander, 2003; Pahlavan et al., 2023), where gravity waves are amplified by enhanced stability in the tropopause region, and also amplify with height in the stratosphere due to decreasing atmospheric density. Compared to non-TC samples, the variance in the upper troposphere within the TC core and broadly throughout the lower stratosphere is enhanced relative to non-TC samples. The maxima near and above the tropopause is greater in TCs for both tropical storms and hurricanes than non-TC profiles, likely a result of increased gravity waves associated with convection (Figure 5.4b). Rectified effects of the enhanced tropopause-level gravity waves may be largely responsible for the existence of a two-layered cold anomaly structure, since the enhanced variance broadly coincides with the relatively weak cooling between the near-tropopause and lower stratosphere layers.

The layered stratospheric temperature anomalies are probably not driven by radiative processes linked to TC temperatures, clouds, and composition changes in the troposphere. TC structure includes dense clouds, increased H_2O, and decreased O_3 in the upper troposphere primarily over radii out to $\sim$600 km from TC center (Fagan and Homeyer, 2025; Gordon and Homeyer, 2025; Xu and Takemi, 2022), while the observed stratospheric temperature anomalies extend to far greater distances of $\sim$1500 km. Cloud radiative effects are known to be a minor influence near the tropopause cold layer (Rivoire et al., 2020), and given the lack of a strong diurnal signal observed for the stratospheric temperature anomalies it seems unlikely that cloud radiative influence would be the sole or main contributing factor. Preliminary calculations using a fixed dynamical heating model (Peter Hitchcock, personal communication) furthermore suggest a significant time lag for stratospheric radiative response to imposed tropospheric temperature and composition effects ($\sim$10 days), which is inconsistent with the appearance of the layered stratospheric temperature anomalies at all stages of the TC

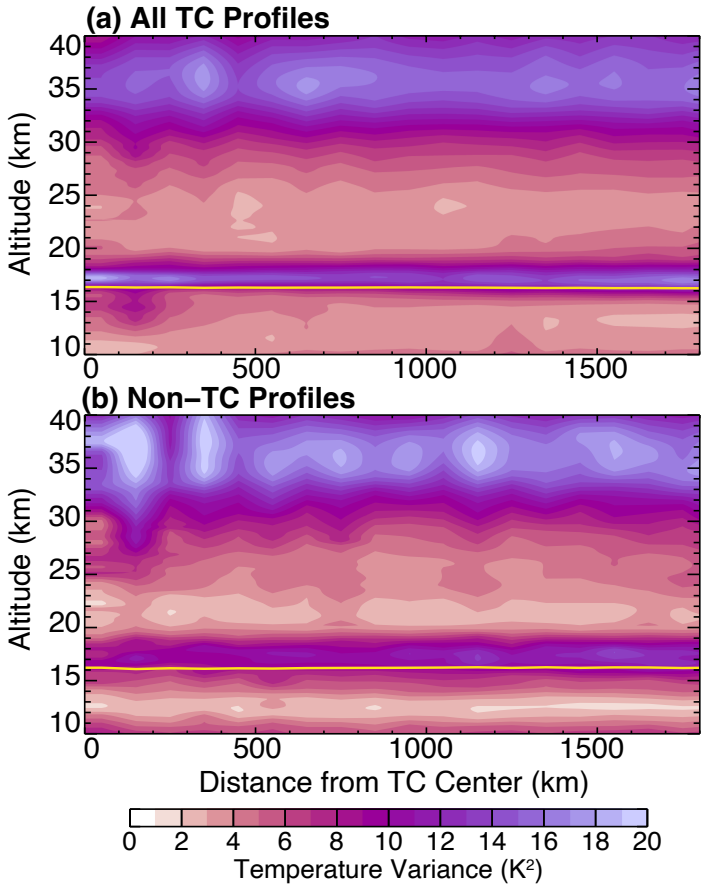


Figure 5.7: ROMEX temperature variance for: (b) all identified TC profiles, (b) non-TC profiles. High temperature variance indicates gravity wave activity. The yellow line is the tropopause.

lifecycle observed in the RO data and the larger anomalies seen in weaker storms.

5.3 Summary

In this chapter, a special collection of radio occultation data, ROMEX, was leveraged during the 2022 Northern Hemisphere tropical cyclone season to reveal that tropical cyclones perturb their environments deeper than previously recognized, driving ubiquitous cold and warm layers in the low-to-middle stratosphere. In addition to the well recognized TC mid-to-upper troposphere warm core and near-tropopause cooling, there is a secondary cold layer in the lower stratosphere (centered near an altitude of 21 km; distinct from the tropopause layer) and a deep warm layer in the middle stratosphere (centered at an altitude of 33 km) that have not been identified in previous work. These stratospheric temperature anomalies have anomalies as large as -1 K and 1.75 K, and extend outwards of ∼1400 km and ∼1600 km, respectively. The stratospheric temperature anomalies are statistically significant and do not change based on vertical coordinate choice. These temperature patterns are present regardless of latitude or basin, show no strong diurnal signal, and are present in individual storms. While the mid-to-upper troposphere warm core and near-tropopause cooling is stronger in hurricanes compared to tropical storms, the stratospheric cooling and warming are stronger in tropical storms. These anomalies are similarly captured in ERA5 reanalysis data.

Dynamical and radiative influences on these stratospheric temperature anomalies are considered. Radiation being the driving process seems less likely due to the much longer timescale required to see similar anomalies. The rectified effects of dissipating gravity waves could contribute towards the anomalies, given the increased variance present above the tropopause for TC profiles. These temperature anomalies are balanced with circulations in the stratosphere. The inferred deep stratospheric circulations

may have impacts on TC evolution and forecasting that are not captured in current simulations.

Chapter 6

Summary and Conclusions

6.1 Lessons Learned

This dissertation has shown that environmental factors, such as varying dynamic and thermodynamic characteristics, influence convectively-driven STE in the midlatitudes and tropics. One example of such for midlatitude convection is the strength of storm-relative winds in the UTLS, as strong winds drive gravity wave breaking and a hydraulic jump that results in the formation of AACPs atop the storm anvil (as also shown in several independent studies). This dissertation has further demonstrated using simulations and observations in Chapters 2 and 3 that these AACP-producing storms have greater TST of H_2O and boundary layer constituents than non AACP-producing storms, and can uniquely transport air from the stratospheric overworld down to the lower stratosphere (and potentially, the upper troposphere). The vertical wind profile is also important for STE facilitated by TCs, as incorporating deep-layer VWS increases the spatial extent of enhanced stratospheric H_2O relative to TC center.

This dissertation has also emphasized that UTLS temperature is an important constraint for transporting H_2O in convective phenomena. In AACP-producing storms, observations in Chapter 3 revealed that low near-tropopause temperatures result in a saturation-limited environment and a different character of STE, where H_2O will preferentially sublimate into the warmer lower stratosphere air and result in a positive

H_2O-O_3 correlation during mixing. Previously, a process resulting in a positive H_2O-O_3 relationship was unknown, as it was widely thought to be a solely negative or neutral relationship. In TCs, simulations in Chapter 4 revealed spatially limited H_2O near the tropopause and in the stratosphere, due to near-tropopause cooling that increased with TC strength. The magnitude of cooling near the tropopause varied depending on TC intensity and shear, the former of which was similarly identified in GNSS-RO observations in Chapter 5, with additional cooling and warming in the stratosphere extending upwards of 40 km that had not been identified in prior literature.

The tropopause altitude and structure itself has been shown to impact STE in overshooting convection. For example, a lower tropopause is easier to reach and allows less diluting effects on air within the updraft (and concomitantly, greater UTLS composition change). Here, it was shown in simulations of midlatitude overshooting convection in Chapter 2 that a double tropopause allows for more expansive AACPs and more TST. For TCs, the altitude of the outflow relative to the tropopause (regardless of TC intensity) was revealed to be important to the resulting STE in Chapter 4. Specifically, a TC that does not impinge upon the tropopause will have less tropopause-overshooting convection and TST, while STT takes on different characteristics. One factor influencing the outflow versus tropopause height in a TC is the base-state SST, revealing that environmental factors near the surface indirectly influence STT in TCs.

This dissertation has shown that there is generally good agreement between the models and observations used for convective STE in the midlatitudes and tropics, especially in the UTLS. For midlatitude AACP-producing storms, airborne observations validated a novel modeling result that AACP-producing storms can transport stratospheric overworld air down to the troposphere through the hydraulic jump and accompanying mixing and stirring.

6.2 Midlatitude Overshooting Convection

While the idealized simulations demonstrated that double tropopause environments enhanced overshooting depth (as in prior observational studies; e.g., Homeyer et al., 2014b; Solomon et al., 2016), such reduction in stratospheric stability was found to have minor impacts on storm dynamics and, ultimately, STE relative to the AACP/non-AACP outcome from the storm-relative wind environment. The increased stratospheric overworld air transport to the lowermost stratosphere in simulated AACP-producing storms suggests such storms could lead to high O_3 and inorganic chlorine being drawn down, which the DCOTSS observations indicated might have been ongoing in the 31 May 2022 flight. As a result, the resulting mixing with enhanced stratospheric H_2O in the lowermost stratosphere can potentially lead to O_3 depletion, so long as the temperature is sufficiently low (Anderson et al., 2012, 2017), which was not the case for the DCOTSS flight, nor for the entire field campaign (Howar et al., 2025). The midlatitude storm simulations in this dissertation also have a lower stratosphere environment that is too warm (characteristic of the midlatitudes) for such chemistry, but similar storms in a higher (tropical) tropopause environment with a colder tropopause would be more conducive. The added sensitivity of increased overworld to lowermost stratosphere transport in double tropopause environments is also less relevant to O_3 depletion since those environments are midlatitude by definition, but the resultant O_3 increase from transport would have radiative implications nonetheless.

Greater STT in simulated non-AACP overshooting storms found here suggests such storms are most important to the upper troposphere O_3 budget, which has an important radiative impact on climate. Moreover, this work draws attention to STT in the vicinity of the overshoot, which accomplishes nearly all of the STT in these simulations. This result is in contrast to significant processes such as anvil wrapping of

stratospheric air found in MCSs that have been the focus of several recent studies (e.g., Pan et al., 2014; Phoenix et al., 2020); no evidence of anvil wrapping was found in the supercell simulations here. Varying lower stratospheric stability (single versus double tropopause) had no discernible impact on STT, which is not surprising since STT impacts are likely more dependent on upper troposphere characteristics.

While Chapter 2 has contributed valuable insights towards the sensitivities of overshooting and cross-tropopause transport to the lower stratospheric environment, there are several sources of variability in tropopause-overshooting convection that can be explored in future work. For example, a much wider range of tropospheric environments are conducive to overshooting convection than the specific midlatitude environment used here. The biggest difference that could be explored is overshooting convection within a tropical, high tropopause environment. Additionally, an environment supporting only discrete supercells was examined here. Supercells are dynamically unique, so exploring other storm modes (such as MCSs) could help to better quantify the range of potential UTLS impacts. While the use of idealized simulations can help to understand some of the fundamental processes, storm characteristics, and sensitivities to storm environments, they are not always indicative or representative of reality.

The results in Chapters 2 & 3 emphasize that determining how often overshooting storms produce AACPs is important for assessing both H_2O and non-H_2O composition impacts to the UTLS. While some insight into stratospheric hydration can be gained from existing overshoot climatologies (Homeyer and Bowman, 2021; Cooney et al., 2018; Solomon et al., 2016; Liu and Liu, 2016; Liu et al., 2020), an AACP climatology is needed to provide sufficient knowledge towards H_2O and non-H_2O UTLS composition change. Machine learning efforts are underway to help facilitate an objective AACP climatology (Cooney et al., 2025).

While Chapter 3 is the first to analyze targeted observations of an AACP, it is

important to note that this was the only DCOTSS flight to do so. Thus, these observations from an AACP-producing storm are representative of only one storm within one environment. Observed UTLS composition changes may vary substantially in other scenarios based on the known sensitivities of STE to the stratospheric environment, as further emphasized by the modeling work in this dissertation. The DCOTSS observations from this flight also have a limited spatial extent, with observations not spanning the entirety of the storm throughout its lifetime. It is also worth noting that it is possible some of the overshoot-influenced air measured could have been sourced from the overshooting storm to the southwest of the target storm. However, the premise of this analysis would not change as the analyzed observations are from active overshooting convection and an AACP regardless of the responsible storm cell. Future modeling work could also simulate this event to supplement the observational analysis conducted here, providing additional perspective on the UTLS composition changes, sources, and constraining mechanisms.

Observations from the 31 May 2022 flight also uniquely showed that H_2O within the overshoot and AACP was saturation-limited due to the constraint of the low temperature, and that stratospheric hydration was occurring via sublimation and subsequent mixing of cool, high-ice cloud material into the warm stratospheric environment. Thus, consideration of saturation-limited H_2O transport in midlatitude overshooting convection is important for future work. Specifically, it is important to determine how frequently a H_2O-limiting temperature constraint occurs and its impact on stratospheric hydration. It is currently unclear whether the temperature constraint is driven by environmental characteristics alone, or if the storms themselves can facilitate it. Exploring the microphysics occurring in overshoots and AACPs could provide increased understanding of these processes. The saturation-limited condition was also associated with a uniquely positive correlation between O_3 and H_2O. Recent efforts evaluating

O_3-H_2O correlations from all DCOTSS flights may provide indirect evidence for the importance of this temperature constraint on a broader scale (Homeyer et al., 2024; Shepherd et al., 2026).

6.3 Tropical Cyclones

While the simulations in Chapter 4 have contributed beneficial insight towards the importance of several STE processes in TCs and their cumulative impacts on UTLS composition, there are multiple sources of variability that could be explored in future work, especially those impacting STT outside of the TC eye. Namely, rather than the previously hypothesized STE process of downward transport of stratospheric air around the edge of tropopause-level TC outflow (i.e., wrapping), similar layered STT features were produced by a variety of mechanisms. In $TC_{noshear}$, the deepening of the TC and strengthening of the secondary circulation over time was responsible for the feature. In TC_{lowSST}, the outflow remained about 2 km below the tropopause, allowing for a filament of stratospheric air to reside above and extend outwards of TC center which results in a vertical profile consistent with what one would expect for wrapping. In TC_{shear}, complex advection of STT near TC center by the primary and secondary circulations resulted in such a feature which was most prominent downshear and right of shear. These results and the broader TST variability revealed by CM1 simulation motivate additional studies with greater variability in environmental characteristics to further resolve the outstanding science questions addressed in this work. Priorities for future work should include determining the persistence of UTLS composition impacts from TCs and the sensitivity of STE in TCs as it encounters a wide variety of environments during its lifecycle (e.g., during extratropical transition).

The near-tropopause dehydration found in the simulated TCs of this dissertation

is also consistent with previous work (Jiang et al., 2020; Allison et al., 2018). Near-tropopause cooling was present in all simulations, but the temperature minimum and corresponding saturation limit was not as low when including VWS or in a weaker/shallower TC. However, it remains unknown if this saturation limit operates similarly across a broader range of UTLS environments, such as those at a higher latitudes. As this simulation does not incorporate radiation, it is also unknown how much radiative processes would modify the cold layers produced in this simulation. Radiation could enhance or lessen the temperature anomalies diagnosed. If radiation were to enhance the cold layers (i.e., reduce cloud-top temperature) then H_2O transport may be more limited, whereas if the cold layers were weakened then H_2O transport may increase.

Similar near-tropopause cooling that increased in magnitude with TC intensity was found in RO observations, and additional significant perturbations to stratospheric temperature structure at higher altitudes were discovered. The discovery of ubiquitous stratospheric TC thermal structures (and corresponding stratospheric circulations) using ROMEX RO observations and outlined in Chapter 5 suggests a much deeper stratospheric impact of TCs than previously appreciated. While the mechanisms responsible for the stratospheric thermal anomalies are not well understood, they are suggestive of mean circulations that could impact TC structural evolution and forecasting, along with influencing background stratospheric dynamics, composition, and transport. Thus, additional work is warranted to identify responsible mechanisms for the existence of these layers and their downstream impacts. Convection-resolving numerical experiments using a high-top model would be ideal to explore responsible mechanisms, as most current simulations typically incorporate a low model top of $\leq$25 km (as employed in the idealized simulations of this dissertation), coarse vertical grid spacing, and a sponge layer to dampen circulations above the lower stratosphere. Similarly, if the observed layers can be independently reproduced by a model, high-

top global simulations could be executed to assess their impact on large scale wave dynamics, the MJO, QBO, and, ultimately, teleconnections.

6.4 Recommended Directions of Future Research

Overall, this dissertation highlights the importance of the stratospheric environment when studying high-impact convective phenomena such as AACP-producing storms and TCs, however, future work is warranted towards increasing understanding and representation of how both convective phenomena interact with the stratosphere.

The unique impact of AACP-producing storms in the midlatitude convection studies of this dissertation has also been recognized in recent follow-on studies (Homeyer et al., 2024; Shepherd et al., 2026). As this dissertation focuses on supercells, additional focus on different storm modes in future simulations would be beneficial. Shepherd et al. (2026) has shown using DCOTSS observations that AACP-producing storms and MCSs are of the most impactful on UTLS composition change. MCSs are the only storm mode thus far recognized to facilitate ozone wrapping (Phoenix et al., 2020). Further exploration of transport mechanisms in MCSs would increase understanding of their prevailing differences from other storm modes. Additionally, exploring overshoots, AACPs, and STE associated with a high-impact subset of MCSs–derechos–could provide valuable insight since derechos have a greater lifetime and spatial extent than other storms and have been documented to contain significant overshooting (Bell et al., 2022). Prior global simulations to explore the contributions of overshooting convection towards stratospheric H_2O only span across the tropics (e.g., Dauhut and Hohenegger, 2022). More expansive global simulations that additionally include the midlatitudes would provide greater insight towards stratospheric H_2O from convection, as it allows for consideration of the impact and persistence of transport from

midlatitude overshooting convection.

For TCs, additional work is warranted in several areas to better understand their interactions with the stratosphere. TCs often migrate to high latitudes and encounter low-tropopause, midlatitude environments (e.g., prior to and during extratropical transition). Tropopause height is a known constraint for STE in overshooting convection (Phoenix and Homeyer, 2021), though its impact on STE in TCs has not yet been explored. Specifically, when encountering midlatitude environments, TCs interact with the tropopause break. The tropopause break is a sharp discontinuity in tropopause altitude near the subtropical jet, typically considered as a boundary between the tropics (tropospheric air) and extratropics (stratospheric air; Homeyer and Bowman, 2013). It is unknown how the dynamics and transport of TCs vary in proximity to the tropopause break, but considerable variations are likely given the sensitivities of TC STE to the environment documented in this dissertation. Nearly 40% percent of TCs undergo extratropical transition, however, STE in TCs undergoing ET has not been explored (Evans et al., 2017). Given that TCs lose their warm-core and undergo several structural and environmental changes, exploring TC STE and dynamics is warranted to increase understanding of TCs and STE overall. Furthermore, it is unknown if the stratospheric temperature anomalies identified in Chapter 5 persist during extratropical transition and how they may vary and thus impact H_2O transport.

TC STE has also not been explored using a global convection-resolving model. Global simulations would allow the exploration of multiple poorly understood aspects of TC STE (e.g., persistence of UTLS impacts, variation throughout lifecycle, extratropical transition) and provide a more wholistic assessment of TC impacts on the UTLS. Lastly, TC intensity is expected to intensify as the climate warms (Walsh et al., 2019), but it is unknown how TC STE may change in future climate scenarios. Regardless of TC intensity, the depth of a TC was found to be critical in this study and

sensitive to the base-state SST. As SSTs are anticipated to be increasing in a warming climate and a major driver of increasing TC intensity, it stands to reason that STE in TCs would increase more dramatically even if the number of TCs did not. Future work could thus explore TCs and UTLS composition change using a pseudo–global warming experiment, as Tinney et al. (2024) utilized for midlatitude tropopause-overshooting convection.

Reference List

Allison, T., H. Fuelberg, and N. Heath, 2018: Simulations of vertical water vapor transport for TC Ingrid (2013). *J. Geophys. Res. Atmos.*, **123**, 8255–8282, https://doi.org/10.1029/2018JD028334.

Anderson, J. G., D. M. Wilmouth, J. B. Smith, and D. S. Sayres, 2012: UV dosage levels in summer: Increased risk of ozone loss from convectively injected water vapor. *Science*, **337 (6096)**, 835–839, https://doi.org/10.1126/science.1222978.

Anderson, J. G., and Coauthors, 2017: Stratospheric ozone over the United States in summer linked to observations of convection and temperature via chlorine and bromine catalysis. *Proc. Nat. Acad. Sci.*, **114**, E4905–E4913, https://doi.org/10.1073/pnas.1619318114.

Anthes, R. A., C. Marquardt, B. Ruston, and H. Shao, 2024: Radio occultation modeling experiment (romex): Determining the impact of radio occultation observations on numerical weather prediction. *Bulletin of the American Meteorological Society*, **105 (8)**, E1552 – E1568, https://doi.org/10.1175/BAMS-D-23-0326.1, URL https://journals.ametsoc.org/view/journals/bams/105/8/BAMS-D-23-0326.1.xml.

Appenzeller, C., and H. C. Davies, 1992: Structure of stratospheric intrusions into the troposphere. *Nature*, **358 (6387)**, 570–572, https://doi.org/10.1038/358570a0, URL https://doi.org/10.1038/358570a0.

Banerjee, A., G. Chiodo, M. Previdi, M. Ponater, A. J. Conley, and L. M. Polvani, 2019: Stratospheric water vapor: an important climate feedback. *Climate Dynamics*, **53**, 1697–1710, https://doi.org/10.1007/s00382-019-04721-4.

Baray, J.-L., G. Ancellet, T. Randriambelo, and S. Baldy, 1999: Tropical cylone marlene and stratosphere-troposphere exchange. *J. Geophys. Res.*, **104 (D11)**, 13,953–13,970.

Bedka, K., E. M. Murillo, C. R. Homeyer, B. Scarino, and H. Mersiovsky, 2018: The above anvil cirrus plume: An important severe weather indicator in visible and infrared satellite imagery. *Wea. Forecasting*, **33**, 1159–1181, https://doi.org/10.1175/WAF-D-18-0040.1.

Bedka, K. M., 2011: Overshooting cloud top detections using MSG SEVIRI infrared brightness temperatures and their relationship to severe weather over Europe. *Atmos. Res.*, **99**, 175–189, https://doi.org/10.1016/j.atmosres.2010.10.001.

Bedka, K. M., C. Wang, R. Rogers, L. D. Carey, W. Feltz, and J. Kanak, 2015: Examining deep convective cloud evolution using total lightning, WSR-88D, and GOES-14 super rapid scan datasets. *Wea. Forecasting*, **30**, 571–590, https://doi.org/10.1175/WAF-D-14-00062.1.

Bell, J. R., and Coauthors, 2022: Satellite-based characterization of convection and impacts from the catastrophic 10 august 2020 midwest u.s. derecho. *Bulletin of the American Meteorological Society*, **103 (4)**, E1172 – E1196, https://doi.org/10.1175/BAMS-D-21-0023.1, URL https://journals.ametsoc.org/view/journals/bams/103/4/BAMS-D-21-0023.1.xml.

Bigelbach, B. C., G. L. Mullendore, and M. Starzec, 2014: Differences in deep convective transport characteristics between quasi-isolated strong convection and mesoscale convective systems using seasonal WRF simulations. *J. Geophys. Res. Atmos.*, **119**, 11,445–11,455, https://doi.org/10.1002/2014JD021875.

Biondi, R., S.-P. Ho, W. Randel, S. Syndergaard, and T. Neubert, 2013: Tropical cyclone cloud-top height and vertical temperature structure detection using gps radio occultation measurements. *Journal of Geophysical Research: Atmospheres*, **118 (11)**, 5247–5259, https://doi.org/https://doi.org/10.1002/jgrd.50448, URL https://agupubs.onlinelibrary.wiley.com/doi/abs/10.1002/jgrd.50448, https://agupubs.onlinelibrary.wiley.com/doi/pdf/10.1002/jgrd.50448.

Biondi, R., A. K. Steiner, G. Kirchengast, and T. Rieckh, 2015: Characterization of thermal structure and conditions for overshooting of tropical and extratropical cyclones with gps radio occultation. *Atmospheric Chemistry and Physics*, **15 (9)**, 5181–5193, https://doi.org/10.5194/acp-15-5181-2015, URL https://acp.copernicus.org/articles/15/5181/2015/.

Brewer, A. W., 1949: Evidence for a world circulation provided by the measurements of helium and water vapour distribution in the stratosphere. *Quarterly Journal of the Royal Meteorological Society*, **75 (326)**, 351–363, https://doi.org/https://doi.org/10.1002/qj.49707532603, URL https://rmets.onlinelibrary.wiley.com/doi/abs/10.1002/qj.49707532603, https://rmets.onlinelibrary.wiley.com/doi/pdf/10.1002/qj.49707532603.

Browell, E. V., E. F. Danielsen, S. Ismail, G. L. Gregory, and S. M. Beck, 1987: Tropopause fold structure determined from airborne lidar and in situ measurements. *Journal of Geophysical Research: Atmospheres*, **92 (D2)**, 2112–2120, https://doi.org/https://doi.org/10.1029/JD092iD02p02112, URL https://agupubs.onlinelibrary.wiley.com/doi/abs/10.1029/JD092iD02p02112, https://agupubs.onlinelibrary.wiley.com/doi/pdf/10.1029/JD092iD02p02112.

Brunner, J. C., S. A. Ackerman, A. S. Bachmeier, and R. M. Rabin, 2007: A quantitative analysis of the enhanced-v feature in relation to severe weather. *Wea. Forecasting*, **22**, 853–872, https://doi.org/10.1175/WAF1022.1.

Bryan, G. H., and J. M. Fritsch, 2000: Diabatically driven discrete propagation of surface fronts: A numerical analysis. *J. Atmos. Sci.*, **57**, 2061–2079.

Bryan, G. H., and J. M. Fritsch, 2002: A benchmark simulation for moist nonhydrostatic numerical models. *Monthly Weather Review*, **130 (12)**, 2917 – 2928, https://doi.org/10.1175/1520-0493(2002)130⟨2917:ABSFMN⟩2.0.CO;2, URL https://journals.ametsoc.org/view/journals/mwre/130/12/1520-0493_2002_130_2917_absfmn_2.0.co_2.xml.

Bryan, G. H., and R. Rotunno, 2009: The maximum intensity of tropical cyclones in axisymmetric numerical model simulations. *Monthly Weather Review*, **137 (6)**, 1770 – 1789, https://doi.org/10.1175/2008MWR2709.1, URL https://journals.ametsoc.org/view/journals/mwre/137/6/2008mwr2709.1.xml.

Chang, K.-W., K. P. Bowman, and A. D. Rapp, 2023: Transport and confinement of plumes from tropopause-overshooting convection over the contiguous united states during the warm season. *Journal of Geophysical Research: Atmospheres*, **128 (2)**, e2022JD037 020, https://doi.org/https://doi.org/10.1029/2022JD037020, URL https://agupubs.onlinelibrary.wiley.com/doi/abs/10.1029/2022JD037020, e2022JD037020 2022JD037020, https://agupubs.onlinelibrary.wiley.com/doi/pdf/10.1029/2022JD037020.

Chelpon, S. M., and Coauthors, 2021: Deriving tropospheric transit time distributions using airborne trace gas measurements: Uncertainty and information content. *Journal of Geophysical Research: Atmospheres*, **126 (17)**, e2020JD034 358, https://doi.org/https://doi.org/10.1029/2020JD034358, URL https://agupubs.onlinelibrary.wiley.com/doi/abs/10.1029/2020JD034358, e2020JD034358 2020JD034358, https://agupubs.onlinelibrary.wiley.com/doi/pdf/10.1029/2020JD034358.

Clapp, C. E., J. B. Smith, K. M. Bedka, and J. G. Anderson, 2023: Distribution of cross-tropopause convection within the asian monsoon region from may through october 2017. *Atmospheric Chemistry and Physics*, **23 (5)**, 3279–3298, https://doi.org/10.5194/acp-23-3279-2023, URL https://acp.copernicus.org/articles/23/3279/2023/.

Cooney, J. W., K. M. Bedka, C. A. Liles, and C. R. Homeyer, 2025: Automated detection of overshooting tops and above-anvil cirrus plumes within geostationary imagery using deep learning. *Artificial Intelligence for the Earth Systems*,

4 (2), e240 037, https://doi.org/10.1175/AIES-D-24-0037.1, URL https://journals.ametsoc.org/view/journals/aies/4/2/AIES-D-24-0037.1.xml.

Cooney, J. W., K. P. Bowman, C. R. Homeyer, and T. M. Fenske, 2018: Ten-year analysis of tropopause-overshooting convection using gridrad data. *J. Geophys. Res. Atmos.*, **123**, 329–343, https://doi.org/10.1002/2017JD027718.

Cooper, O., and Coauthors, 2004: On the life cycle of a stratospheric intrusion and its dispersion into polluted warm conveyor belts. *Journal of Geophysical Research: Atmospheres*, **109 (D23)**, https://doi.org/https://doi.org/10.1029/2003JD004006, URL https://agupubs.onlinelibrary.wiley.com/doi/abs/10.1029/2003JD004006, https://agupubs.onlinelibrary.wiley.com/doi/pdf/10.1029/2003JD004006.

Corbosiero, K. L., and J. Molinari, 2002: The effects of vertical wind shear on the distribution of convection in tropical cyclones. *Monthly Weather Review*, **130 (8)**, 2110 – 2123, https://doi.org/10.1175/1520-0493(2002)130⟨2110:TEOVWS⟩2.0.CO;2, URL https://journals.ametsoc.org/view/journals/mwre/130/8/1520-0493_2002_130_2110_teovws_2.0.co_2.xml.

Crosson, E. R., 2008: A cavity ring-down analyzer for measuring atmospheric levels of methane, carbon dioxide, and water vapor. *Applied Physics B*, **92 (3)**, 403–408, https://doi.org/10.1007/s00340-008-3135-y, URL https://doi.org/10.1007/s00340-008-3135-y.

Danielsen, E. F., 1993: In situ evidence of rapid, vertical, irreversible transport of lower tropospheric air into the lower tropical stratosphere by convective cloud turrets and by larger-scale upwelling in tropical cyclones. *J. Geophys. Res.*, **98 (D5)**, 8665–8681.

Das, S. S., and Coauthors, 2016: Influence of tropical cyclones on tropospheric ozone: possible implications. *Atmos. Chem. Phys.*, **16**, 4837–4847, https://doi.org/10.5194/acp-16-4837-2016.

Dauhut, T., and C. Hohenegger, 2022: The contribution of convection to the stratospheric water vapor: The first budget using a global storm-resolving model. *Journal of Geophysical Research: Atmospheres*, **127 (5)**, e2021JD036 295, https://doi.org/https://doi.org/10.1029/2021JD036295, URL https://agupubs.onlinelibrary.wiley.com/doi/abs/10.1029/2021JD036295, e2021JD036295 2021JD036295, https://agupubs.onlinelibrary.wiley.com/doi/pdf/10.1029/2021JD036295.

De Bellevue, J. L., A. Réchou, J. L. Baray, G. Ancellet, and R. D. Diab, 2006: Signatures of stratosphere to troposphere transport near deep convective events in the southern subtropics. *J. Geophys. Res.*, **111 (D24107)**, https://doi.org/

10.1029/2005JD006947.

Del Genio, A. D., M.-S. Yao, and J. Jonas, 2007: Will moist convection be stronger in a warmer climate? *Geophys. Res. Lett.*, **34**, L16 703, https://doi.org/10.1029/2007GL030525.

Demuth, J. L., M. DeMaria, J. A. Knaff, and T. H. V. Haar, 2004: Evaluation of advanced microwave sounding unit tropical-cyclone intensity and size estimation algorithms. *Journal of Applied Meteorology*, **43 (2)**, 282 – 296, https://doi.org/10.1175/1520-0450(2004)043⟨0282:EOAMSU⟩2.0.CO;2, URL https://journals.ametsoc.org/view/journals/apme/43/2/1520-0450_2004_043_0282_eoamsu_2.0.co_2.xml.

Dessler, A. E., and S. C. Sherwood, 2004: Effect of convection on the summertime extratropical lower stratosphere. *Journal of Geophysical Research: Atmospheres*, **109 (D23)**, https://doi.org/https://doi.org/10.1029/2004JD005209, URL https://agupubs.onlinelibrary.wiley.com/doi/abs/10.1029/2004JD005209, https://agupubs.onlinelibrary.wiley.com/doi/pdf/10.1029/2004JD005209.

Dobson, G. M. B., and H. S. W. Massey, 1956: Origin and distribution of the polyatomic molecules in the atmosphere. *Proceedings of the Royal Society of London. Series A. Mathematical and Physical Sciences*, **236 (1205)**, 187–193, https://doi.org/10.1098/rspa.1956.0127, URL https://royalsocietypublishing.org/doi/abs/10.1098/rspa.1956.0127, https://royalsocietypublishing.org/doi/pdf/10.1098/rspa.1956.0127.

Dunion, J. P., 2011: Rewriting the climatology of the tropical north atlantic and caribbean sea atmosphere. *J. Clim.*, **24**, 893–908, https://doi.org/10.1175/2010JCLI3496.1.

Dworak, R., K. Bedka, J. Brunner, and W. Feltz, 2012: Comparison between /textitGOES-12 overshooting-top detections, WSR-88D radar reflectivity, and severe storm reports. *Wea. Forecasting*, **27**, 684–699, https://doi.org/10.1175/WAF-D-11-00070.1.

Eckhardt, S., A. Stohl, H. Wernli, P. James, C. Forster, and N. Spichtinger, 2004: A 15-year climatology of warm conveyor belts. *Journal of Climate*, **17 (1)**, 218 – 237, https://doi.org/10.1175/1520-0442(2004)017⟨0218:AYCOWC⟩2.0.CO;2, URL https://journals.ametsoc.org/view/journals/clim/17/1/1520-0442_2004_017_0218_aycowc_2.0.co_2.xml.

Evans, C., and Coauthors, 2017: The extratropical transition of tropical cyclones. part i: Cyclone evolution and direct impacts. *Monthly Weather Review*, **145 (11)**, 4317 – 4344, https://doi.org/10.1175/MWR-D-17-0027.1, URL https://journals.ametsoc.org/view/journals/mwre/145/11/mwr-d-17-0027.1.xml.

Fagan, H. E., and C. R. Homeyer, 2025: Upper troposphere lower stratosphere composition change in tropical cyclones: Assessments from 17 years of satellite observations. *Journal of Geophysical Research: Atmospheres*, **130 (22)**, e2025JD044 717, https://doi.org/https://doi.org/10.1029/2025JD044717, URL https://agupubs.onlinelibrary.wiley.com/doi/abs/10.1029/2025JD044717, e2025JD044717 2025JD044717, https://agupubs.onlinelibrary.wiley.com/doi/pdf/10.1029/2025JD044717.

Fischer, H., and Coauthors, 2003: Deep convective injection of boundary layer air into the lowermost stratosphere at midlatitudes. *Atmospheric Chemistry and Physics*, **3 (3)**, 739–745, https://doi.org/10.5194/acp-3-739-2003, URL https://acp.copernicus.org/articles/3/739/2003/.

Flocke, F., and Coauthors, 1999: An examination of chemistry and transport processes in the tropical lower stratosphere using observations of long-lived and short-lived compounds obtained during STRAT and POLARIS. *J. Geophys. Res.*, **104 (D21)**, 26,625–26,642.

Fovell, R., D. Durran, and J. Holton, 1992: Numerical modeling of gravity wave generation by deep tropical convection. *Journal of the Atmospheric Sciences*, **49 (16)**, 1427–1442.

Frank, W. M., and E. A. Ritchie, 2001: Effects of vertical wind shear on the intensity and structure of numerically simulated hurricanes. *Monthly Weather Review*, **129 (9)**, 2249 – 2269, https://doi.org/10.1175/1520-0493(2001)129⟨2249:EOVWSO⟩2.0.CO;2, URL https://journals.ametsoc.org/view/journals/mwre/129/9/1520-0493_2001_129_2249_eovwso_2.0.co_2.xml.

Frey, W., and Coauthors, 2015: The impact of overshooting deep convection on local transport and mixing in the tropical upper troposphere/lower stratosphere (utls). *Atmospheric Chemistry and Physics*, **15 (11)**, 6467–6486, https://doi.org/10.5194/acp-15-6467-2015, URL https://acp.copernicus.org/articles/15/6467/2015/.

Fritts, D. C., and M. J. Alexander, 2003: Gravity wave dynamics and effects in the middle atmosphere. *Reviews of Geophysics*, **41 (1)**, https://doi.org/https://doi.org/10.1029/2001RG000106, URL https://agupubs.onlinelibrary.wiley.com/doi/abs/10.1029/2001RG000106, https://agupubs.onlinelibrary.wiley.com/doi/pdf/10.1029/2001RG000106.

Fromm, M. D., and R. Servranckx, 2003: Transport of forest fire smoke above the tropopause by supercell convection. *Geophys. Res. Lett.*, **30 (10)**, 1542, https://doi.org/10.1029/2002GL016820.

Fujita, T. T., 1974: Overshooting thunderheads observed from ats and learjet. Tech. Rep. NASA-CR-138595, University of Chicago, Department of Geophysical Sciences, Chicago, IL, United States.

Gordon, A. E., and C. R. Homeyer, 2022: Sensitivities of cross-tropopause transport in midlatitude overshooting convection to the lower stratosphere environment. *Journal of Geophysical Research: Atmospheres*, **127 (13)**, e2022JD036 713, https://doi.org/https://doi.org/10.1029/2022JD036713, URL https://agupubs.onlinelibrary.wiley.com/doi/abs/10.1029/2022JD036713, e2022JD036713 2022JD036713, https://agupubs.onlinelibrary.wiley.com/doi/pdf/10.1029/2022JD036713.

Gordon, A. E., and C. R. Homeyer, 2025: Examining stratosphere-troposphere exchange in an idealized simulation of a tropical cyclone. *Journal of Geophysical Research: Atmospheres*, **130 (21)**, e2025JD044 044, https://doi.org/https://doi.org/10.1029/2025JD044044, URL https://agupubs.onlinelibrary.wiley.com/doi/abs/10.1029/2025JD044044, e2025JD044044 2025JD044044, https://agupubs.onlinelibrary.wiley.com/doi/pdf/10.1029/2025JD044044.

Gordon, A. E., and Coauthors, 2024: Airborne observations of upper troposphere and lower stratosphere composition change in active convection producing above-anvil cirrus plumes. *Atmospheric Chemistry and Physics*, **24 (13)**, 7591–7608, https://doi.org/10.5194/acp-24-7591-2024, URL https://acp.copernicus.org/articles/24/7591/2024/.

Hanisco, T. F., and Coauthors, 2007: Observations of deep convective influence on stratospheric water vapor and its isotopic composition. *Geophys. Res. Lett.*, **34**, L04 814, https://doi.org/10.1029/2006GL027899.

Hannun, R. A., A. K. Swanson, S. A. Bailey, T. F. Hanisco, T. P. Bui, I. Bourgeois, J. Peischl, and T. B. Ryerson, 2020: A cavity-enhanced ultraviolet absorption instrument for high-precision, fast-time-response ozone measurements. *Atmospheric Measurement Techniques*, **13 (12)**, 6877–6887, https://doi.org/10.5194/amt-13-6877-2020, URL https://amt.copernicus.org/articles/13/6877/2020/.

Hegglin, M. I., and Coauthors, 2004: Tracing troposphere-to-stratosphere transport above a mid-latitude deep convective system. *Atmos. Chem. Phys.*, **4 (3)**, 741—756, https://doi.org/10.5194/acp-4-741-2004.

Hence, D. A., and R. A. Houze, 2011: Vertical structure of hurricane eyewalls as seen by the trmm precipitation radar. *Journal of the Atmospheric Sciences*, **68 (8)**, 1637 – 1652, https://doi.org/10.1175/2011JAS3578.1, URL https://journals.ametsoc.org/view/journals/atsc/68/8/2011jas3578.1.xml.

Herman, R. L., and Coauthors, 2017: Enhanced stratospheric water vapor over the summertime continental United States and the role of overshooting convection. *Atmos. Chem. Phys.*, **17**, 6113–6124, https://doi.org/10.5194/acp-17-6113-2017.

Hersbach, H., and Coauthors, 2020: The ERA5 global reanalysis. *Q. J. R. Meteorol. Soc.*, **146**, 1999–2049, https://doi.org/10.1002/qj.3803.

Hitchman, M. H., and A. S. Huesmann, 2007: A seasonal climatology of rossby wave breaking in the 320–2000-k layer. *Journal of the Atmospheric Sciences*, **64 (6)**, 1922 – 1940, https://doi.org/10.1175/JAS3927.1, URL https://journals.ametsoc.org/view/journals/atsc/64/6/jas3927.1.xml.

Hoffmann, L., and R. Spang, 2022: An assessment of tropopause characteristics of the ERA5 and ERA-Interim meteorological reanalyses. *Atmos. Chem. Phys.*, **22**, 4019–4046, https://doi.org/10.5194/acp-22-4019-2022.

Holland, G. J., and R. T. Merrill, 1984: On the dynamics of tropical cyclone structural changes. *Quarterly Journal of the Royal Meteorological Society*, **110 (465)**, 723–745, https://doi.org/https://doi.org/10.1002/qj.49711046510, URL https://rmets.onlinelibrary.wiley.com/doi/abs/10.1002/qj.49711046510, https://rmets.onlinelibrary.wiley.com/doi/pdf/10.1002/qj.49711046510.

Holton, J. R., P. H. Haynes, M. E. McIntyre, A. R. Douglass, and L. Pfister, 1995: Stratosphere-troposphere exchange. *Rev. Geophys.*, **33 (4)**, 403–439.

Homeyer, C. R., 2015: Numerical simulations of extratropical tropopause-penetrating convection: Sensitivities to grid resolution. *Journal of Geophysical Research: Atmospheres*, **120 (14)**, 7174–7188, https://doi.org/https://doi.org/10.1002/2015JD023356, URL https://agupubs.onlinelibrary.wiley.com/doi/abs/10.1002/2015JD023356, https://agupubs.onlinelibrary.wiley.com/doi/pdf/10.1002/2015JD023356.

Homeyer, C. R., and K. P. Bowman, 2013: Rossby wave breaking and transport between the tropics and extratropics above the subtropical jet. *Journal of the Atmospheric Sciences*, **70 (2)**, 607 – 626, https://doi.org/10.1175/JAS-D-12-0198.1, URL https://journals.ametsoc.org/view/journals/atsc/70/2/jas-d-12-0198.1.xml.

Homeyer, C. R., and K. P. Bowman, 2021: A 22-year evaluation of convection reaching the stratosphere over the united states. *J. Geophys. Res. Atmos.*, **126**, https://doi.org/10.1029/2021JD034808.

Homeyer, C. R., and K. P. Bowman, 2022: Algorithm description document for version 4.2 of the three-dimensional gridded nexrad wsr-88d radar (gridrad) dataset. Tech.

rep., available online at http://gridrad.org.

Homeyer, C. R., K. P. Bowman, L. L. Pan, E. L. Atlas, R.-S. Gao, and T. L. Campos, 2011: Dynamical and chemical characteristics of tropospheric intrusions observed during START08. *J. Geophys. Res.*, **116**, D06 111, https://doi.org/10.1029/2010JD015098.

Homeyer, C. R., J. D. McAuliffe, and K. M. Bedka, 2017: On the development of above-anvil cirrus plumes in extratropical convection. *J. Atmos. Sci.*, **74**, 1617–1633, https://doi.org/10.1175/JAS-D-16-0269.1.

Homeyer, C. R., L. L. Pan, and M. C. Barth, 2014a: Transport from convective overshooting of the extratropical tropopause and the role of large-scale lower stratosphere stability. *J. Geophys. Res. Atmos.*, **119**, 2220–2240, https://doi.org/10.1002/2013JD020931.

Homeyer, C. R., and Coauthors, 2014b: Convective transport of water vapor into the lower stratosphere observed during double-tropopause events. *J. Geophys. Res. Atmos.*, **119**, 10,941–10,958, https://doi.org/10.1002/2014JD021485.

Homeyer, C. R., and Coauthors, 2023: Extreme altitudes of stratospheric hydration by midlatitude convection observed during the dcotss field campaign. *Geophysical Research Letters*, **50 (18)**, e2023GL104 914, https://doi.org/https://doi.org/10.1029/2023GL104914, URL https://agupubs.onlinelibrary.wiley.com/doi/abs/10.1029/2023GL104914, e2023GL104914 2023GL104914, https://agupubs.onlinelibrary.wiley.com/doi/pdf/10.1029/2023GL104914.

Homeyer, C. R., and Coauthors, 2024: Stratospheric hydration processes in tropopause-overshooting convection revealed by tracer-tracer correlations from the dcotss field campaign. *Journal of Geophysical Research: Atmospheres*, **129 (16)**, e2024JD041 340, https://doi.org/https://doi.org/10.1029/2024JD041340, URL https://agupubs.onlinelibrary.wiley.com/doi/abs/10.1029/2024JD041340, e2024JD041340 2024JD041340, https://agupubs.onlinelibrary.wiley.com/doi/pdf/10.1029/2024JD041340.

Hong, S.-Y., Y. Noh, and J. Dudhia, 2006: A new vertical diffusion package with an explicit treatment of entrainment processes. *Monthly Weather Review*, **134 (9)**, 2318 – 2341, https://doi.org/10.1175/MWR3199.1, URL https://journals.ametsoc.org/view/journals/mwre/134/9/mwr3199.1.xml.

Houze, R. A., 2010: Clouds in tropical cyclones. *Monthly Weather Review*, **138 (2)**, 293 – 344, https://doi.org/10.1175/2009MWR2989.1, URL https://journals.ametsoc.org/view/journals/mwre/138/2/2009mwr2989.1.xml.

Howar, L. V., and Coauthors, 2025: Conditions necessary for chlorine activation in the midlatitude summer lower stratosphere. *Journal of Geophysical Research: Atmospheres*, **130 (20)**, e2025JD043 786, https://doi.org/https://doi.org/10.1029/2025JD043786, URL https://agupubs.onlinelibrary.wiley.com/doi/abs/10.1029/2025JD043786, e2025JD043786 2025JD043786, https://agupubs.onlinelibrary.wiley.com/doi/pdf/10.1029/2025JD043786.

Jiang, B., W. Lin, C. Hu, and Y. Wu, 2020: Tropical cyclones impact on tropopause and the lower stratosphere vapour based on satellite data. *Atmos. Sci. Let.*, **21 (e1006)**, https://doi.org/10.1002/asl.1006.

Jiang, H., and C. Tao, 2014: Contribution of tropical cyclones to global very deep convection. *Journal of Climate*, **27 (11)**, 4313 – 4336, https://doi.org/10.1175/JCLI-D-13-00085.1, URL https://journals.ametsoc.org/view/journals/clim/27/11/jcli-d-13-00085.1.xml.

Joiner, J., A. Vasilkov, K. Yang, and P. K. Bhartia, 2006: Observations over hurricanes from the ozone monitoring instrument. *Geophys. Res. Lett.*, **33 (L06807)**, https://doi.org/10.1029/2005GL025592.

Jones, S. C., 1995: The evolution of vortices in vertical shear. i: Initially barotropic vortices. *Quarterly Journal of the Royal Meteorological Society*, **121 (524)**, 821–851, https://doi.org/https://doi.org/10.1002/qj.49712152406, URL https://rmets.onlinelibrary.wiley.com/doi/abs/10.1002/qj.49712152406, https://rmets.onlinelibrary.wiley.com/doi/pdf/10.1002/qj.49712152406.

Khaykin, S., and Coauthors, 2009: Hydration of the lower stratosphere by ice crystal geysers over land convective systems. *Atmos. Chem. Phys.*, **9**, 2275–2287, https://doi.org/10.5194/acp-9-2275-2009.

Khaykin, S. M., and Coauthors, 2022: Persistence of moist plumes from overshooting convection in the asian monsoon anticyclone. *Atmospheric Chemistry and Physics*, **22 (5)**, 3169–3189, https://doi.org/10.5194/acp-22-3169-2022, URL https://acp.copernicus.org/articles/22/3169/2022/.

Kim, J., W. J. Randel, and T. Birner, 2018: Convectively driven tropopause-level cooling and its influences on stratospheric moisture. *Journal of Geophysical Research: Atmospheres*, **123 (1)**, 590–606, https://doi.org/https://doi.org/10.1002/2017JD027080, URL https://agupubs.onlinelibrary.wiley.com/doi/abs/10.1002/2017JD027080, https://agupubs.onlinelibrary.wiley.com/doi/pdf/10.1002/2017JD027080.

Knapp, K. R., M. C. Kruk, D. H. Levinson, H. J. Diamond, and C. J. Neumann, 2010:

The international best track archive for climate stewardship (ibtracs): Unifying tropical cyclone data. *Bulletin of the American Meteorological Society*, **91 (3)**, 363 – 376, https://doi.org/10.1175/2009BAMS2755.1, URL https://journals.ametsoc.org/view/journals/bams/91/3/2009bams2755_1.xml.

Knutson, T., and Coauthors, 2019: Tropical cyclones and climate change assessment: Part i: Detection and attribution. *Bulletin of the American Meteorological Society*, **100 (10)**, 1987 – 2007, https://doi.org/10.1175/BAMS-D-18-0189.1, URL https://journals.ametsoc.org/view/journals/bams/100/10/bams-d-18-0189.1.xml.

Lacis, A. A., D. J. Wuebbles, and J. A. Logan, 1990: Radiative forcing of climate by changes in the vertical distribution of ozone. *Journal of Geophysical Research: Atmospheres*, **95 (D7)**, 9971–9981, https://doi.org/https://doi.org/10.1029/JD095iD07p09971, URL https://agupubs.onlinelibrary.wiley.com/doi/abs/10.1029/JD095iD07p09971, https://agupubs.onlinelibrary.wiley.com/doi/pdf/10.1029/JD095iD07p09971.

Lane, T. P., M. J. Reeder, and T. L. Clark, 2001: Numerical modeling of gravity wave generation by deep tropical convection. *Journal of the Atmospheric Sciences*, **58 (10)**, 1249 – 1274, https://doi.org/10.1175/1520-0469(2001)058⟨1249:NMOGWG⟩2.0.CO;2, URL https://journals.ametsoc.org/view/journals/atsc/58/10/1520-0469_2001_058_1249_nmogwg_2.0.co_2.xml.

Lenz, A., K. M. Bedka, W. F. Feltz, and S. A. Ackerman, 2009: Convectively induced transverse band signatures in satellite imagery. *Weather and Forecasting*, **24 (5)**, 1362 – 1373, https://doi.org/10.1175/2009WAF2222285.1, URL https://journals.ametsoc.org/view/journals/wefo/24/5/2009waf2222285_1.xml.

Liu, N., and C. Liu, 2016: Global distribution of deep convection reaching tropopause in 1 year GPM observations. *J. Geophys. Res. Atmos.*, **121**, 3824–3842, https://doi.org/10.1002/2015JD024430.

Liu, N., C. Liu, and L. Hayden, 2020: Climatology and detection of overshooting convection from 4 years of GPM precipitation radar and passive microwave observations. *J. Geophys. Res. Atmos.*, **125**, e2019JD032 003, https://doi.org/10.1029/2019JD032003.

Luderer, G., J. Trentmann, K. Hungershöfer, M. Herzog, M. Fromm, and M. O. Andreae, 2007: Small-scale mixing processes enhancing troposphere-to-stratosphere transport by pyro-cumulonimbus storms. *Atmospheric Chemistry and Physics*, **7 (23)**, 5945–5957, https://doi.org/10.5194/acp-7-5945-2007, URL https://acp.copernicus.org/articles/7/5945/2007/.

Marion, G. R., R. J. Trapp, and S. W. Nesbitt, 2019: Using overshooting top area to discriminate potential for large, intense tornadoes. *Geophys. Res. Lett.*, **46**, 12,520–12,526, https://doi.org/10.1029/2019GL084099.

Morrison, H., G. Thompson, and V. Tatarskii, 2009: Impact of cloud microphysics on the development of trailing stratiform precipitation in a simulated squall line: Comparison of one- and two-moment schemes. *Mon. Wea. Rev.*, **137**, 991–1007, https://doi.org/10.1175/2008MWR2556.1.

Mullendore, G. L., D. R. Durran, and J. R. Holton, 2005: Cross-tropopause tracer transport in midlatitude convection. *J. Geophys. Res.*, **110**, D06 113, https://doi.org/10.1029/2004JD005059.

Murillo, E. M., and C. R. Homeyer, 2022: What determines above-anvil cirrus plume infrared temperature? *Journal of the Atmospheric Sciences*, **79 (12)**, 3181 – 3194, https://doi.org/https://doi.org/10.1175/JAS-D-22-0080.1, URL https://journals.ametsoc.org/view/journals/atsc/79/12/JAS-D-22-0080.1.xml.

Newell, R. E., and Coauthors, 1996: Atmosphere sampling of supertyphoon mireille with NASA DC-8 aircraft on september 27, 1991 during PEM-West A. *J. Geophys. Res.*, **101 (D1)**, 1853–1871.

Nguyen, L. T., R. Rogers, J. Zawislak, and J. A. Zhang, 2019: Assessing the influence of convective downdrafts and surface enthalpy fluxes on tropical cyclone intensity change in moderate vertical wind shear. *Monthly Weather Review*, **147 (10)**, 3519 – 3534, https://doi.org/10.1175/MWR-D-18-0461.1, URL https://journals.ametsoc.org/view/journals/mwre/147/10/mwr-d-18-0461.1.xml.

Nolan, D. S., 2020: An investigation of spiral gravity waves radiating from tropical cyclones using a linear, nonhydrostatic model. *Journal of the Atmospheric Sciences*, **77 (5)**, 1733 – 1759, https://doi.org/10.1175/JAS-D-19-0259.1, URL https://journals.ametsoc.org/view/journals/atsc/77/5/jas-d-19-0259.1.xml.

Nugent, A. D., and R. Rios-Berrios, 2018: Factors leading to extreme precipitation on dominica from tropical storm erika (2015). *Monthly Weather Review*, **146 (2)**, 525 – 541, https://doi.org/10.1175/MWR-D-17-0242.1, URL https://journals.ametsoc.org/view/journals/mwre/146/2/mwr-d-17-0242.1.xml.

Nugent, J. M., and C. S. Bretherton, 2023: Tropical convection overshoots the cold point tropopause nearly as often over warm oceans as over land. *Geophysical Research Letters*, **50 (21)**, e2023GL105 083, https://doi.org/https://doi.org/10.1029/2023GL105083, URL https://agupubs.onlinelibrary.wiley.com/doi/abs/10.1029/2023GL105083, e2023GL105083 2023GL105083, https://agupubs.

onlinelibrary.wiley.com/doi/pdf/10.1029/2023GL105083.

O'Neill, M. E., L. Orf, G. M. Heymsfield, and K. Halbert, 2021: Hydraulic jump dynamics above supercell thunderstorms. *Science*, **373**, 1248–1251, https://doi.org/10.1126/science.abh3857.

Pahlavan, H. A., J. M. Wallace, and Q. Fu, 2023: Characteristics of tropical convective gravity waves resolved by era5 reanalysis. *Journal of the Atmospheric Sciences*, **80 (3)**, 777 – 795, https://doi.org/10.1175/JAS-D-22-0057.1, URL https://journals.ametsoc.org/view/journals/atsc/80/3/JAS-D-22-0057.1.xml.

Pahlavan, H. A., J. M. Wallace, Q. Fu, and M. J. Alexander, 2024: Characteristics of gravity waves in opposing phases of the qbo: A reanalysis perspective with era5. *Journal of the Atmospheric Sciences*, **81 (9)**, 1579 – 1587, https://doi.org/10.1175/JAS-D-23-0165.1, URL https://journals.ametsoc.org/view/journals/atsc/81/9/JAS-D-23-0165.1.xml.

Pan, L. L., L. C. Paulik, S. B. Honomichl, L. A. Munchak, J. Bian, H. B. Selkirk, and H. Vömel, 2014: Identification of the tropical tropopause transition layer using the ozone-water vapor relationship. *J. Geophys. Res. Atmos.*, **119**, 3586–3599, https://doi.org/10.1002/2013JD020558.

Phoenix, D. B., and C. R. Homeyer, 2021: Simulated impacts of tropopause-overshooting convection on the chemical composition of the upper troposphere and lower stratosphere. *Journal of Geophysical Research: Atmospheres*, **126 (21)**, e2021JD034 568, https://doi.org/https://doi.org/10.1029/2021JD034568, URL https://agupubs.onlinelibrary.wiley.com/doi/abs/10.1029/2021JD034568, e2021JD034568 2021JD034568, https://agupubs.onlinelibrary.wiley.com/doi/pdf/10.1029/2021JD034568.

Phoenix, D. B., C. R. Homeyer, M. C. Barth, and S. B. Trier, 2020: Mechanisms responsible for stratosphere-to-troposphere transport around a mesoscale convective system anvil. *J. Geophys. Res. Atmos.*, **125**, https://doi.org/10.1029/2019JD032016.

Postel, G. A., and M. H. Hitchman, 1999: A climatology of rossby wave breaking along the subtropical tropopause. *Journal of the Atmospheric Sciences*, **56 (3)**, 359 – 373, https://doi.org/10.1175/1520-0469(1999)056⟨0359:ACORWB⟩2.0.CO;2, URL https://journals.ametsoc.org/view/journals/atsc/56/3/1520-0469_1999_056_0359_acorwb_2.0.co_2.xml.

Poulida, O., R. R. Dickerson, and A. Heymsfield, 1996: Stratosphere-troposphere exchange in a midlatitude mesoscale convective complex 1. observations. *J. Geophys. Res.*, **101 (D3)**, 6823–6836.

Preston, A. D., H. E. Fuelberg, and M. C. Barth, 2019: Simulation of chemical transport by typhoon mireille (1991). *J. Geophys. Res. Atmos.*, **124**, 11,614–11,639, https://doi.org/10.1029/2019JD030446.

Randel, W. J., E. Moyer, M. Park, E. Jensen, P. Bernath, K. Walker, and C. Boone, 2012: Global variations of HDO and HDO/H_2O ratios in the upper troposphere and lower stratosphere derived from ACE-FTS satellite measurements. *J. Geophys. Res.*, **117**, D06 303, https://doi.org/10.1029/2011JD016632.

Ratnam, M. V., S. R. Babu, S. S. Das, G. Basha, B. V. Krishnamurthy, and B. Venkateswararao, 2016: Effect of tropical cyclones on the stratosphere–troposphere exchange observed using satellite observations over the north indian ocean. *Atmos. Chem. Phys.*, **16**, 8581–8591, https://doi.org/10.5194/acp-16-8581-2016.

Ray, E. A., and K. H. Rosenlof, 2007: Hydration of the upper troposphere by tropical cyclones. *J. Geophys. Res.*, **112 (D12311)**, https://doi.org/10.1029/2006JD008009.

Reasor, P. D., R. Rogers, and S. Lorsolo, 2013: Environmental flow impacts on tropical cyclone structure diagnosed from airborne doppler radar composites. *Monthly Weather Review*, **141 (9)**, 2949 – 2969, https://doi.org/10.1175/MWR-D-12-00334.1, URL https://journals.ametsoc.org/view/journals/mwre/141/9/mwr-d-12-00334.1.xml.

Rios-Berrios, R., C. A. Davis, and R. D. Torn, 2018: A hypothesis for the intensification of tropical cyclones under moderate vertical wind shear. *Journal of the Atmospheric Sciences*, **75 (12)**, 4149 – 4173, https://doi.org/10.1175/JAS-D-18-0070.1, URL https://journals.ametsoc.org/view/journals/atsc/75/12/jas-d-18-0070.1.xml.

Rios-Berrios, R., P. M. Finocchio, J. J. Alland, X. Chen, M. S. Fischer, S. N. Stevenson, and D. Tao, 2024: A review of the interactions between tropical cyclones and environmental vertical wind shear. *Journal of the Atmospheric Sciences*, **81 (4)**, 713 – 741, https://doi.org/10.1175/JAS-D-23-0022.1, URL https://journals.ametsoc.org/view/journals/atsc/81/4/JAS-D-23-0022.1.xml.

Rios-Berrios, R., and R. D. Torn, 2017: Climatological analysis of tropical cyclone intensity changes under moderate vertical wind shear. *Monthly Weather Review*, **145 (5)**, 1717 – 1738, https://doi.org/10.1175/MWR-D-16-0350.1, URL https://journals.ametsoc.org/view/journals/mwre/145/5/mwr-d-16-0350.1.xml.

Rivoire, L., T. Birner, and J. A. Knaff, 2016: Evolution of the upper-level thermal structure in tropical cyclones. *Geophysical Research Letters*, **43 (19)**, 10,530–10,537, https://doi.org/https://doi.org/10.1002/2016GL070622, URL https://

agupubs.onlinelibrary.wiley.com/doi/abs/10.1002/2016GL070622, https://agupubs.onlinelibrary.wiley.com/doi/pdf/10.1002/2016GL070622.

Rivoire, L., T. Birner, J. A. Knaff, and N. Tourville, 2020: Quantifying the radiative impact of clouds on tropopause layer cooling in tropical cyclones. *Journal of Climate*, **33 (15)**, 6361 – 6376, https://doi.org/10.1175/JCLI-D-19-0813.1, URL https://journals.ametsoc.org/view/journals/clim/33/15/JCLI-D-19-0813.1.xml.

Rodgers, E. B., J. Stout, J. Steranka, and S. Chang, 1990: Tropical cyclone-upper atmospheric interaction as inferred from satellite total ozone observations. *J. Appl. Meteor.*, **29**, 934–954.

Romps, D. M., and Z. Kuang, 2009: Overshooting convection in tropical cyclones. *Geophysical Research Letters*, **36 (9)**, https://doi.org/https://doi.org/10.1029/2009GL037396, URL https://agupubs.onlinelibrary.wiley.com/doi/abs/10.1029/2009GL037396, https://agupubs.onlinelibrary.wiley.com/doi/pdf/10.1029/2009GL037396.

Roux, F., H. Clark, K.-Y. Wang, S. Rohs, B. Sauvage, and P. Nédélec, 2020: The influence of typhoons on atmospheric composition deduced from IAGOS measurements over taipei. *Atmos. Chem. Phys.*, **20**, 3945–3963, https://doi.org/10.5194/acp-20-3945-2020.

Salby, M. L., and P. F. Callaghan, 2006: Influence of the brewer-dobson circulation on stratosphere-troposphere exchange. *Journal of Geophysical Research: Atmospheres*, **111 (D21)**, https://doi.org/https://doi.org/10.1029/2006JD007051, URL https://agupubs.onlinelibrary.wiley.com/doi/abs/10.1029/2006JD007051, https://agupubs.onlinelibrary.wiley.com/doi/pdf/10.1029/2006JD007051.

Sandmæl, T. N., C. R. Homeyer, K. M. Bedka, J. M. Apke, J. R. Mecikalski, and K. Khlopenkov, 2019: Evaluating the ability of remote sensing observations to identify significantly severe and potentially tornadic storms. *J. Appl. Meteor. Climatol.*, **58**, 2569–2590, https://doi.org/10.1175/JAMC-D-18-0241.1.

Sargent, M. R., and Coauthors, 2013: A new direct absorption tunable diode lase spectrometere for high precision measurement of water vapor in the upper troposphere and lower stratosphere. *Rev. Sci. Instrum.*, **84**, 074 102, https://doi.org/10.1063/1.4815828.

Sayres, D. S., and Coauthors, 2009: A new cavity based absorption instrument for detection of water isotopologues in the upper troposphere and lower stratosphere. *Review of Scientific Instruments*, **80 (4)**, 044 102, https://doi.org/10.1063/1.3117349, URL https://doi.org/10.1063/1.3117349, https://pubs.aip.org/aip/rsi/article-pdf/

doi/10.1063/1.3117349/15941326/044102_1_online.pdf.

Schauffler, S. M., E. L. Atlas, D. R. Blake, F. Flocke, R. A. Lueb, J. M. Lee-Taylor, V. Stroud, and W. Travnicek, 1999: Distributions of brominated organic compounds in the troposphere and lower stratosphere. *Journal of Geophysical Research: Atmospheres*, **104 (D17)**, 21 513–21 535, https://doi.org/https://doi.org/10.1029/1999JD900197, URL https://agupubs.onlinelibrary.wiley.com/doi/abs/10.1029/1999JD900197, https://agupubs.onlinelibrary.wiley.com/doi/pdf/10.1029/1999JD900197.

Schmit, T. J., P. Griffith, M. M. Gunshor, J. M. Daniels, S. J. Goodman, and W. J. Lebair, 2017: A closer look at the abi on the goes-r series. *Bulletin of the American Meteorological Society*, **98 (4)**, 681 – 698, https://doi.org/https://doi.org/10.1175/BAMS-D-15-00230.1, URL https://journals.ametsoc.org/view/journals/bams/98/4/bams-d-15-00230.1.xml.

Schwartz, M. J., W. G. Read, M. L. Santee, N. J. Livesey, L. Froidevaux, A. Lambert, and G. L. Manney, 2013: Convectively injected water vapor in the North American summer lowermost stratosphere. *Geophys. Res. Lett.*, **40**, 1–6, https://doi.org/10.1002/grl.50421.

Scott, S. G., T. P. Bui, and K. R. Chan, 1990: The meteorological measurement system on the NASA ER-2 aircraft. *J. Atmos. Oceanic Technol.*, **7**, 525–540, https://doi.org/10.1175/1520-0426(1990)007⟨0525:TMMSOT⟩2.0.CO;2.

Shepherd, C. M., and Coauthors, 2026: Evaluating the impacts of storm-scale and environmental factors on stratosphere-troposphere exchange associated with midlatitude convection. *Journal of Geophysical Research: Atmospheres*, **131 (5)**, e2025JD045 514, https://doi.org/https://doi.org/10.1029/2025JD045514, URL https://agupubs.onlinelibrary.wiley.com/doi/abs/10.1029/2025JD045514, e2025JD045514 2025JD045514, https://agupubs.onlinelibrary.wiley.com/doi/pdf/10.1029/2025JD045514.

Smith, J. B., and Coauthors, 2017: A case study of convectively sourced water vapor observed in the overworld stratosphere over the united states. *J. Geophys. Res. Atmos.*, **122**, 9529–9554, https://doi.org/10.1002/2017JD026831.

Solomon, D. L., K. P. Bowman, and C. R. Homeyer, 2016: Tropopause-penetrating convection from three-dimensional gridded NEXRAD data. *J. Appl. Meteor. Climatol.*, **55**, 465–478, https://doi.org/10.1175/JAMC-D-15-0190.1.

Solomon, S., K. H. Rosenlof, R. W. Portmann, J. S. Daniel, S. M. Davis, T. J. Sanford, and G.-K. Plattner, 2010: Contributions of stratospheric water vapor to decadal

changes in the rate of global warming. *Science*, **327**, 1219–1223, https://doi.org/10.1126/science.1182488.

Starzec, M., G. L. Mullendore, and C. R. Homeyer, 2020: Retrievals of convective detrainment heights using ground-based radar observations. *J. Geophys. Res. Atmos.*, **125**, https://doi.org/10.1029/2019JD031164.

Stevens, B., W. R. Cotton, G. Feingold, and C.-H. Moeng, 1998: Large-eddy simulations of strongly precipitating, shallow, stratocumulus-topped boundary layers. *Journal of the Atmospheric Sciences*, **55 (24)**, 3616 – 3638, https://doi.org/10.1175/1520-0469(1998)055⟨3616:LESOSP⟩2.0.CO;2, URL https://journals.ametsoc.org/view/journals/atsc/55/24/1520-0469_1998_055_3616_lesosp_2.0.co_2.xml.

Stohl, A., H. Wernli, P. James, M. Bourqui, C. Forster, M. A. Liniger, P. Seibert, and M. Sprenger, 2003: A new perspective of stratosphere-troposphere exchange. *Bull. Amer. Meteorol. Soc.*, **84 (11)**, 1565–1573.

Tilmes, S., and Coauthors, 2010: An aircraft-based upper troposphere lower stratosphere o3, co, and h2o climatology for the northern hemisphere. *Journal of Geophysical Research: Atmospheres*, **115 (D14)**, https://doi.org/https://doi.org/10.1029/2009JD012731, URL https://agupubs.onlinelibrary.wiley.com/doi/abs/10.1029/2009JD012731, https://agupubs.onlinelibrary.wiley.com/doi/pdf/10.1029/2009JD012731.

Tinney, E. N., and C. R. Homeyer, 2021: A 13-year trajectory-based analysis of convection-driven changes in upper troposphere lower stratosphere composition over the united states. *J. Geophys. Res. Atmos.*, **126**, e2020JD033 657, https://doi.org/10.1029/2020JD033657.

Tinney, E. N., C. R. Homeyer, K. M. Bedka, and B. R. Scarino, 2024: The response of tropopause-overshooting convection over north america to climate change. *Journal of Climate*, **37 (23)**, 6183 – 6200, https://doi.org/10.1175/JCLI-D-23-0745.1, URL https://journals.ametsoc.org/view/journals/clim/37/23/JCLI-D-23-0745.1.xml.

Tinney, E. N., C. R. Homeyer, L. Elizalde, D. F. Hurst, A. M. Thompson, R. M. Stauffer, H. Vömel, and H. B. Selkirk, 2022: A modern approach to a stability-based definition of the tropopause. *Monthly Weather Review*, **150 (12)**, 3151 – 3174, https://doi.org/10.1175/MWR-D-22-0174.1, URL https://journals.ametsoc.org/view/journals/mwre/150/12/MWR-D-22-0174.1.xml.

Trapp, R. J., N. S. Diffenbaugh, H. E. Brooks, M. E. Baldwin, E. D. Robinson, and J. S. Pal, 2007: Changes in severe thunderstorm environment frequency during the 21st century caused by anthropogenically enhanced global radiative forcing. *Proc.*

Nat. Acad. Sci., **104**, 19,719–19,723, https://doi.org/10.1073/pnas.0705494104.

Ueyama, R., M. Schoeberl, E. Jensen, L. Pfister, M. Park, and J.-M. Ryoo, 2023: Convective impact on the global lower stratospheric water vapor budget. *Journal of Geophysical Research: Atmospheres*, **128 (6)**, e2022JD037 135, https://doi.org/https://doi.org/10.1029/2022JD037135, URL https://agupubs.onlinelibrary.wiley.com/doi/abs/10.1029/2022JD037135, e2022JD037135 2022JD037135, https://agupubs.onlinelibrary.wiley.com/doi/pdf/10.1029/2022JD037135.

Walsh, K., S. Camargo, T. Knutson, J. Kossin, T.-C. Lee, H. Murakami, and C. Patricola, 2019: Tropical cyclones and climate change. *Tropical Cyclone Research and Review*, **8 (4)**, 240–250, https://doi.org/https://doi.org/10.1016/j.tcrr.2020.01.004, URL https://www.sciencedirect.com/science/article/pii/S2225603220300047.

Wang, P. K., 2003: Moisture plumes above thunderstorm anvils and their contributions to cross-tropopause transport of water vapor in midlatitudes. *J. Geophys. Res.*, **108 (D6)**, 4194, https://doi.org/10.1029/2002JD002581.

Wang, P. K., K.-Y. Cheng, M. Setvák, and C.-K. Wang, 2016: The origin of the gullwing-shaped cirrus above an Argentinian thunderstorm as seen in CALIPSO images. *J. Geophys. Res. Atmos.*, **121**, 3729–3738, https://doi.org/10.1002/2015JD024111.

Weisman, M., and J. Klemp, 1982: The dependence of numerically simulated convective storms on vertical wind shear and buoyancy. *Monthly Weather Review - MON WEATHER REV*, **110**, https://doi.org/10.1175/1520-0493(1982)110⟨0504:TDONSC⟩2.0.CO;2.

Werner, F., M. J. Schwartz, N. J. Livesey, W. G. Read, and M. L. Santee, 2020: Extreme outliers in lower stratospheric water vapor over north america observed by mls: Relation to overshooting convection diagnosed from colocated aqua-modis data. *Geophysical Research Letters*, **47 (24)**, e2020GL090 131, https://doi.org/https://doi.org/10.1029/2020GL090131, URL https://agupubs.onlinelibrary.wiley.com/doi/abs/10.1029/2020GL090131, e2020GL090131 10.1029/2020GL090131, https://agupubs.onlinelibrary.wiley.com/doi/pdf/10.1029/2020GL090131.

Wernli, H., and M. Bourqui, 2002: A lagrangian "1-year climatology" of (deep) cross-tropopause exchange in the extratropical northern hemisphere. *Journal of Geophysical Research: Atmospheres*, **107 (D2)**, ACL 13–1–ACL 13–16, https://doi.org/https://doi.org/10.1029/2001JD000812, URL https://agupubs.onlinelibrary.wiley.com/doi/abs/10.1029/2001JD000812, https://agupubs.onlinelibrary.wiley.com/doi/pdf/10.1029/2001JD000812.

World Meteorological Organization, 1957: Meteorology—a three-dimensional science: Second session of the commission for aerology. *World Meteorol. Organ. Bull.*, **4**, 134–138.

Xu, M., and T. Takemi, 2022: Radiative effects on tropical cyclone development in different life stages. *Monthly Weather Review*, **150 (12)**, 3131 – 3150, https://doi.org/10.1175/MWR-D-21-0337.1, URL https://journals.ametsoc.org/view/journals/mwre/150/12/MWR-D-21-0337.1.xml.

Yu, W., W. M. Hannah, J. J. Benedict, C.-C. Chen, and J. H. Richter, 2025: Improving the qbo forcing by resolved waves with vertical grid refinement in e3smv2. *Journal of Advances in Modeling Earth Systems*, **17 (5)**, e2024MS004 473, https://doi.org/ https://doi.org/10.1029/2024MS004473, URL https://agupubs.onlinelibrary.wiley.com/doi/abs/10.1029/2024MS004473, e2024MS004473 2024MS004473, https://agupubs.onlinelibrary.wiley.com/doi/pdf/10.1029/2024MS004473.

Zou, X., and Y. Wu, 2005: On the relationship between total ozone mapping spectrometer (toms) ozone and hurricanes. *J. Geophys. Res.*, **110 (D06109)**, https://doi.org/10.1029/2004JD005019.